9-1-2018

Thermochemical Non-Equilibrium Models for Weakly Ionized Hypersonic Flows with Application to Slender-Body Wakes

Matthew P. Clarey

THERMOCHEMICAL NON-EQUILIBRIUM MODELS FOR WEAKLY IONIZED HYPERSONIC FLOWS WITH APPLICATION TO SLENDER-BODY WAKES

DISSERTATION

Matthew P. Clarey, Capt, USAF

AFIT-ENY-DS-18-S-059

DEPARTMENT OF THE AIR FORCE
AIR UNIVERSITY

AIR FORCE INSTITUTE OF TECHNOLOGY

Wright-Patterson Air Force Base, Ohio

AFIT-ENY-DS-18-S-059

THERMOCHEMICAL NON-EQUILIBRIUM MODELS FOR WEAKLY IONIZED HYPERSONIC FLOWS WITH APPLICATION TO SLENDER-BODY WAKES

DISSERTATION

Presented to the Faculty

Graduate School of Engineering and Management

Air Force Institute of Technology

Air University

Air Education and Training Command

in Partial Fulfillment of the Requirements for the

Degree of Doctor of Philosophy

Matthew P. Clarey, B.S., M.S.

Capt, USAF

September 2018

AFIT-ENY-DS-18-S-059

THERMOCHEMICAL NON-EQUILIBRIUM MODELS FOR WEAKLY IONIZED HYPERSONIC FLOWS WITH APPLICATION TO SLENDER-BODY WAKES

Matthew P. Clarey, B.S., M.S.
Capt, USAF

Committee Membership:

Robert B. Greendyke, Ph.D.
Chairman

Maj Darrell Crowe, Ph.D
Member

Maj Brook I. Bentley, Ph.D.
Member

Kevin Gross, Ph.D.
Member

AFIT-ENY-DS-18-S-059

Abstract

The current resurgence of interest in hypersonic technologies has warranted an inquiry into the commonly employed thermochemical non-equilibrium models within computational fluid dynamic (CFD) simulations. Additionally, research has historically focused on forebody flow-fields, while studies of the complex wake structure have remained elusive. Although the forebody is of significance for vehicle analysis, the wake presents many exploitative characteristics. This dissertation aimed to address these two deficits. First, two three-temperature non-equilibrium models were developed, increasing the fidelity of hypersonic solutions above that of the legacy two-temperature model. The models were then investigated via zero-dimensional simulations, to detail the non-equilibrium processes, and ultimately implemented within a CFD architecture and validated against the RAM C-II flight test data. Compared against the two-temperature, the three-temperature models were shown to capture additional physics of the non-equilibrium phenomena; thus, the accuracy of the predicted thermochemical state increased. Second, a parametric study characterizing the wake behind a generic, slender geometry was completed, where the non-equilibrium processes were shown to extend a significant distance into the wake. The complex wake structure, coupled with the high-fidelity three-temperature model, has implications on radiative heating, communications blackout, and remote detection predictions.

To my wife,

for her endless love and support.

Acknowledgements

The work within this dissertation would not have been possible without the counsel of my advisor, Dr. Robert Greendyke. His sage advice proved to be invaluable in this effort, and I am grateful for it. Thanks is also owed to Dr. Peter Gnoffo and the Aerothermodynamics Branch at NASA Langley for their insightful comments and making available the FUN3D CFD software. Additionally, I am indebted to Maj Darrell Crowe, Maj Brook Bentley, Dr. Kevin Gross, and Maj Jeffrey Komives for their knowledge and guidance regarding my research.

Matthew P. Clarey

Table of Contents

Page

List of Figures

List of Tables

List of Symbols

Symbol Page

Symbol		Page
$T_{t,s}$	transltional temperature for species s, with respect to the mass averaged velocity, K	19
T_v	vibrational temperature, K	17
T_{ve}	vibrational-electronic temperature, K	17
u^i	mass-averaged velocity, $m\,s^{-1}$	18
u_s^i	average velocity of species s, $m\,s^{-1}$	18
V	volume, m^3	36
V_s^i	diffusion velocity of species s, $m\,s^{-1}$	19
$\dot{w}_e^{hpci}$	mass rate of production of electrons from heavy-partical collision ionization reactions, $kg\,m^{-3}\,s^{-1}$	34
$\dot{w}_s$	mass rate of production of species s per unit volume, $kg\,m^{-3}\,s^{-1}$	24
X_s	mole fraction of species s	21
Z_s	net charge of the species s	22

List of Abbreviations

Abbreviation		Page
AD	approximate diffusion	105
AOTV	aeroassisted orbital transfer vehicle	9
CFD	computational fluid dynamics	3
DES	detached-eddy simulation	10
DoD	Department of Defense	1
DPLR	Data Parallel Line Relaxation	6
DSMC	direct simulation Monte-Carlo	3
FUN3D	Fully Unstructured Navier-Stokes in Three-Dimensions	3
HARA	High-Temperature Aerothermodynamic Radiation Algorithm	147
ISR	intelligence, surveillance, and reconnaissance	1
LAURA	Langley Aerothermodynamic Upwind Relaxation Algorithm	6
LES	large-eddy simulation	148
MD	multicomponent diffusion	105
MMD	multi-temperature multicomponent diffusion	105
NASA	National Aeronautics and Space Administration	1
RAM	Radio Attenuation Measurements	11
STS	state-to-state	6
US3D	Un-Structured 3D	3

THERMOCHEMICAL NON-EQUILIBRIUM MODELS FOR WEAKLY IONIZED HYPERSONIC FLOWS WITH APPLICATION TO SLENDER-BODY WAKES

I. Introduction

In recent years, hypersonic technologies have seen a growth in interest within the United States Department of Defense (DoD) and has been labeled a game-changing technology [2]. Hypersonic speeds, or traveling faster than five times the speed of sound ($M > 5$), pose several challenges to vehicle design due to the extreme temperatures and aerodynamic forces they encounter. Overcoming these challenges, however, is worth the effort because both air breathing and boost glide vehicles offer unprecedented intelligence, surveillance, reconnaissance (ISR) and strike capabilities [1, 87]. Additionally, foreign powers have been "investing heavily in hypersonic technologies" [36] thus necessitating the DoD to also explore defense strategies against hypersonic systems [34, 88]. Hypersonics is the new frontier of military power and successful implementation of this technology will have its foundations in the detailed knowledge of the complex flow-field around these vehicles.

Historically, hypersonic aerodynamics have been almost exclusively associated with planetary entry vehicles such the Apollo capsule or Space Shuttle of the National Aeronautics and Space Administration (NASA). The design objective for this application is to decelerate through the hypersonic regime for safe recovery, thus the vehicles are generally blunt to increase drag and spread the extreme heat load across the forebody. Blunt configurations have been studied in depth for decades with particular focus on forebody flow-fields where the heat transfer rate is exceptionally high. However, unlike planetary entry vehicles, the objectives for a military application are

generally to maximize speed and range, which lead to slender configurations. These geometries result in concentrated locations on the nose and leading edges of extremely high temperatures. Additionally, the stability of these vehicles is more uncertain and high-fidelity simulations of the entire flow-field around the vehicle are generally warranted.

The complexity of hypersonic flows stems from the massive amount of kinetic energy present in the fluid which increases quadratically with speed [84, 104]. As the fluid passes through the strong bow shock wave, which is characteristic of the hypersonic regime, the bulk fluid kinetic energy is transfered into the translational and internal energy modes of the constituent gas species. The thermal energy, or temperature, of the fluid then drives chemical reactions and the composition of the gas changes. However, all of these processes require a finite amount of time to reach equilibrium values. As the speed of the vehicle increases, the residence time of a fluid element decreases and the thermochemical state of the gas increasingly becomes in a state of non-equilibrium throughout the domain. The modeling of this energy cascade is of prime importance to the overall solution accuracy of any simulation of a hypersonic flow-field.

Another consideration is that hypersonic vehicles fly at very high altitudes. At some point, as altitude increases, the fluid domain transitions from continuum to free-molecular flow and the applicability of the chosen computational method may be questionable. The Knudsen number is the ratio of the molecular mean free path, λ, to a characteristic length, L_{ref}, and is given by

$$Kn = \frac{\lambda}{L_{ref}}. \tag{1}$$

Generally, if the Knudsen number is less than 0.01 the continuum fluid dynamics assumption is valid [18, 19]; however, for a Knudsen number greater than 0.01, the

continuum assumption begins to break down and individual molecular dynamics need to be considered. Standard computational fluid dynamics (CFD) methods are applicable for continuum flows while the more computationally expensive direct simulation Monte-Carlo (DSMC) method is applicable across all regimes. Assessing the continuum assumption is especially important for wake flows due to the potential situation where the forebody flow may be within the continuum regime, where CFD methods are applicable, while the local Knudsen number within the wake indicates transition to the free-molecular regime, where the DSMC method would be more appropriate.

CFD is used heavily in the field of hypersonics due to its low financial impact compared to flight or wind tunnel testing and the ability to easily complete parametric studies. Fully Unstructured Navier-Stokes in Three-Dimensions (FUN3D), developed by NASA Langley [12, 41], and Un-Structured 3D (US3D), developed by the University of Minnesota and NASA Ames [23], are two state-of-the-art CFD codes that are capable of simulating hypersonic flows. The physical models between these two codes are very similar: both solve the Navier-Stokes equations for mixtures of gases in thermochemical non-equilibrium. However, there still exists a fair amount of uncertainty in the final solution of any simulation. As an example, Wright, Milos, and Tran [110] posit that the uncertainty in the heating rate for the forebody of a given vehicle is on the order of 15% to 30% and between 50% to 300% for the afterbody. This example highlights the need for higher-fidelity physics models as well as extending research of the flow-field into the wake of the vehicle.

According to Park [84], the accuracy of the thermochemical non-equilibrium model affects the prediction of four important wake features: radiative heating to the afterbody, aerodynamic coefficients of the vehicle, electron number-density which in turn is used for the prediction of radio communication interference and remote detection, and optical radiation for visual tracking of the vehicle. All of these points concerning

the wake are of importance to the DoD, which could benefit from research in this area. To this end, this dissertation is focused on characterizing the structure and thermochemical state of the wake behind a slender, hypersonic vehicle using a newly developed, high-fidelity, thermochemical non-equilibrium model.

1.1 Non-Equilibrium Modeling

This research focuses on weakly ionized plasmas in thermochemical non-equilibrium; such a plasma is composed of neutral, ionic, and free-electron species. The neutral and ionic species are either single atom molecules, which contain translational and electronic energies, or multi-atom molecules, which additionally contain rotational and vibrational energies. The free electrons possess only translational energy. The transfer of energy into or out of a particular mode occurs through molecular collisions or electromagnetic radiation [4, 84, 104]. Considering only collisional processes, the transfer of translational and rotational energy between the molecules takes very few collisions (< 5) before equilibrium among the surrounding molecules is obtained. On the other hand, vibrational, electronic, and chemical processes take many more collisions to equilibrate ($>$10,000). Additionally, due of the mass disparity between free electrons and the other heavier particles, the transfer of translational energy between the two takes considerably more collisions than for two like-massed particles [6, 100, 104]. The energy of each mode is dictated by quantum mechanics and transitions between states of each mode are governed by the master equation [30, 84], however, individual states and energy modes that are tightly coupled, that have quick relaxation processes between them, can be grouped together into a single manifold. Thus, the non-equilibrium phenomena is reduced to a smaller, more manageable, set of equations.

In the 1960's, the conservation equations for three-component, weakly ionized plas-

mas consisting of neutral, ionic, and free-electron species were developed by Appleton and Bray [6]; a similar set of equations was also presented by Sutton and Sherman [100]. In this model, the translational temperatures of the heavy neutral and ionic species were considered to be the same while the electron temperature was allowed to be independent. The final form of the conservation equations did not include contributions from viscous or thermal conduction terms nor any internal degrees of freedom for the neutral or ionic species. These limitations, as well the need to model a more complex mixture of chemically reacting gases, make the direct application of these conservation equations inappropriate for the flows under consideration in this work. However, the development of a separate free-electron energy equation was a significant contribution and of prime importance in the present work.

Two decades later, in the 1980's, Lee [62] developed a set of conservation equations appropriate for hypersonic, weakly ionized flows in thermochemical non-equilibrium. The internal energy of the gas constituents was considered by grouping tightly coupled modes together into three separate manifolds. First, the rotational energy of the polyatomic molecules was considered to be equilibrated with the translational energy at a translational-rotational temperature. Second, the vibrational energy of the polyatomic species was considered to be in a Boltzmann distribution at a common vibrational temperature. Lastly, the electronic energy for the bound electrons was considered to be in a Boltzmann distribution and tightly coupled to the translational energy of the free electrons at an electron-electronic temperature. This three-temperature model has been the foundation of most, if not all, subsequent thermochemical non-equilibrium models and its impact on the field can not be overstated.

Due to the uncertainties in the energy exchange rates for Lee's three-temperature model, Park [80, 81, 82] proposed a simplified two-temperature model, which considered the vibrational, electronic, and free-electron energy to be in equilibrium at the

same temperature. The single vibrational-electronic-electron manifold was justified because of the efficient energy exchange process between the free-electron translational energy and the vibrational energy of the molecules, specifically the nitrogen molecule (N_2) [63, 84]. This two-temperature model has been the basis for the most prevalent hypersonic CFD codes such as FUN3D [12, 41] and US3D [23] as well as their respective predecessors: Langley Aerothermodynamic Upwind Relaxation Algorithm (LAURA) [70] and Data Parallel Line Relaxation (DPLR) [108].

The accuracy of the previous models relies on the existence of a common vibrational temperature. This assumption can be relaxed by considering a multi-species multi-temperature model, which defines a separate vibrational temperature for each polyatomic molecule present. The introduction of additional energy equations results in the need for exchange rates between each vibrational mode, however, there is a considerable amount of uncertainty associated with the few rates that are available [84]. Several researchers, including Candler and MacCormack [24], Josyula and Bailey [56], and Martin [69], have used this thermochemical model for the simulation of hypersonic flows in air. Their results showed that the vibrational temperatures of the diatomic molecules were very similar throughout the shock layer, which demonstrates the strong coupling between the vibrational modes of the diatomic species. Therefore, Park [84] suggests that the inclusion of additional vibrational temperatures does not increase the solution fidelity enough to be worth the added computational cost.

Additional non-equilibrium models gaining interest are state-to-state (STS) kinetic models that couple the fluid dynamics equations to the master equation to account for the quantum state of each species [57]. An additional mass transport equation is required for each quantum number considered; thus, the energies of the internal modes are permitted to have non-Boltzmann distributions. Determining the numerous transition rates for all the states to be considered from *ab initio* methods

is an area of active research. Even though STS models have a lot of potential for the simulation of non-equilibrium flows, the availability of the transition rates and the enormous increase in computation cost make them prohibitive for practical problems at this time.

Considering that the current study is concerned with the investigation of hypersonic wake-flows behind slender bodies, where the computational domain was large and numerous simulations were to be completed, a computationally efficient thermochemical model was of prime importance. Therefore, models similar to the three-temperature model of Lee [62], from which the widely accepted two-temperature model was derived, were explored.

1.2 Hypersonic Wakes

The wake behind a hypersonic vehicle is a complex flow-field due to thermal and chemical non-equilibrium effects, a large recirculation zone, instabilities that lead to transitional or turbulent flows, the possibility of rarefaction, and the addition of forebody ablation products contaminating the flow-field. A schematic for the wake behind a sphere at hypersonic speeds is shown in Figure 1; the characteristics of the structure are presented by Lees [65], Lykoudis [67], Park [84], and Gnoffo [37]. As a fluid element travels through the shock wave the translational energy increases according to the Rankine-Hugoniot shock relations [3]. Then, an energy cascade proceeds from the translational to the internal energy modes and through chemical reactions. The wake structure begins as the fluid element is processed by an expansion zone as the flow turns from the forebody, over the vehicle shoulder, to the afterbody. This expansion quickly decreases the mass density and translational energy through the Prandtl-Meyer relations [3]. The internal energy states begin to depopulate and reactions proceed as the thermochemical state equilibrates with the low translational

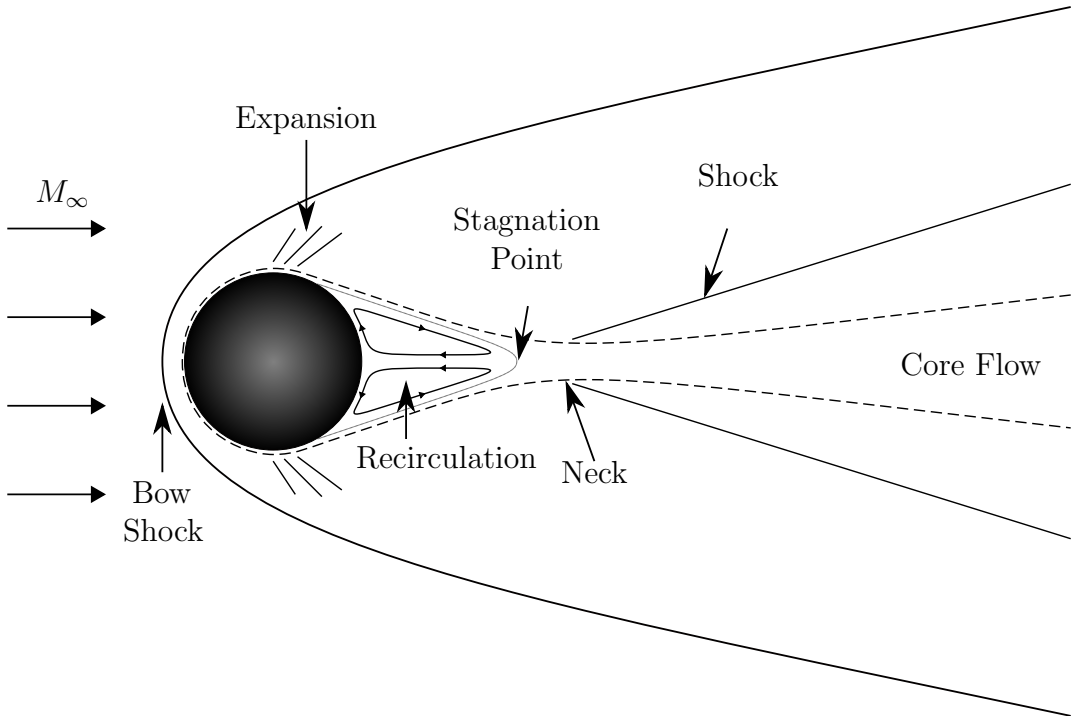

Figure 1. Hypersonic wake structure.

temperature. Through the expansion over the vehicle shoulder the flow separates creating a free-shear layer and recirculation zone. The shear layer coalesces to the rear stagnation point, where the flow velocity is zero relative to the body. The collapse of the near wake creates a neck region where the gas is compressed and heated before progressing downstream. The flow outside the shear layer is supersonic and turns near the neck region, thus dictating the formation of a shock wave which leads to additional non-equilibrium phenomena. This complex wake structure is of interest in this study due to the potential for a population inversion within the internal states and the presence of free-electrons far downstream.

Research concerning hypersonic wakes exploded in the 1960's when numerous theoretical and experimental investigations on the wake behind blunt and slender vehicles were undertaken. Lykoudis [67] conducted a thorough review of more than 180 papers, covering the beginning years of the 1960's, pertaining to wake flow-fields.

He indicated that this interest stemmed from a military need to understand the hypersonic re-entry phenomena of ballistic missiles. In particular, estimates for vehicle size, shape, weight, and aerodynamic performance could be made if the details for the wake structure, including the far wake, could be determined. Of the voluminous amount of papers during the time, a few are briefly described in order to highlight the trends in research. Dealing with the far wake, Lees [65] developed scaling laws for laminar-turbulent transition and electron densities behind blunt and slender bodies. Similarly, Behrens published a series of papers [9, 10] on the characteristics and stability of the far wake behind cylinders using experimental data and theoretical calculations. Concerning the near wake, Dewey [58] conducted an experimental campaign to investigate the recirculation zone, shear layer, and neck region. Additionally, ballistic range tests, like those of Taylor, Melcher, and Washburn [102] and Reis [95], were popular since the free-flight nature of the projectile meant the far wake could be investigated and theoretical models could be validated. As expected, the accuracy of the models during this time was poor and only general trends for the wake structure could be determined.

Through the 1970's, research concerning the wake of hypersonic vehicles diminished. However, the late 1980's, with the introduction of the aeroassisted orbital transfer vehicle (AOTV) concept, saw a regained interest in the wake structure because of the need to accurately calculate the flow-field for payload and afterbody heatshield sizing. Gnoffo, Price, and Braun [40] used an eleven-species, two-temperature thermochemical non-equilibrium model within a CFD framework to characterize the separation angle of the shear layer in order to predict the conditions that cause its impingement on the payload, which is critical for heating predictions. Trajectory points with velocities of approximately $9.5\,\mathrm{km\,s^{-1}}$ at 80 km altitude were considered. They showed that the shear layer deflection angle increased linearly with angle of

attack and seemed to have some dependence on gas chemistry. Additionally, their simulations predicted that local, aft heating levels were a factor of 10 higher with shear layer impingement. Due to the rarefied conditions expected for an AOTV vehicle, Wilmoth *et al.* [106], Dogra *et al.* [31], and Moss *et al.* [78] investigated the utility of the DSMC method to investigate the wake of a generic AOTV configuration at the conditions of a low density wind tunnel. One of their results indicated that the stable recirculation zone forms for flows with freestream Knudsen numbers less than or equal to 0.01 and grows in size as the flow transitions more into a continuum description. Additionally, Dogra *et al.* [32] showed that the inclusion of chemical reactions increased the overall size of the recirculation zone. These works, along with other similar wake investigations, showed the ability of computational methods to simulate hypersonic wake-flows and capture the expected physical characteristics.

Towards the end of the 1990's, the focus shifted to capsule-type vehicles and the prediction of heat loads to the afterbody. Grasso and Pirozzoli [44] investigated the thermochemical non-equilibrium effects of ionizing air on the near wake of sphere-cone and blunt vehicles. They concluded that the non-equilibrium processes along the forebody play a significant role in the recirculation zone size, base heating rates, and other near-wake characteristics. Wright *et al.* [107] computed the afterbody heating of the Fire II experiment and investigated the effect surface catalysis has on heating predictions. As expected, the heat flux to the body increased with increasing catalysis. Wright, Prabhu, and Martinez [112] conducted a thorough study for the afterbody heating to the Apollo capsule and compared the results to flight data. The simulations agreed well with 15 of the 19 working calorimeters to within $\pm 20\%$. Detached-eddy simulations (DES) were conducted by Brock, Subbareddy, and Candler [21] on a spherical capsule to investigate the unsteady nature of the massively separated flow-field of the wake. Heating predictions were in fairly good agreement to experimental

shock-tunnel data, and the ability of DES to resolve the unsteady nature of the wake was demonstrated. Johnston and Brandis [52] included radiative heating in their calculations of the Stardust and Fire II capsules and showed that afterbody radiation could contribute as much as convective heating. The aforementioned studies highlight the current research of wake flows behind blunt, capsule-like vehicles.

Significantly less research exists concerning wake flows behind slender vehicles compared to blunt bodies. One of the few investigations concerning slender bodies was by Lin *et al.* [66]. They characterized the near-wake structure, including base heating rates and pressure distributions, behind cones at angle of attack. Another study was completed by Barnhardt and Candler [8], who used DES to simulate the flow-field around the Reentry-F vehicle. The results agreed well with flight test data for both heating rates and pressure distribution and showed the utility of DES on modeling slender-body wakes. The lack of research concerning wakes behind slender bodies represents a knowledge gap within the field of hypersonic aerodynamics.

Hypersonic wake flows have been of interest for several decades. However, wakes behind slender bodies have not been thoroughly studied using modern computational techniques. Additionally, of the few studies that do exist, none have explored the effects that the non-equilibrium model has on the thermochemical state of the fluid within the wake.

1.3 RAM C-II Flight Experiment

In the 1960's, NASA conducted a series of tests investigating the plasma sheath that envelopes hypersonic vehicles. Their primary concern was interference with communication equipment, or radio blackout [55]. One of the most useful datasets from the Radio Attenuation Measurements (RAM) project was from the RAM C-II flight experiment, which measured the electron density in the flow-field using microwave re-

flectometers and electrostatic probes. Other experimental measurements, especially from flight tests, of electron densities within hypersonic flows are scarce, making the RAM C-II that much more important. The RAM C-II was a spherically-blunted cone with a nose diameter of 30.48 cm, a cone half angle of 9 degrees, and an overall body length of 129.54 cm. The vehicle attained a maximum speed of approximately 7,620 $\mathrm{m\,s^{-1}}$ with data being collected over the altitude range of 85.3 km to 53.3 km. The data from this flight test have been used by numerous researchers to validate their respective thermochemical non-equilibrium models [24, 33, 38, 43, 44, 56, 59, 91]. The accurate prediction of the electron density within a hypersonic flow-field is the result of a model accurately capturing numerous thermochemical phenomena. Thus, in agreeing well with experimentally determined electron densities, the confidence that the model captures all relevant physics is increased. Therefore, simulations of the 61 km and 71 km trajectory points of the RAM C-II were used to validate the three-temperature models developed in this dissertation by comparison to the experimental data.

1.4 Research Objectives

The overarching objective of this dissertation is to advance the understanding of wake flow-fields behind hypersonic vehicles by characterizing the thermo-chemical state and structure of slender-body wakes with a high-fidelity, three-temperature thermochemical non-equilibrium model. Research in this area aids in improving aerodynamic, afterbody heating, electron number-density, and optical radiation predictions. Towards these ends, two three-temperature thermochemical non-equilibrium models were developed and their predicted processes were investigated in detail. The models were then integrated and validated within a CFD architecture and utilized in a study investigating the wake behind a slender, hypersonic vehicle.

The contents of this dissertation are aligned against the following four research objectives:

> **Research Objective 1:** Develop two three-temperature thermo-chemical non-equilibrium models appropriate for weakly ionized hypersonic flows.
>
> **Research Objective 2:** Detail the thermochemical non-equilibrium processes, predicted by the newly developed three-temperature models, within zero-dimensional simulations considering both heating and cooling processes.
>
> **Research Objective 3:** Implement the three-temperature models within FUN3D and validate them against the RAM C-II flight test data. Additionally, extend the simulation downstream to assess the models capability to accurately capture the physics within the wake.
>
> **Research Objective 4:** In order to characterize the thermochemical non-equilibrium phenomena within the wake, conduct a parametric study, varying angle of attack and altitude, of a slender, spherically-blunted cone at hypersonic speeds

Research supporting the completion of these objectives is presented in the chapters that follow. Chapter II discusses the relevant theory and develops two three-temperature thermochemical non-equilibrium models. Chapter III presents the results of the zero-dimensional simulation investigation. Implementation within a CFD architecture and validation against the RAM C-II flight test data is detailed in Chapter IV. The investigation of the wake behind a slender, hypersonic cone at angle of attack is presented in Chapter V. Finally, Chapter VI draws conclusions on the present study and presents avenues for future work to explore.

II. Theory and Methodology

The development of the equations governing the fluid dynamics of hypersonic flows begins by considering the well established kinetic theory of gases [27, 104]. The foundations of which are based on the construct that, on the microscopic level, a gas is made up of continuously moving and colliding particles. Bulk fluid properties are obtained by averaging over the molecules at a given location, and the macroscopic conservation equations are derived by taking moments of the Boltzmann equation.

The thermal energy of a molecule is composed of contributions from the random, translational motion of the particle, ϵ_t, and the internal energy, ϵ_{int} [104]. Monatomic species have one internal mode: the electronic energy associated with the bound electrons, ϵ_e. Polyatomic molecules have two additional internal modes: rotational energy from the tumbling motion of the molecules, ϵ_r, and vibrational energy from the oscillating behavior between the atoms, ϵ_v. The total thermal energy of a given particle is thus

$$\epsilon = \epsilon_t + \epsilon_{int},$$

where, for an atom $\epsilon_{int} = \epsilon_e$, and for a polyatomic molecule $\epsilon_{int} = \epsilon_r + \epsilon_v + \epsilon_e$. A free-electron's thermal energy is composed of only the translational motion of the electron, ϵ_t.

The partition of energy among each mode and the processes which transfer energy into and out of each mode are dictated by quantum mechanics [62, 84, 104]. The exchange of translational energy, between molecules of similar mass, is a very quick process and equilibrium between all like-massed particles is reached in less than five collisions. Therefore, at every spatial location, the translational energy of all particles, excluding free-electrons, is assumed to be commensurate with the translational temperature, T_t. The rotational energy of the polyatomic species similarly equilibrates

in less than ten collisions for like-massed particles leading to a common rotational temperature, T_r. Additionally, there is a strong coupling between the translational and rotational energies and are commonly assumed to be equilibrated at a single translational-rotational temperature, $T_{tr} = T_t = T_r$. Note that this dissertation considers ionized air. If a different gas mixture was under consideration, which contained hydrogen or helium, the translational and rotational energy equilibrium assumption may not be appropriate due to the mass disparity of these species compared to others which may be present.

Following the work of Lee [62] and Park [84], the vibrational and electronic energies of each species are assumed to follow Boltzmann distributions at a vibrational (T_v) and electronic ($T_{el.}$) temperature, respectively. The existence of a common vibrational temperature is assumed due to the quick vibrational energy exchange process between the species. The existence of a common electronic temperature is similarly reasoned. As can be seen in the work of Candler and MacCormack [24] or Josyula and Bailey [56], who modeled the diatomic species vibrational energy as separate equations, the vibrational temperatures of each species are closely coupled, suggesting that they can be sufficiently described by a single vibrational temperature.

The energy contained within the translational mode of the free-electrons is treated as a separate energy mode and is assumed to be equilibrated at an electron temperature, T_e. Translational energy exchange is most efficient among particles of like-mass, and since an electron's mass is much smaller than that of the other species, the translational modes of the electrons and other molecules do not quickly equilibrate [84, 100]. However, there are strong mechanisms for free-electron energy coupling with vibrational and electronic states [62, 84]. As an electron impacts a polyatomic molecule, the electromagnetic field holding the molecule together is altered, which changes the vibrational characteristics of the bound nuclei and thus the exchange of energy with

the free-electron becomes probable. The electron-impact electronic-excitation process results in a strong coupling between these energy modes because, when an electron encounters a molecule, there is a high probability of the free-electron and the bound electrons, due to their equality in mass, interacting and exchanging energy.

The two three-temperature thermochemical non-equilibrium models proposed in this dissertation are differentiated by how the electronic energy is partitioned. The first model, the free-electron three-temperature model follows along the work of Appleton and Bray [6] and considers a wholly separate free-electron energy equation. Thus, the vibrational and electronic energies are grouped together and a common vibrational-electronic temperature, $T_{ve} = T_v = T_{el.}$, is assumed to fully describes the energy within these modes. The three-temperatures that compose this model are the translational-rotational (T_{tr}), vibrational-electronic (T_{ve}), and free-electron (T_e) temperatures. This model is suitable for very weakly ionized flows where, due to the insufficient number of free-electrons, the electron-impact electronic-excitation process is not the dominant exchange mechanism to the electronic energy.

The second three-temperature model is termed the electron-electronic model. This model follows the work of Lee [62] in that the electronic energy is grouped with the free-electron energy and assumed to be equilibrated at a electron-electronic temperature, $T_{ee} = T_{el.} = T_e$. The three-temperatures of the electron-electronic model are the translational-rotational (T_{tr}), vibrational (T_v), and electron-electronic (T_{ee}) temperatures. As ionization levels increase, the electron-impact electronic-excitation process becomes more probable, leading to a strong coupling between the free-electrons and the electronic states of the gas species, and the electron-electronic model becomes more applicable than the free-electron model.

Although these models are applicable to hypersonic flows through any gas mixture, particular attention is given to mixtures commensurate to Earth's atmosphere

(79% N_2 and 21% O_2). An eleven-species air model was considered which included the following species: N_2, O_2, N, O, NO, N_2^+, O_2^+, N^+, O^+, NO^+, e^-. Realizing that for lower speed flows NO^+ is the major ion constituent present, a seven-species model is also popular: N_2, O_2, N, O, NO, NO^+, e^-. As the fluid velocity increases, the applicability of the gas model changes from the seven-species to the eleven-species model. The line of demarcation for the transition point between these two models is ill-defined, and realizing that the electron energy is highly coupled to the number of free electrons the eleven-species model should be given preference.

The following sections present the derivation of the conservation equations. First, the velocity distribution function is introduced along with the relevant mixture averages in Sections 2.1 and 2.2, respectively. The Boltzmann equation is then presented in Section 2.4 and used to obtain the important equation of change in Section 2.6. The equations for the conservation of mass, momentum, and energy are developed in Section 2.7. In order to close the equation set, the necessary thermodynamic relations, collision frequencies, relaxation times, chemical kinetic equations, electric field model, and transport properties are detailed in Sections 2.8 through 2.12. The final form of the governing equations for each non-equilibrium model considered is presented in Section 2.14. Lastly, the numerical implementation of the finite volume formulation is discussed in Section 2.15.

2.1 The Velocity-Distribution Function

The velocity-distribution function of species s is denoted by $f_s(x^i, c^i, t)$ and is a function of position (x^i), velocity (c^i), and time (t) [27, 48]. It is defined such that the probable number of molecules of species s in the volume $d\mathbf{x} \equiv dx^1 dx^2 dx^3$ containing the point x^i, with a velocity in the range $d\mathbf{c} \equiv dc^1 dc^2 dc^3$ about the value c^i, and at

time t is equal to

$$f_s(x^i, c^i, t)d\mathbf{x}d\mathbf{c}. \tag{2}$$

2.2 Averages and Mixture Properties

The number-density of species s, n_s, is found by integrating the velocity-distribution function over the entire velocity space

$$n_s = \iiint_{-\infty}^{\infty} f_s(x^i, c^i, t)dc^1dc^2dc^3 \equiv \int f_s d\mathbf{c}. \tag{3}$$

Additionally, consider ϕ be any molecular property that is a function of position, velocity, and time ($\phi = \phi(x^i, c^i, t)$); then the average value of ϕ at x^i and t is

$$n_s\langle\phi\rangle_s = \int \phi f_s d\mathbf{c}. \tag{4}$$

The mass-density and average velocity of species s are then

$$\rho_s = m_s n_s \tag{5}$$

and

$$u_s^i = \langle c^i \rangle_s, \tag{6}$$

respectively, where m_s is the mass of species s. The mixture density is thus

$$\rho = \sum_s \rho_s, \tag{7}$$

and the mass-averaged velocity is

$$u^i = \frac{1}{\rho}\sum_s \rho_s u_s^i, \tag{8}$$

where the summation of s is over all species in the mixture.

The thermal, or peculiar, velocity with respect to the mass-averaged velocity is

$$C^i = c^i - u^i. \tag{9}$$

Thus, the diffusion velocity of species s is

$$V_s^i = \langle C^i \rangle_s = u_s^i - u^i. \tag{10}$$

Multiplying Equation (10) by ρ_s, summing over all species, and utilizing Equation (8) leads to

$$\sum_s \rho_s V_s^i = 0. \tag{11}$$

The thermal, translational energy of a particle is [27]

$$\epsilon_t = \frac{1}{2} m_s C^i C^i, \tag{12}$$

and the average translational energy for species s, per unit mass, is

$$e_{t,s} = \frac{1}{m_s} \big\langle \epsilon_t \big\rangle_s = \frac{1}{2} \big\langle C^i C^i \big\rangle_s. \tag{13}$$

The translational temperature is a measure of the average kinetic energy in the random motion of the gas particles [27, 104]. The translational temperature of species s, $T_{t,s}$, is defined by the relation [100]

$$\frac{3}{2} n_s k T_{t,s} = \rho_s e_{t,s} = \frac{1}{2} \rho_s \big\langle C^i C^i \big\rangle_s, \tag{14}$$

where k is the Boltzmann constant. Similarly, the electron temperature is defined by

$$\frac{3}{2}n_e k T_e = \rho_e e_{t,e} = \frac{1}{2}\rho_e \left\langle C^i C^i \right\rangle_e. \tag{15}$$

The Boltzmann constant is related to the universal gas constant, $\hat{R}$, via

$$\hat{R} = k\hat{N}, \tag{16}$$

where $\hat{N}$ is Avogadro's number. The thermal translational energy for each species, except free-electrons, is assumed to be equilibrated; therefore,

$$T_{t,s} = T_t \quad \left(s \neq e^-\right). \tag{17}$$

The partial pressure of each species is [27, 100]

$$p_s = n_s k T_t \quad \left(s \neq e^-\right) \quad \text{and} \quad p_e = n_e k T_e. \tag{18}$$

Using Dalton's Law of partial pressure, the total pressure is

$$p = \sum_s p_s. \tag{19}$$

The ratio of the mass of a particular species to the total mass of the mixture, or mass fraction, is

$$c_s = \frac{\rho_s}{\rho}. \tag{20}$$

Likewise, the ratio of the moles of species s to the total number of moles of the

mixture, or mole fraction, is

$$X_s = \frac{n_s}{\sum\limits_k n_k} = \frac{\rho_s/m_s}{\sum\limits_k \rho_k/m_k}. \tag{21}$$

The average internal energy of species s, per unit mass, is

$$e_{int,s} = \frac{1}{m_s}\left\langle \epsilon_{int} \right\rangle_s. \tag{22}$$

Similar expressions exist for the particular internal energy modes. The total thermal energy of species s is

$$e_s = e_{t,s} + e_{int,s}, \tag{23}$$

and the average thermal energy of the mixture is

$$e = \sum_s c_s e_s. \tag{24}$$

There exists similar expressions for the mixture averaged translational (e_t), rotational (e_r), vibrational (e_v), and electronic (e_e) energy modes:

$$e_t = \sum_s c_s e_{t,s}, \quad e_r = \sum_s c_s e_{r,s}, \quad e_v = \sum_s c_s e_{v,s}, \quad \text{and} \quad e_e = \sum_s c_s e_{e,s}. \tag{25}$$

2.3 External Forces

The force on a gas particle from external sources is denoted by $m_s F_s^i$ and include gravitational and electromagnetic, both externally applied and induced, forces. The electromagnetic force can be decomposed into two parts: the coulombic force from the electric field, E^i, and the ampere force from the magnetic field, B^i [100]. Therefore

the force on a given particle is

$$m_s F_s^i = m_s g^i + \mathsf{e} Z_s \left(\mathsf{E}^i + \epsilon^{ijk} c^j \mathsf{B}^k \right), \tag{26}$$

where g^i is the acceleration due to gravity, e is the charge of an electron, Z_s is the net charge of the particle, and ϵ^{ijk} is the permutation symbol.

2.4 The Boltzmann Equation

The evolution of the velocity-distribution function is governed by the Boltzmann equation. Its derivation is presented in texts concerning the kinetic theory of gases such as those by Chapman and Cowling [27] and Hirschfelder, Curtiss, and Bird [48] and is therefore omitted in the present work. The Boltzmann equation for species s is

$$\frac{\partial f_s}{\partial t} + c^i \frac{\partial f_s}{\partial x^i} + F_s^i \frac{\partial f_s}{\partial c^i} = \frac{\partial_e f_s}{\partial t}, \tag{27}$$

where $(\partial_e f_s / \partial t)$ is the rate of change of f_s from molecular encounters.

2.5 Maxwellian Distribution Function

If the gas is quiescent, an analytical solution to the Boltzmann equation, Equation (27), can be obtained for the velocity-distribution function, which is termed the Maxwellian distribution. Neglecting external forces, the Maxwellian velocity-distribution function for species s is [27]

$$f_s^{(0)} = n_s \left(\frac{m_s}{2\pi k T_{t,s}} \right)^{3/2} \exp \left[-\frac{m_s C^i C^i}{2 k T_{t,s}} \right]. \tag{28}$$

The average thermal speed of molecule s can then be found from Equation (4)

$$\left\langle C \right\rangle_s = \left(\frac{8kT_{t,s}}{\pi m_s} \right)^{1/2}. \tag{29}$$

2.6 Moments of the Boltzmann Equation

Multiplying the Boltzmann equation by any function of velocity, $\phi(c^i)$, and integrating over velocity-space leads to [27]

$$\int \phi \frac{\partial f_s}{\partial t} d\mathbf{c} + \int \phi c^i \frac{\partial f_s}{\partial x^i} d\mathbf{c} + \int \phi F_s^i \frac{\partial f_s}{\partial c^i} d\mathbf{c} = n_s \Delta \langle \phi \rangle_s, \tag{30}$$

where the collisional exchange term,

$$n_s \Delta \langle \phi \rangle_s = \int \phi \frac{\partial_e f_s}{\partial t} d\mathbf{c}, \tag{31}$$

represents the change of ϕ from encounters. The first term on the left can be simplified via

$$\int \phi \frac{\partial f_s}{\partial t} d\mathbf{c} = \frac{\partial}{\partial t} \int \phi f_s d\mathbf{c} = \frac{\partial}{\partial t} \left(n_s \langle \phi \rangle_s \right).$$

Likewise the second and third terms become

$$\int \phi c^i \frac{\partial f_s}{\partial x^i} d\mathbf{c} = \frac{\partial}{\partial x^i} \int \phi c^i f_s d\mathbf{c} = \frac{\partial}{\partial x^i} \left(n_s \langle \phi c^i \rangle_s \right)$$

and

$$\int \phi F_s^i \frac{\partial f_s}{\partial c^i} d\mathbf{c} = -n_s \left\langle F_s^i \frac{\partial \phi}{\partial c^i} \right\rangle_s.$$

After substituting these relations back into Equation 30, the equation of change

of any molecular property, ϕ, is obtained

$$\frac{\partial}{\partial t} n_s \langle \phi \rangle_s + \frac{\partial}{\partial x^i} n_s \langle c^i \phi \rangle_s - n_s \left\langle F_s^i \frac{\partial \phi}{\partial c^i} \right\rangle_s = n_s \Delta \langle \phi \rangle_s. \tag{32}$$

The equation of change is the beginning point for the derivation of the governing equations. The conservation of mass, momentum, and energy of a single species can be obtained by letting ϕ equal the mass, momentum, and energy, respectively, of a given molecule. The mixture momentum and energy conservation equations are then obtained by summation of the individual species equations.

2.7 Conservation Equations

2.7.1 Conservation of Species Mass

The conservation of mass of species s is obtained by setting $\phi = m_s$ within Equation (32):

$$\frac{\partial}{\partial t} \rho_s + \frac{\partial}{\partial x^i} \rho_s \left\langle c^i \right\rangle_s = n_s \Delta \left\langle m_s \right\rangle_s.$$

The term on the right side, the collisional exchange term, accounts for the possibility of chemical reactions producing or consuming species s and is represented as

$$n_s \Delta \left\langle m_s \right\rangle_s = \dot{w}_s.$$

With the use Equations (6) and (10), the conservation of mass of species s becomes

$$\frac{\partial}{\partial t} \rho_s + \frac{\partial}{\partial x^i} \rho_s \left(u^i + V_s^i \right) = \dot{w}_s. \tag{33}$$

2.7.2 Conservation of Momentum

The equation for the conservation of momentum of species s is obtained by setting $\phi = m_s c^i$ in Equation (32):

$$\frac{\partial}{\partial t}\rho_s \langle c^i \rangle_s + \frac{\partial}{\partial x^j}\rho_s \langle c^i c^j \rangle_s - \rho_s \langle F_s^i \rangle_s = \rho_s \Delta \langle c^i \rangle_s.$$

The mixture momentum conservation equation is obtained by summation over all constituent species. The first term becomes

$$\sum_s \frac{\partial}{\partial t}\rho_s \langle c^i \rangle_s = \sum_s \frac{\partial}{\partial t}\rho_s \left(u^i + V_s^i\right) = \frac{\partial}{\partial t}\left[\rho u^i + \sum_s \rho_s V_s^i\right] = \frac{\partial}{\partial t}\rho u^i,$$

where the last equality is obtained from Equation (11). The second term is similarly simplified

$$\frac{\partial}{\partial x^j}\sum_s \rho_s \langle c^i c^j \rangle_s = \frac{\partial}{\partial x^j}\left(\rho u^i u^j + \mathtt{p}^{ij}\right),$$

where the pressure tensor is [27]

$$\mathtt{p}^{ij} = \sum_s \mathtt{p}_s^{ij} = \sum_s \rho_s \langle C^i C^j \rangle_s.$$

The hydrostatic partial pressure is the average of the trace of the pressure tensor [27]

$$p_s = \frac{1}{3}\mathtt{p}_s^{ii}.$$

Therefore, the pressure tensor can be rewritten as

$$\mathtt{p}^{ij} = p\delta^{ij} - \tau^{ji},$$

where Equation (19) has been utilized and the viscous stress tensor is given by

$$\tau^{ij} = \sum_s \tau_s^{ij}.$$

The third term, neglecting gravitational forces, is

$$-\sum_s \rho_s \left\langle F_s^i \right\rangle_s = -\sum_s n_s \mathsf{e} Z_s \left\langle \mathsf{E}^i + \epsilon^{ijk} c^j \mathsf{B}^k \right\rangle_s = -\rho_+ \mathsf{E}^i - \epsilon^{ijk} J^j \mathsf{B}^k,$$

where the total charge-density is

$$\rho_+ = \mathsf{e} \sum_s n_s Z_s \tag{34}$$

and the current-density is

$$J^i = \mathsf{e} \sum_s n_s Z_s u_s^i. \tag{35}$$

The collisional exchange term is

$$\sum_s \rho_s \Delta \left\langle c^i \right\rangle_s = 0$$

because momentum is conserved for each collision and summation over all collisions results in the vanishing of this term [27]. Therefore, the conservation of mixture momentum becomes

$$\frac{\partial}{\partial t} \rho u^i + \frac{\partial}{\partial x^j} \left(\rho u^i u^j + p \delta^{ij} - \tau^{ji} \right) = \rho_+ \mathsf{E}^i + \epsilon^{ijk} J^j \mathsf{B}^k. \tag{36}$$

2.7.3 Conservation of Total Energy

The conservation of total energy is obtained by setting $\phi = \frac{1}{2}m_s c^i c^i + \epsilon_{int}$ in Equation (32) and summing over all species [100]. The first term is

$$\frac{\partial}{\partial t}\sum_s n_s \left\langle \frac{1}{2}m_s c^i c^i + \epsilon_{int} \right\rangle_s = \frac{\partial}{\partial t}\sum_s \rho_s \left(\frac{1}{2}u^i u^i + e_s\right) = \frac{\partial}{\partial t}\rho E,$$

where

$$E = e + \frac{1}{2}u^i u^i.$$

The second term becomes

$$\frac{\partial}{\partial x^j}\sum_s n_s \left\langle \frac{1}{2}m_s c^i c^i c^j + \epsilon_{int} c^j \right\rangle_s = \frac{\partial}{\partial x^i}\left[Hu^i - u^i\tau^{ji} + q^i\right],$$

where $H = E + p/\rho$ and the heat flux vector is

$$q^i = \sum_s n_s \left\langle \left(\frac{1}{2}m_s C^j C^j + \epsilon_{int}\right) C^i \right\rangle_s = n_s \left\langle \epsilon C^i \right\rangle_s.$$

The third term simplifies via

$$\begin{aligned} -\sum_s n_s \left\langle F_s^j \frac{\partial}{\partial c^j}\left(\frac{1}{2}m_s c^i c^i + \epsilon_{int}\right) \right\rangle_s &= -\sum_s n_s \left\langle F_s^i m_s c^i \right\rangle_s \\ &= -\sum_s n_s \mathsf{e} Z_s \left\langle \mathsf{E}^i c^i + \epsilon^{ijk}\mathsf{B}^k c^i c^j \right\rangle_s = -J^i \mathsf{E}^i, \end{aligned}$$

where the vector identity $\epsilon^{ijk}a^j b^k a^i = 0$ has been utilized.

The collisional exchange term is

$$\sum_s n_s \Delta \left\langle \frac{1}{2}m_s c^i c^i + \epsilon_{int} \right\rangle_s = 0$$

because energy is conserved during collisions and summation over all collisions results

in the vanishing of this term [27]. Lastly, gas radiation is accounted for by subtracting Q_{rad} from the right side of the final conservation equation.

The conservation of total energy is, after substitution of the above terms,

$$\frac{\partial}{\partial t}\rho E + \frac{\partial}{\partial x^i}\rho H u^i = \frac{\partial}{\partial x^j}\left(u^i \tau^{ij} - q^j\right) + J^i \mathsf{E}^i - Q_{rad}. \tag{37}$$

2.7.4 Conservation of Vibrational Energy

The conservation of vibrational energy is obtained by setting $\phi = \epsilon_v$ in Equation (32) and summing over all species. The first term is

$$\frac{\partial}{\partial t}\sum_s n_s \left\langle \epsilon_v \right\rangle_s = \frac{\partial}{\partial t}\rho e_v,$$

and the second term is

$$\frac{\partial}{\partial x^i}\sum_s n_s \left\langle \epsilon_v c^i \right\rangle_s = \frac{\partial}{\partial x^i}\left(\rho e_v u^i + q_v^i\right),$$

where the vibrational heat flux vector is

$$q_v^i = \sum_s n_s \left\langle \epsilon_v C^i \right\rangle_s.$$

The third term vanishes since $\partial \epsilon_v / \partial c^i = 0$.

The last term captures the change in vibrational energy from several processes: exchange between the vibrational mode and translational, electronic, and free electron energies as well as the production of vibrational energy due to chemical reactions [84]. The energy exchange between the vibrational and the translational modes is modeled

using the Landau-Teller relaxation model and is [104]

$$\sum_{s=mol.} \rho_s \frac{e_{v,s}^{T_t} - e_{v,s}}{\tau_s^{t-v}},$$

where $e_{v,s}$ is the vibrational energy per unit mass of species s, $e_{v,s}^{T_t}$ is the vibrational energy evaluated at the translational temperature (T_t), and τ_s^{t-v} is the Landau-Teller relaxation time for translational-vibrational energies. Lee [62] derived a similar expression for the energy exchange between the vibrational energy and free-electrons:

$$\sum_{s=mol.} \rho_s \frac{e_{v,s}^{T_e} - e_{v,s}}{\tau_s^{v-e}}, \tag{38}$$

where $e_{v,s}^{T_e}$ is the vibrational energy evaluated at the electron temperature (T_e), and τ_s^{v-e} is the relaxation time for the vibrational-electron mechanism. The vibrational energy exchange with the electronic mode is represented simply by

$$Q_{v-el.}.$$

Lastly, the production of vibrational energy within the volume due to chemical reactions is [39]

$$\sum_{s=mol.} \dot{w}_s \hat{e}_{v,s},$$

where $\hat{e}_{v,s}$ is the average vibrational energy of a dissociating s molecule.

Additionally, heteroneculear molecules are subject to radiative processes [84]; which are represented by subtracting Q_{rad}^{v} from the right side of the final equation.

Therefore, the conservation equation for the vibrational energy becomes

$$\frac{\partial}{\partial t}\rho e_v + \frac{\partial}{\partial x^i}\rho e_v u^i = -\frac{\partial q_v^i}{\partial x^i} + Q_{v-el.} + \sum_{s=mol.}\left(\rho_s \frac{e_{v,s}^{T_t} - e_{v,s}}{\tau_s^{t-v}} + \rho_s \frac{e_{v,s}^{T_e} - e_{v,s}}{\tau_s^{v-e}} + \dot{w}_s \hat{e}_{v,s}\right) - Q_{rad}^v. \tag{39}$$

2.7.5 Conservation of Electronic Energy

The conservation of electronic energy is obtained by setting $\phi = \epsilon_e$ in Equation (32) and summing over all species. The first and second terms are

$$\frac{\partial}{\partial t}\sum_s n_s \left\langle \epsilon_e \right\rangle_s = \frac{\partial}{\partial t}\rho e_e$$

and

$$\frac{\partial}{\partial x^i}\sum_s n_s \left\langle \epsilon_e c^i \right\rangle_s = \frac{\partial}{\partial x^i}\left(\rho e_e u^i + q_{el.}^i\right),$$

respectively, where the electronic heat flux vector is

$$q_{el.}^i = \sum_s n_s \left\langle \epsilon_e C^i \right\rangle_s.$$

The third term vanishes since $\partial \epsilon_e / \partial c^i = 0$.

The last term captures the change in electronic energy by several volumetric processes: energy exchange with the heavy particle translational energy ($Q_{t-el.}$), energy exchange with the vibrational mode ($Q_{v-el.}$), electron-impact electronic-excitation ($Q_{el.-e}$), radiative processes ($Q_{rad}^{el.}$), and production from chemical reactions. The mechanism for electronic energy production from chemical reactions is

$$\sum_s \dot{w}_s \hat{e}_{e,s}, \tag{40}$$

where $\hat{e}_{e,s}$ is the average electronic energy of a reacting s molecule. Following Park,

[84], it is assumed that the products and reactants electronic energies are commensurate with the electronic temperature and $\hat{e}_{e,s} = e_{e,s}$.

Therefore, the conservation equation for the electronic energy becomes

$$\frac{\partial}{\partial t}\rho e_e + \frac{\partial}{\partial x^i}\rho e_e u^i = -\frac{\partial q_e^i}{\partial x^i} + \sum_s \dot{w}_s e_{e,s} + Q_{t-el.} - Q_{v-el.} + Q_{el.-e} - Q_{rad}^{el.}. \tag{41}$$

2.7.6 Conservation of Free-Electron Energy

The equation governing the conservation of free-electron energy is obtained by setting $\phi = \frac{1}{2}m_e c^i c^i$ in Equation (32). The first term in the resulting equation is [100]

$$\frac{\partial}{\partial t} n_s \Big\langle \frac{1}{2} m_s c^i c^i \Big\rangle = \frac{\partial}{\partial t}\rho_e \left(\frac{1}{2} u^i u^i + V_e^i u^i + e_{t,e} \right).$$

The second term becomes

$$\begin{aligned} &\frac{\partial}{\partial x^j} n_e \Big\langle \frac{1}{2} m_e c^i c^i c^j \Big\rangle_e \\ &\qquad = \frac{\partial}{\partial x^j}\left[\rho_e \left(\frac{1}{2} u^i u^i + e_{t,e} \right) u^j + \rho_e \left(\frac{1}{2} u^i u^i V_e^j + u^i V_e^i u^j \right) + u^i \mathsf{p}_e^{ij} + q_e^j \right], \end{aligned}$$

where $\mathsf{p}_e^{ij} = \rho_e \big\langle C^i C^j \big\rangle_e = p_e \delta^{ij} - \tau_e^{ji}$ and $q_e^j = \frac{1}{2}\rho_e \big\langle C^i C^i C^j \big\rangle_e$ are the free-electron pressure tensor and heat flux vector, respectively. The third term, considering only electromagnetic forces, is

$$-n_e \left\langle F_e^j \frac{\partial \frac{1}{2} m_e c^i c^i}{\partial c^j} \right\rangle_e = -J_e^i \mathsf{E}^i,$$

where the electron current-density is

$$J_e^i = \mathsf{e} n_e \left(u^i + V_e^i \right). \tag{42}$$

The collisional exchange term is composed of several volumetric exchange pro-

cesses to the electron energy. The exchange with the heavy particle translational energy is found by evaluating the collision integral explicitly. If only binary encounters are considered, it can be shown that the collision integral, Equation (31), becomes [6, 27, 100]

$$-\sum_s \frac{m_e m_s}{m_e + m_s} \int g^i G^i g Q_{es}(g) f_e f_s d\mathbf{c}_e \mathbf{c}_s,$$

where the relative velocity is $g^i = c_e^i - c_s^i$, the velocity of the center of the mass of the two particles is

$$G^i = \frac{m_e c_e^i + m_s c_s^i}{m_e + m_s},$$

and Q_{es} is the collision cross section. This equation can be simplified by making the assumption that the velocity-distribution functions are displaced Maxwellians, Equation (28), about each species average velocity, u_s^i, and by recognizing that

$$\frac{m_e}{m_s} \ll 1.$$

The resulting relation for the exchange between the free-electron and heavy particle translational energies is [76, 77, 89, 100]

$$3\hat{R}\rho_e \sum_{s \neq e} \left(\hat{T}_{t,s} - \hat{T}_e\right) \frac{\nu_{es}^*}{M_s} + \rho_e \sum_{s \neq e} u_g^i \left(u_s^i - u_e^i\right) \nu_{es}^{**},$$

where the first term represents the change in electron temperature due to a temperature difference with the heavy particles, and the second term is the frictional heating due to difference in the diffusion velocity of the electrons and heavy particles. The collision frequencies are given by

$$\nu_{es}^* = \frac{m_e n_s}{3 n_e k T_e} \int Q_{es} c_e^3 f_e d\mathbf{c}_e \tag{43}$$

and

$$\nu_{es}^{**} = \frac{n_s}{n_e} \int Q_{es} c_e f_e d\mathbf{c}_e, \tag{44}$$

and

$$u_g^i = \frac{m_e u_e^i + m_s u_s^i}{m_e + m_s}.$$

The translational temperatures, $\hat{T}_{t,s}$ and $\hat{T}_e$, are unique in that, because of the assumed offset Maxwellian distribution functions, they are defined with respect to the average species velocities [100]

$$\frac{3}{2} n_s k \hat{T}_{t,s} = \frac{1}{2} \rho_s \left\langle \hat{C}^i \hat{C}^i \right\rangle_s \quad \text{and} \quad \frac{3}{2} n_e k \hat{T}_e = \frac{1}{2} \rho_e \left\langle \hat{C}^i \hat{C}^i \right\rangle_e$$

where $\hat{C}^i = c^i - u_s^i$. These temperatures are related to their mass-averaged counterparts via

$$\hat{T}_{t,s} = T_{t,s} - \frac{m_s}{3k} V_s^i V_s^i \quad \text{and} \quad \hat{T}_e = T_e - \frac{m_e}{3k} V_e^i V_e^i. \tag{45}$$

The exchange of vibrational and electron energy has been discussed for the vibrational energy equation. This same term is now subtracted from the electron energy equation:

$$- \sum_{s=mol.} \rho_s \frac{e_{v,s}^{T_e} - e_{v,s}}{\tau_s^{v-e}}.$$

Another mechanism that changes the electron energy is that from ionization reactions, which is further categorized into heavy-particle collision and electron-impact processes. During a collision event that ionizes a particle, the energy of the colliding molecules decreases by an amount at least equal to the ionization energy; the excess energy, above the ionization energy, transfers to the translational energy of the newly freed electron [100]. For an electron-impact reaction, the excess energy loss of the impacting electron is exactly equal to the gain in energy of the liberated electron and the net energy loss of the electron gas is equal to only the ionization energy. Therefore,

the terms accounting for the electron energy decrease from electron-impact ionization processes and increase from heavy-particle collision ionization processes are [84]

$$-\sum_{s=ion} \dot{n}_s^{eii} \hat{I}_s \quad \text{and} \quad \dot{w}_e^{hpci} e_{t,e}^{hpci},$$

respectively, where $\dot{n}_s^{eii}$ is the molar ionic production rate for only electron-impact processes, $\hat{I}_s$ is the ionization energy for species s, $\dot{w}_e^{hpci}$ is the mass rate of production of electrons by heavy-particle collisions, and $e_{t,e}^{hpci}$ is the average energy of a free-electron after a heavy-particle collision ionization reaction. The value for $e_{t,e}^{hpci}$ is assumed to be the average free-electron energy:

$$e_{t,e}^{hpci} = \frac{3}{2} \frac{\hat{R}}{M_s} T_e. \tag{46}$$

Electrons can also impact a molecule with enough energy to cause it to dissociate, this process decreases the electron energy by [84]

$$-\sum_{s=mol.} \dot{n}_s^{eid} \hat{D}_s,$$

where $\dot{n}_s^{eid}$ is the molar rate of dissociation of species s due only from electron-impact dissociation reactions, and $\hat{D}_s$ is the dissociation energy.

The remaining source terms for the electron energy equation are

$$-Q_{el.-e} - Q_{rad}^e,$$

where $Q_{el.-e}$ is the electron-impact electronic excitation rate, which has already been discussed for the electronic energy equation, and Q_{rad}^e is the radiative energy transport for free electron which include bound-free, free-bound, and free-free (Bremsstrahlung) transitions [84].

After combining all the above processes, the electron energy equation becomes

$$\begin{aligned}
&\frac{\partial}{\partial t}\rho_e\left(\frac{1}{2}u^iu^i+u^iV_e^i+e_{t,e}\right)+\frac{\partial}{\partial x^j}\rho_e u^j\left(\frac{1}{2}u^iu^i+e_{t,e}+\frac{p_e}{\rho_e}\right)\\
&\quad+\frac{\partial}{\partial x^j}\rho_e\left(\frac{1}{2}u^iu^iV_e^j+u^iV_e^iu^j\right)=\frac{\partial}{\partial x^i}\left(\tau_e^{ij}u^j-q_e^i\right)+J_e^i\mathsf{E}^i+\dot{w}_e^{hpci}e_{t,e}^{hpci}\\
&\quad-\sum_{s=ion}\dot{n}_s^{eii}\hat{I}_s+3\hat{R}\rho_e\sum_{s\neq e}\left(\hat{T}_{t,s}-\hat{T}_e\right)\frac{\nu_{es}^*}{M_s}+\rho_e\sum_{s\neq e}u_g^i\left(V_s^i-V_e^i\right)\nu_{es}^{**}\\
&\quad-\sum_{s=mol.}\left(\dot{n}_{e,s}^{eid}\hat{D}_s+\rho_s\frac{e_{v,s}^{T_e}-e_{v,s}}{\tau_s^{v-e}}\right)-Q_{el.-e}-Q_{rad}^e.
\end{aligned}\tag{47}$$

2.8 Thermodynamic Relations

The thermodynamic properties of each species is calculated via statistical mechanics. The partition function of a given species is [30, 104]

$$Q=Q_tQ_{int},$$

where Q_t and Q_{int} are the translational and internal partition functions, respectively. Note that a species designator, s, should be attached to each of the above terms but was omitted for simplicity. For monatomic molecules, the internal partition function is

$$Q_{int}=Q_e,$$

where Q_e is the electronic partition function. If the internal modes are assumed to be independent, the partition function of polyatomic molecules is [104]

$$Q_{int}=Q_rQ_vQ_e,$$

where Q_r and Q_v are the rotational and vibrational partition functions, respectively. In general, the vibrational and rotational modes are coupled together; both these

modes alter the internuclear distance which, in turn, changes the moment of inertia of the molecule and thus the rotational motion. Additionally, the vibrational and rotational modes depend on the electronic state of the molecule because higher electronic states change the inter-atomic forces which then alter the vibrational and rotational motion. The detailed investigation of these couplings are beyond the scope the current work and, therefore, were not pursued.

The thermal energy can be computed from the partition function via [30, 104]

$$e_s = \frac{k}{m_s} T^2 \frac{\partial}{\partial T} \ln Q^s + e_s^o, \tag{48}$$

where e_s^o is the heat of formation of species s. The specific heat at constant volume for species s is then

$$c_{v,s} = \left[\frac{\partial e_s}{\partial T} \right]_v. \tag{49}$$

Similar expressions exist for the particular translational, rotational, vibrational, and electronic energy modes: $c_{v,s}^t$, $c_{v,s}^r$, $c_{v,s}^v$, $c_{v,s}^e$. The specific heat at constant pressure for the translational mode is $c_{p,s}^t = c_{v,s}^t + k/m_s$, while for the internal modes $c_{p,s}^x = c_{v,s}^x$ where $x = r$, v, or e.

2.8.1 Translational Energy

The translational partition function is [30]

$$Q_t^s = V \left(\frac{2\pi m_s k T_t}{h^2} \right)^{3/2} \quad \left(s \neq e^-\right) \quad \text{and} \quad Q_t^e = V \left(\frac{2\pi m_e k T_e}{h^2} \right)^{3/2},$$

where V is the volume of the gas and h is the Planck constant. Using Equation (48), the translational energy is

$$e_{t,s} = \frac{3}{2} \frac{k}{m_s} T_t \quad \left(s \neq e^-\right) \quad \text{and} \quad e_{t,e} = \frac{3}{2} \frac{k}{m_e} T_e. \tag{50}$$

These results confirms the relations given in Equations (14) and (15) that were given without proof.

2.8.2 Rotational Energy

The rotational partition function of a rigid, diatomic molecule is [30]

$$Q_r^s = \frac{8\pi I_s k}{\sigma_s h^2} T_r,$$

where I_s is the moment of inertia of the molecule and σ_s is a symmetry factor. For homonuclear molecules $\sigma_s = 2$, and for heteronuclear molecules $\sigma_s = 1$. Using Equation (48), the rotational energy is

$$e_{r,s} = \frac{k}{m_s} T_r. \tag{51}$$

2.8.3 Vibrational Energy

The vibrational partition function, assuming a harmonic oscillator, is [30]

$$Q_v^s = \frac{1}{1 - \exp\left(-\Theta_v^s / T_v\right)},$$

where Θ_v^s, the characteristic vibrational temperature of species s, is

$$\Theta_v^s = \frac{h\nu_s}{k}$$

and ν_s is the harmonic-oscillator frequency of species s. Using Equation (48), the vibrational energy is

$$e_{v,s} = \frac{k}{m_s} \frac{\Theta_v^s}{\exp\left(\Theta_v^s / T_v\right) - 1}. \tag{52}$$

2.8.4 Electronic Energy

The electronic partition function of species s is [30]

$$Q_e^s = \sum_i g_i^s \exp\left(-\Theta_{e,i}^s / T_{el.}\right),$$

where g_i is the ith energy level degeneracy, the characteristic temperature for the ith level is

$$\Theta_{e,i}^s = \frac{\epsilon_i^s}{k},$$

and ϵ_i^s is the energy of the ith level. Using Equation (48), the electronic energy is

$$e_{e,s} = \frac{\hat{R}}{M_s} \frac{\sum_i g_i^s \Theta_{e,i}^s \exp\left(-\Theta_{e,i}^s / T_{el.}\right)}{\sum_j g_j^s \exp\left(-\Theta_{e,j}^s / T_{el.}\right)}. \tag{53}$$

2.8.5 Curve Fit Data

The thermodynamic properties of each species were calculated by curve fits, developed by McBride and Gordon [71, 72, 73], which accounted for vibrational-rotational mode coupling, anharmonic vibration, centrifugal distortion in the rotational mode, and the rotational and vibrational mode dependence on the electronic energy level. However, the curve fits were developed under the assumption of thermal equilibrium, $e_s = e_s(T)$, which cannot be directly used in the present multi-temperature environment. Thus, the vibrational and electronic energy of species s is

$$e_{v,s} + e_{e,s} = e_s\left(T_v\right) - c_{v,s}^{tr} T_v - e_s^o, \tag{54}$$

where the specific heat at constant volume, $c_{v,s}^{tr}$, is $\frac{3}{2}k/m_s$ for monatoms and $\frac{5}{2}k/m_s$ for diatoms.

The vibrational energy can be isolated by subtracting the electronic energy from

the previous equation

$$e_{v,s} = e_s\left(T_v\right) - C_{v,s}^{tr}\left(T_v\right) - e_{e,s}\left(T_v\right) - e_s^o, \tag{55}$$

where the electronic energy, $e_{e,s}$, is calculated via the partition function, Equation (53). The energy level degeneracies and characteristic temperatures, for the electronic partition functions, were taken from Park [84] and are repeated in Appendix A.

Figure 2 compares the electronic energy calculated via the curve fits of McBride and Gordon [71, 72, 73], represented by symbols (■ = N, ▲ = O, ▼ = N^+, ♦ = O^+), and the partition function, represented by lines, for the monatomic species in order to ensure consistency between the two methods. The largest disagreement is seen in the N^+ species at temperatures above 12,000 K; however, at those high temperatures, the electronic energy is less than 10% of the total internal energy. Disagreement is also observed at temperatures lower than 2,000 K but the contribution of the electronic energy to the total internal energy is less than 0.1% at these temperatures.

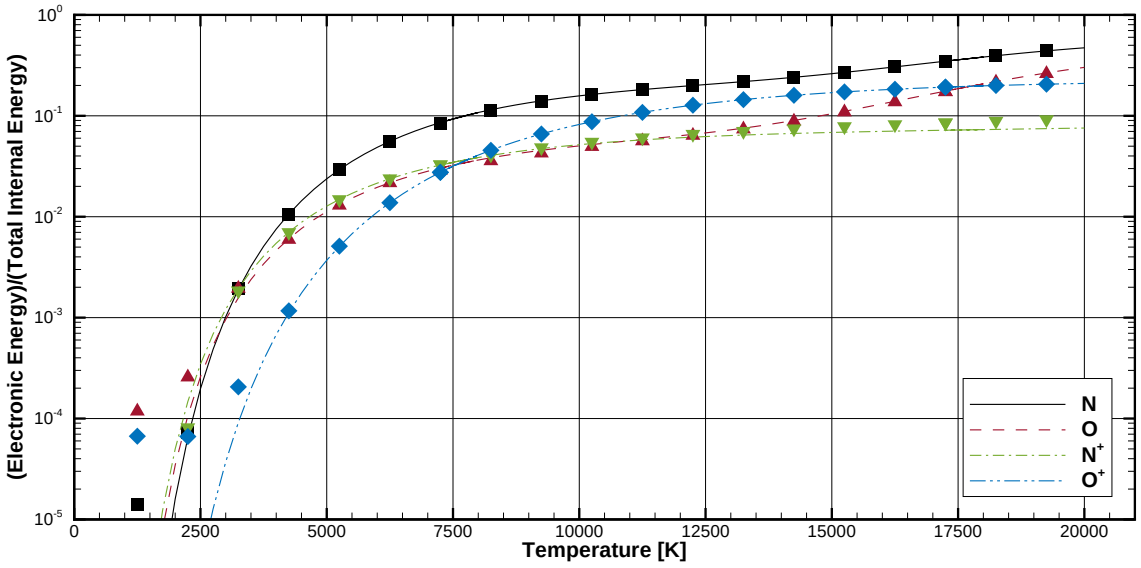

Figure 2. Electronic energy of monatomic species calculated via the partition function and curve fits (■ = N, ▲ = O, ▼ = N^+, ♦ = O^+) of McBride and Gordon [71, 72, 73].

2.9 Collision Frequency and Relaxation Times

2.9.1 Electron Collision Frequency

The collision frequency, ν_{es}^{*}, was derived by Appleton and Bray [6] for elastic collisions between electrons and other molecules. The electron-ion collision frequency is

$$\nu_{es}^{*} = \frac{8}{3}\left(\frac{\pi}{m_e}\right)^{1/2} n_s \mathbf{e}^4 \frac{1}{(2kT_e)^{1/2}} \ln\left(\frac{k^3 T_e^3}{\pi n_e \mathbf{e}^6}\right) \quad (s = ion)\,, \tag{56}$$

and electron-neutral collision frequency is

$$\nu_{es}^{*} = n_s \sigma_{es}\left(\frac{8kT_e}{\pi m_e}\right)^{1/2} \quad (s \neq ion)\,, \tag{57}$$

where σ_{es} is the cross section for the energy exchange and is given in the form of curve fits by Gnoffo, Gupta and Shinn [39]. Additionally, Sutton and Sherman [100] suggest that $\nu_{es}^{**} \approx \nu_{es}^{*}$.

2.9.2 Translational-Vibrational Relaxation Time

The relaxation time of the vibrational energy with the translational energy takes the form [39, 84]

$$\tau_s^{t-v} = \tau_s^{\mathrm{MW}} + \tau_s^{P}, \tag{58}$$

where τ_s^{MW} is the averaged Millikan and White [75] relaxation time defined empirically by [62]

$$\tau_s^{MW} = \frac{\sum\limits_{t \neq e^-} n_t}{\sum\limits_{t \neq e^-} n_t / \tau_{st}^{MW}}$$

and [75]

$$\tau_{st}^{MW} = \frac{1}{p}\exp\left[A_s\left(T_t^{-1/3} - 0.015\mu_{st}^{1/4}\right) - 18.42\right],$$

which is valid for $300\,\mathrm{K} < T_t < 8{,}000\,\mathrm{K}$. The reduced molecular weight is given by

$$\mu_{st} = \frac{M_s M_t}{M_s + M_t}.$$

Park [79] suggests that to the above expression for τ_s^{MW} should be added

$$\tau_s^P = \left(\sigma_{v,s} \langle C \rangle_s n_s\right)^{-1}$$

when temperatures exceed 8,000 K to correct for the exceedingly fast and unrealistic relaxation rates that the uncorrected Millikan and White formulation produces at high temperatures. The average speed $\langle C \rangle_s$ is given by Equation (29). The effective cross section for vibrational relaxation is taken to be [82, 85]

$$\sigma_{v,s} = \sigma'_{v,s} \left(\frac{50{,}000}{T_t}\right)^2,$$

where $\sigma'_{v,s}$ is assumed to $10^{-21}\,\mathrm{cm}^2$.

2.9.3 Vibrational-Electron Energy Relaxation Time

Although the coupling between the electron energy and vibrational energy exists for all diatomic molecules in the flowfield, it is known to be strongest for N_2. Relaxation times for other molecules is discussed by Park [84], who suggests that the available data indicates that the vibrational-electron relaxation times for O_2 and NO are orders of magnitude larger than N_2. Therefore, only the exchange process between the vibrational energy of N_2 and free-electrons is considered in this work.

Vibrational excitation of the N_2 molecule by electron-impact has been extensively studied [63, 50, 15, 17, 61, 59, 47]. The exchange mechanism, governed by the master equation, was simplified by Lee [62] into a Landau-Teller relaxation formulation

[104], where the relaxation time, τ_s^{v-e}, is the only additional parameter needing definition. Figure 3 presents several relaxation time models: Lee's original 1986 model [63] which was curve-fit by Candler and Park [25], Lee (1993) [64], Bourdon and Vervisch [15], and Mertens [74]. Additionally, a relaxation time based on the experimentally determined cross-sections of Schulz [97] is shown [80, 85]. Note that the relaxation times are plotted for lower temperatures than the respective models valid temperature ranges in order to assess their behavior at low electron temperatures as would be found directly behind a shock wave.

Lee [63, 64] developed an expression for the relaxation process assuming a harmonic oscillator and vibrational quantum numbers between 0 and 12. Additionally, the Lee (1993) model was correlated to the experimental data of Schulz at 0.1 eV and predicts the relaxation time to be quicker by a factor of five compared to the nearest model shown in the figure at that temperature. The Lee (1993) model was utilized within this work because the predicted relaxation time is the fastest, compared to the other models, over the majority of the temperature range of interest and, if additional

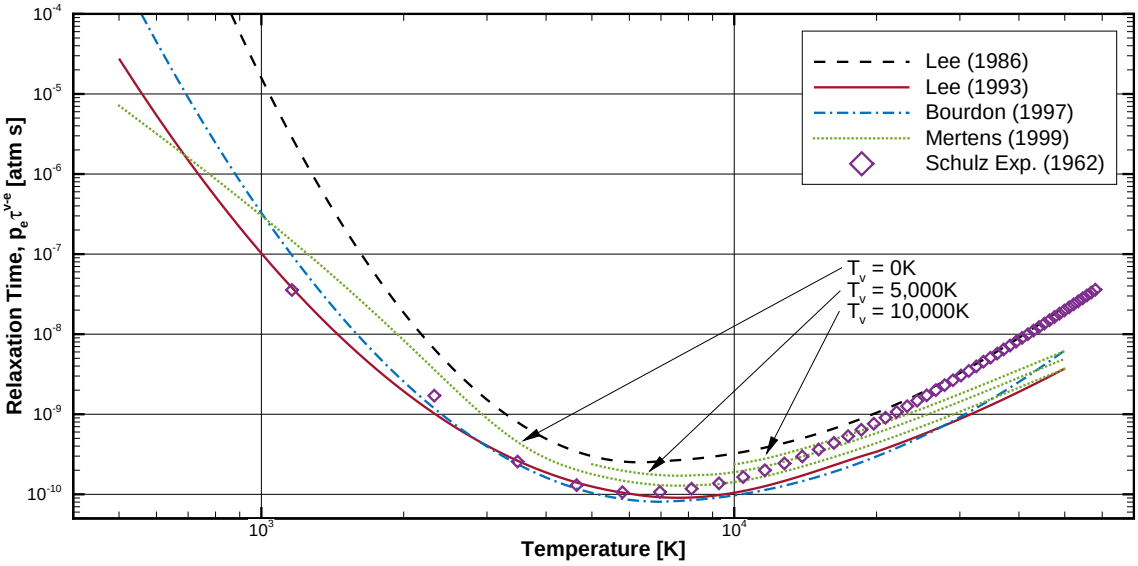

Figure 3. Vibrational-electron energy relaxation times.

physics can be captured utilizing the Lee (1993) model, than it can be assumed that the non-equilibrium of the electron temperature would be more pronounced with any other model. The Lee (1993) [64] relaxation time is:

$$1{,}000\,\mathrm{K} \leq T_e \leq 7{,}000\,\mathrm{K}: \quad \log\left(p_e \tau_{N_2}^{v-e}\right) = 3.91\left(\log T_e\right)^2 - 30.36\left(\log T_e\right) + 48.90 \tag{59}$$

$$7{,}000\,\mathrm{K} < T_e \leq 50{,}000\,\mathrm{K}: \quad \log\left(p_e \tau_{N_2}^{v-e}\right) = 1.30\left(\log T_e\right)^2 - 9.09\left(\log T_e\right) + 5.58 \tag{60}$$

The relaxation time of Mertens is additionally utilized to investigate the sensitivity of the relaxation process to which model is utilized. Mertens [74] extended the work of Lee [63] and solved the master equation for nitrogen relaxation by electron-impact assuming an anharmonic model and vibrational quantum numbers from 0 to 50 in order to improve the accuracy at high vibrational and electron temperatures. The relaxation time developed in his work is

$$2{,}300\,\mathrm{K} < T_e \leq 10{,}4000\,\mathrm{K}: \quad n_e \tau_{N_2}^{v-e} = 4.72{\times}10^{27} T_e^{-5} - 3.32{\times}10^{24} T_e^{-4} + 9.33{\times}10^{20} T_e^{-3} - 1.16{\times}10^{17} T_e^{-2} + 6.20{\times}10^{12} T_e^{-1} \tag{61}$$

$$10{,}400\,\mathrm{K} < T_e \leq 58{,}000\,\mathrm{K}: \quad n_e \tau_{N_2}^{v-e} = 8.97{\times}10^{7} - 2190 T_e + 0.328 T_e^2 - 2.06{\times}10^{-6} T_e^3 \tag{62}$$

Additionally, when $T_v < T_e$ the above equations are multiplied by

$$1 + 6.63{\times}10^{-5} T_v - 4.82{\times}10^{-10} T_v^2. \tag{63}$$

2.10 Chemical Kinetics

The chemical source terms, $\dot{w}_s$, is represented by [104]

$$\dot{w}_s = M_s \sum_r \left(\beta_{s,r} - \alpha_{s,r}\right)\left(R_{f,r} - R_{b,r}\right), \tag{64}$$

where $\alpha_{s,r}$ and $\beta_{s,r}$ are the stoichiometric coefficients for the reactants and products, respectively, for reaction r, and $R_{f,r}$ and $R_{b,r}$ are the forward and backward reaction rates. The summation in the above equation is taken over all reactions that involve species s. Table 1 presents the 22 chemical reactions that were utilized for the eleven-species air model. The forward and backward rates are

$$R_{f,r} = k_{f,r} \prod_s \left(\frac{\rho_s}{M_s}\right)^{\alpha_{s,r}}$$

and

$$R_{b,r} = k_{b,r} \prod_s \left(\frac{\rho_s}{M_s}\right)^{\beta_{s,r}},$$

where the product-sum is taken over all species in the reaction, and $k_{f,r}$ and $k_{b,r}$ are the forward and backward rate coefficients, respectively. The forward rate coefficient is given in terms of an Arrhenius equation [104]

$$k_{f,r} = C_{f,r} T^{n_{f,r}} \exp\left(-\frac{E_{f,r}}{kT}\right),$$

where the constants $C_{f,r}$, $n_{f,r}$ and $E_{f,r}$ are experimentally determined and shown in Table 1. The backward rates are determined using the equilibrium constant, $K_{e,r}$, [104]

$$k_{b,r} = \frac{k_{f,r}}{K_{e,r}}.$$

Since there exists a greater potential for the dissociation of molecules that are in

Table 1. Chemical Kinetics Model

	Reaction	C_f $\left[\frac{cm^3}{mol\,s}\right]$	η_f	E_f/k $[K]$	Ref.
1	$N + N \leftrightarrow N_2^+ + e^-$	4.4×10^7	1.50	6.750×10^4	[85]
2	$N + O \leftrightarrow NO^+ + e^-$	5.3×10^{12}	0.00	3.190×10^4	[86]
3	$N + e^- \leftrightarrow N^+ + e^- + e^-$	2.5×10^{34}	-3.82	1.682×10^5	[84]
4	$N^+ + N_2 \leftrightarrow N_2^+ + N$	1.0×10^{12}	0.50	1.220×10^4	[84]
5	$N_2 + M \leftrightarrow 2N + M$	7.0×10^{21}	-1.60	1.132×10^5	[84]
		$\times 4.3$	$(M = N, O)$		
6	$N_2 + O \leftrightarrow NO + N$	6.0×10^{13}	0.10	3.800×10^4	[35]
7	$N_2 + O^+ \leftrightarrow N_2^+ + O$	9.1×10^{11}	0.36	2.280×10^4	[84]
8	$N_2 + e^- \leftrightarrow 2N + e^-$	6.0×10^3	2.60	1.132×10^5	[16]
9	$NO + M \leftrightarrow N + O + M$	2.0×10^{15}	0.00	7.55×10^4	[51]
		$\times 22$	$(M = N, O, NO)$		
10	$O_2 + N \leftrightarrow NO + O$	2.49×10^9	1.18	4.005×10^3	[14]
11	$NO + O^+ \leftrightarrow N^+ + O_2$	1.4×10^5	1.90	2.660×10^4	[84]
12	$NO^+ + N \leftrightarrow N_2^+ + O$	7.2×10^{13}	0.00	3.550×10^4	[84]
13	$NO^+ + N \leftrightarrow O^+ + N_2$	3.4×10^{13}	-1.08	1.280×10^4	[84]
14	$NO^+ + O \leftrightarrow N^+ + O_2$	1.0×10^{12}	0.50	7.720×10^4	[84]
15	$NO^+ + O \leftrightarrow O_2^+ + N$	7.2×10^{12}	0.29	4.860×10^4	[84]
16	$NO^+ + O_2 \leftrightarrow NO + O_2^+$	2.4×10^{13}	0.41	3.260×10^4	[84]
17	$O + O \leftrightarrow O_2^+ + e^-$	7.1×10^2	2.70	8.060×10^4	[85]
18	$O + e^- \leftrightarrow O^+ + e^- + e^-$	3.9×10^{33}	-3.78	1.585×10^5	[84]
19	$O_2 + M \leftrightarrow 2O + M$	2.0×10^{21}	-1.50	5.936×10^4	[84]
		$\times 5$	$(M = N, O)$		
20	$O_2^+ + N \leftrightarrow O_2 + N^+$	8.7×10^{13}	0.14	2.860×10^4	[84]
21	$O_2^+ + N_2 \leftrightarrow N_2^+ + O_2$	9.9×10^{12}	0.00	4.070×10^4	[84]
22	$O_2^+ + O \leftrightarrow O^+ + O_2$	4.0×10^{12}	-0.09	1.800×10^4	[84]

Note: The generic collision partner, M, for dissociation reactions is taken to be every species present except free-electrons ($M \neq e^-$).

high vibrational states, Park [84] suggests using an average temperature of the form

$$T = T_t^q T_v^{1-q}$$

for dissociation reactions. It has been found that $q = 0.5$ and $q = 0.7$ agree well with experimental data [39, 83]; the present work uses $q = 0.7$. The controlling temperature for reactions involving free-electrons is T_e due to the large thermal velocity of electrons compared to the other heavier particles [39, 84]. The controlling temperature for all other reactions is T_t.

2.11 Electromagnetic Fields

An equation for the electric field is obtained by considering the electron momentum equation:

$$\frac{\partial}{\partial t}\rho_e u_e^i + \frac{\partial}{\partial x^j}\left(\rho_s u_e^i u_e^j + \mathtt{p}_e^{ij}\right) - n_e \mathtt{e} Z_e \left(\mathtt{E}^i + \epsilon^{ijk} u_e^j \mathtt{B}^k\right) = \rho_e \Delta \left\langle c^i \right\rangle_e.$$

The momentum exchange collision term, $\rho_e \Delta \left\langle c^i \right\rangle_e$, is taken as that presented by Sutton and Sherman [100] and Morse [76, 77]:

$$\rho_e \Delta \left\langle c^i \right\rangle_e = \rho_e \sum_s \left(V_s^i - V_e^i\right) \nu_{es}^*,$$

where the collision frequency ν_{es}^* is given by Equations (56) and (57). Since the mass of an electron is small, the inertial terms can be neglected. Additionally, contributions from the viscous terms (τ_e^{ij}), or off-diagonal components of the pressure tensor ($\mathtt{p}_e^{ij}$), are assumed to be negligible. Therefore, the electron momentum equation becomes [62, 84, 100]

$$\frac{\partial p_e}{\partial x^i} = n_e \mathtt{e} Z_e \left(\mathtt{E}^i + \epsilon^{ijk} u_e^j \mathtt{B}^k\right) + \rho_e \sum_s \left(V_s^i - V_e^i\right) \nu_{es}^*. \tag{65}$$

Further simplification comes after investigation of the diffusion velocity of electrons. Since the mass of an electron is much smaller than the other particles, the average thermal speed of a free-electron is much greater than the other species, thus they are highly mobile and diffuse at a faster rate compared to the heavy molecules. This causes a local charge separation and an induced electric field is established, which accelerates the positive ions and retards the electrons; the diffusion of the two particles are therefore tied together. Assuming there are no externally applied electromagnetic fields, this diffusion coupling is strong. Therefore, the electron diffusion velocity is assumed to be equal to that of the ions, which results in zero net current within the flow-field ($J^i = 0$). This very powerful condition is known as ambipolar diffusion [84, 100]. Additionally, if the vehicle body is considered to be electrically neutral, charge cannot build up anywhere and neutrality is enforced throughout the domain ($\rho_+ = 0$). Lastly, with no electric current there cannot exist a magnetic field ($\mathtt{B}^i = 0$).

As a consequence of ambipolar diffusion, the free-electron diffusion velocity is the same order of magnitude as the other particles and the last term of Equation (65), involving $V_s^i - V_e^i$, is much smaller than the other terms. Therefore, this term is neglected and the induced electric field is given by [62, 84]

$$\mathtt{E}^i = -\frac{1}{n_e \mathtt{e}} \frac{\partial p_e}{\partial x^i}, \tag{66}$$

where $Z_e = -1$ has been utilized. This simple relation states that the electric field is proportional to the gradient of the electron pressure.

2.12 Fluxes and Transport Properties

Molecular transport of mass, momentum, and energy is represented by, in the continuum approximation, species diffusion, viscous stresses, and heat flux. These relations can be derived by a Chapman-Enskog expansion of the velocity-distribution function within the Boltzmann equation [27, 48, 104]. Results for these three phenomena are presented below for the second approximation in the expansion, or the Navier-Stokes equations.

2.12.1 Diffusion Velocity

A common way to obtain the diffusion velocities in a multicomponent gas is to solve the Stefan-Maxwell equations [28, 29, 48, 101]. These equations were generalized by Ramshaw [94] and Ramshaw and Chang [92, 93] for a multi-temperature, multicomponent plasma and, in the absence of a magnetic field, are

$$\sum_r \frac{z_s z_r}{\mathscr{D}_{sr}} \left(V_r^i - V_s^i\right) = d_s^i + \gamma_s^i, \tag{67}$$

where $z_s = p_s/p$, $\mathscr{D}_{sr}$ is the binary diffusion coefficient, and the driving potential for ordinary diffusion is

$$d_s^i = \frac{\partial z_s}{\partial x^i} + (z_s - c_s)\frac{\partial \ln p}{\partial x^i} - \frac{\rho_s}{p}F_s^i + \frac{c_s}{p}\sum_r \rho_r F_r^i. \tag{68}$$

In a single temperature plasma z_s reduces to the mole fraction, X_s; thus, the first term on the right side of Equation (68) represents the contribution to diffusion from concentration gradients. The contribution to ordinary diffusion from pressure diffusion is captured in the second term, while the last two terms represent forced diffusion.

Lastly, the thermal diffusion driving potential is

$$\gamma_s^i = \frac{1}{p}\sum_r \left(\beta_{sr}\frac{\partial}{\partial x^i}\ln T_{t,r} - \beta_{rs}\frac{\partial}{\partial x^i}\ln T_{t,s}\right). \tag{69}$$

Summation of Equation (67) over all s species is zero since $\mathscr{D}_{sr} = \mathscr{D}_{rs}$ and from Equations (68) and (69)

$$\sum_s d_s^i = \sum_s \frac{\partial z_s}{\partial x^i} = 0 \quad \text{and} \quad \sum_s \gamma_s^i = 0. \tag{70}$$

After neglecting contributions from thermal diffusion and taking F_s^i from Equation (26), with $\mathsf{B}^k = 0$, Equation 67 becomes

$$\sum_r \frac{z_s z_r}{\mathscr{D}_{sr}}\left(V_r^i - V_s^i\right) = \frac{\partial z_s}{\partial x^i} + (z_s - c_s)\frac{\partial \ln p}{\partial x^i} - \frac{n_s \mathsf{e} Z_s}{p}\mathsf{E}^i \tag{71}$$

where the charge neutrality condition, $\rho_+ = 0$, has been utilized. Equation (71) is a set of $N_s - 1$ linearly independent equations and rearranging to solve for V_s^i leads to

$$V_s^i = \left(\sum_{r\neq s}\frac{z_r}{\mathscr{D}_{sr}}\right)^{-1}\left[-\frac{1}{z_s}\frac{\partial z_s}{\partial x^i} - \frac{z_s - c_s}{z_s}\frac{\partial \ln p}{\partial x^i} + \frac{n_s \mathsf{e} Z_s}{z_s p}\mathsf{E}^i + \sum_{r\neq s}\frac{z_r}{\mathscr{D}_{sr}}V_r^i\right]. \tag{72}$$

To ensure ambipolar diffusion, the electron diffusion velocity is found explicitly using the zero current condition, $J^i = 0$:

$$V_e^i = \frac{1}{n_e}\sum_{s\neq e} n_s Z_s V_s^i. \tag{73}$$

The iterative procedure presented by Sutton and Gnoffo [101] was adopted to solve these equations. The initial guess for the diffusion velocities are taken to be the first term inside the brackets of Equation (72). Then, the diffusion velocity at iteration N, $V_s^{i,N}$, is obtained via Equation (72). The $N+1$ step is obtained from

the closure equation

$$V_s^{i,N+1} = V_s^{i,N} - \sum_r c_r V_r^{i,N}, \tag{74}$$

which enforces net zero diffusive flux, Equation (11). Equation (72) to (74) are iterated until convergence is reached.

Following the work of Ramshaw and Chang [92], the $r = e$ term in the summation of Equation (67) can be neglected due to the small mass of an electron:

$$\sum_{r \neq e} \frac{z_s z_r}{\mathscr{D}_{sr}} \left(V_r^i - V_s^i \right) = d_s^i + \gamma_s^i. \tag{75}$$

Summation over all $s \neq e$ and the use of Equation (70) results in $d_e^i + \gamma_e^i = 0$. Taking F_s^i from Equation (26), with $\mathsf{B}^k = 0$, and rearranging to solve for the electric field leads to the relation

$$\mathtt{E}^i = \frac{p}{n_e \mathsf{e} Z_e} h_e^i, \tag{76}$$

where

$$h_s^i = \frac{\partial z_s}{\partial x^i} + (z_s - c_s) \frac{\partial \ln p}{\partial x^i} + \gamma_s^i \tag{77}$$

and use has been made of charge neutrality. Finally, if thermal diffusion is neglected, $\gamma_e^i = 0$, Equation (76) becomes

$$\mathtt{E}^i = -\frac{1}{n_e \mathsf{e}} \frac{\partial p_e}{\partial x^i}, \tag{78}$$

where, following the work of Ramshaw and Chang [92], c_e is neglected when compared to z_e. This relation for the electric field is exactly the same as that obtained in Section 2.11, which was independently derived using the electron momentum equation.

Approximate relations for ambipolar diffusion velocities are commonly utilized and can be obtained by considering a three component plasma containing neutral molecules (N), singly ionized molecules (I), and free-electrons (e) [92]. Within this

model, Equation (75) reduces to, for $s = I$,

$$\frac{z_I z_N}{\mathscr{D}_{NI}} \left(u_N^i - u_I^i \right) = h_I^i + h_e^i, \tag{79}$$

where use has been made of Equation (76). Equation (8) can be combined with the zero current assumption, $J^i = 0$, to eliminate u_e^i; the resulting relation is

$$\sum_{s \neq e} \left[1 + \frac{m_e Z_s}{m_s} \right] \rho_s u_s^i = \rho u^i, \tag{80}$$

where $Z_s m_e / m_s$ can be neglected due to an electron's small mass. Therefore, for the three component plasma $\rho_N u_N^i + \rho_I u_I^i \approx \rho u^i$ and, similarly, $\rho_N + \rho_I \approx \rho$. These relations can be used within Equation (79) to solve for the diffusion velocity of the ionic species:

$$V_I^i = -\frac{\rho_N \mathscr{D}_{NI}}{\rho z_I z_N} \left(h_I^i + h_e^i \right). \tag{81}$$

It is observed that when considering only ordinary diffusion, $\partial p / \partial x^i = 0$ and $\partial T_t / \partial x^i = \partial T_e / \partial x^i = 0$,

$$h_e^i = \frac{k T_e}{p} \frac{\partial n_e}{\partial x^i} = \frac{T_e}{T_t} h_I^i \tag{82}$$

since $n_e = n_I$. Therefore, Equation (81) becomes

$$V_I^i = -\frac{\rho_N \mathscr{D}_{NI}}{\rho z_I z_N} \left(1 + \frac{T_e}{T_t} \right) h_I^i, \tag{83}$$

which suggests that to account for ambipolar diffusion the ionic species diffusion velocities need only be multiplied by the factor [42, 49, 57, 92]

$$1 + \frac{T_e}{T_t}. \tag{84}$$

With this relation, the electric field would be neglected ($\mathsf{E}^i = 0$) within Equation 72.

Lastly, approximate diffusion velocities are often utilized due to their low computational costs, and in terms of mole fraction gradient is [29, 45, 101]

$$V_s^i = -\left(\sum_{r \neq s} \frac{X_r}{\mathscr{D}_{sr}}\right)^{-1} \frac{1 - c_s}{X_s} \frac{\partial X_s}{\partial x^i}. \tag{85}$$

This equation was derived by Curtiss and Hirschfelder [29] using the Stefan-Maxwell equations for the case of species s being present as a trace amount. Additionally, its derivation can be reasoned by considering an effective diffusion coefficient within the framework of Fick's Law where the other species diffusion velocities are considered to be equal [101]. In this model, ambipolar effects can be considered by multiplying the diffusion coefficients for ionic species by a factor of two, which is justified by considering $T_e \approx T_t$ in Equation (84) [39, 62, 84, 100]. The electron diffusion velocity is then found via Equation (73). As a final step, the approximate diffusion velocities are corrected with Equation (74) to ensure consistency [101].

2.12.2 Stress Tensor

The viscous stress tensor, τ^{ij}, for a Newtonian fluid, is [60, 104]

$$\tau^{ij} = \mu\left(\frac{\partial u^i}{\partial x^j} + \frac{\partial u^j}{\partial u^i}\right) + \beta \frac{\partial u^k}{\partial x^k}\delta^{ij},$$

where μ is the mixture viscosity and β is the mixture second coefficient of viscosity. Using Stoke's hypothesis results in [60, 104]

$$\beta = -\frac{2}{3}\mu.$$

Therefore, the viscous stress tensor is

$$\tau^{ij} = \mu \left(\frac{\partial u^i}{\partial x^j} + \frac{\partial u^j}{\partial x^i} \right) - \frac{2}{3} \mu \frac{\partial u^k}{\partial x^k} \delta^{ij}. \tag{86}$$

2.12.3 Energy Flux

The heat flux vectors are composed of two processes: conduction of energy driven by temperature gradients and diffusion of energetic molecules [48, 62]. For the internal energy modes, the heat flux vectors are

$$q_x^i = \sum_s \rho_s e_{x,s} V_s^i - \eta_x \frac{\partial T_x}{\partial x^i}, \tag{87}$$

where $x = r$, v, or $el.$ for the rotational, vibrational, or electronic vectors, respectively, and η_x is the thermal conductivity for the x energy mode. The free-electron heat flux vector is [62]

$$q_e^i = \rho_e h_{t,e} V_e^i - f_e \eta_e \frac{\partial T_e}{\partial x^i}, \tag{88}$$

where $h_{t,e}$ is the enthalpy of the free electrons and η_e is the electron thermal conductivity. The factor f_e is the ratio of the collision frequency of electrons with other electrons to collisions with all species to account for only heat transfer from electron-electron collisions [62, 84]. The total heat flux vector is [62]

$$q^i = \sum_s \rho_s h_s V_s^i - \eta_t \frac{\partial T_t}{\partial x^i} - \eta_r \frac{\partial T_r}{\partial x^i} - \eta_v \frac{\partial T_v}{\partial x^i} - \eta_{el.} \frac{\partial T_{el.}}{\partial x^i} - \eta_e \frac{\partial T_e}{\partial x^i}, \tag{89}$$

where h_s is the enthalpy for species s, and η_t is the thermal conductivity for translational energy.

2.12.4 Transport Properties

The following transport property coefficients were developed by Yos [114] and subsequently adapted for multi-temperature mixtures by Lee [62]. Similar derivations are presented by Gnoffo, Gupta, and Shinn [39] and Gupta *et al.* [46]. The binary diffusion, mixture viscosity, and thermal conductivity coefficients require the calculation of the collision integral, $\bar{\Omega}_{st}^{(k,k)}$, which are weighted averages of the of the collision cross sections and have been compiled by Wright *et al.* [109, 111]. Two additional modified collision integrals are of use to define:

$$\Delta_{sr}^{(1)}(T) = \frac{8}{3}\left[\frac{2m_s m_r}{\pi kT\left(m_s + m_r\right)}\right]^{1/2} \pi \bar{\Omega}_{sr}^{(1,1)}$$

and

$$\Delta_{sr}^{(2)}(T) = \frac{16}{5}\left[\frac{2m_s m_r}{\pi kT\left(m_s + m_r\right)}\right]^{1/2} \pi \bar{\Omega}_{sr}^{(2,2)}.$$

The binary diffusion coefficients are

$$\mathscr{D}_{sr} = \frac{kT_t}{p\Delta_{sr}^{(1)}(T_t)}\ (s,\ r \neq e) \quad \text{and} \quad \mathscr{D}_{sr} = \frac{kT_e}{p\Delta_{sr}^{(1)}(T_e)}\ (s \text{ or } r = e), \tag{90}$$

and the mixture coefficient of viscosity is, using Wilke's mixing rule [105],

$$\mu = \sum_{s \neq e} \frac{m_s X_s}{\sum\limits_{r \neq e} X_r \Delta_{sr}^{(2)}(T_t) + X_e \Delta_{se}^{(2)}(T_e)} + \frac{m_e X_e}{\sum\limits_{r} X_r \Delta_{er}^{(2)}(T_e)}. \tag{91}$$

The translational thermal conductivity is

$$\eta_t = \frac{15}{4} k \sum_{s \neq e} \frac{X_s}{\sum\limits_{r \neq e} a_{sr} X_r \Delta_{sr}^{(2)}(T_t) + a_{se} X_e \Delta_{se}^{(2)}(T_e)}, \tag{92}$$

where

$$a_{sr} = 1 + \frac{\left(1 - \frac{m_s}{m_r}\right)\left(0.45 - 2.45\frac{m_s}{m_r}\right)}{\left(1 + \frac{m_s}{m_r}\right)^2}.$$

The rotational thermal conductivity is

$$\eta_r = k \sum_{s=mol.} \frac{X_s}{\sum\limits_{r \neq e} X_r \Delta_{sr}^{(1)}\left(T_t\right) + X_e \Delta_{se}^{(1)}\left(T_e\right)}, \tag{93}$$

the vibrational conductivity is

$$\eta_v = \sum_{s=mol.} \frac{m_s c_{p,s}^v X_s}{\sum\limits_{r \neq e} X_r \Delta_{sr}^{(1)}\left(T_t\right) + X_e \Delta_{se}^{(1)}\left(T_e\right)}, \tag{94}$$

and the electronic conductivity is

$$\eta_{el.} = \sum_{s \neq e} \frac{m_s c_{p,s}^e X_s}{\sum\limits_{r \neq e} X_r \Delta_{sr}^{(1)}\left(T_r\right) + X_e \Delta_{se}^{(1)}\left(T_e\right)}. \tag{95}$$

Lastly, the electron conductivity is

$$\eta_e = \frac{15}{4} k \frac{X_e}{\sum\limits_{r} a_{er} X_r \Delta_{er}^{(2)}\left(T_e\right)}. \tag{96}$$

The factor f_e, from Equation (88), is given by Park [84]

$$f_e = \frac{X_e}{\Delta_{ee}^{(2)}\left(T_e\right)} \left[\sum_r \frac{X_r}{a_{er} \Delta_{er}^{(2)}}\right]^{-1}. \tag{97}$$

2.13 Simplifications to the Electron Energy Equation

The electron energy equation, Equation (47), is complex with many terms not contributing significantly. First, the kinetic terms contribute very little to the overall energy balance due to the small mass of an electron. This argument is illustrated by considering the electron velocity, u_e^i, to be 10,000 $\mathrm{m\,s^{-1}}$ and the electron temperature, T_e, to be 100 K; with these conditions the kinetic energy ($\frac{1}{2}u_e^i u_e^i$) is still less than 2.5% of the thermal energy, $e_{t,e}$. Considering that throughout the domain the ambipolar diffusion velocity of electrons is much less than the freestream fluid velocity, the kinetic terms involving V_e^i are neglected. Similarly, the diffusion term in the electron current, J_e^i, is also neglected on the grounds that generally $V_e^i \ll u^i$. Additionally, following the reasoning in Section 2.11 in deriving the electric field, the frictional heating term due to the difference in electron and heavy particle velocities is also neglected. Lastly, the electron viscous stress tensor, τ_e^{ij}, is assumed to be small and is neglected [62, 84, 100]. Therefore, the electron energy equation, Equation (47), reduces to

$$\begin{aligned}\frac{\partial}{\partial t}\rho_e E_e + \frac{\partial}{\partial x^i}u^i\rho_e H_e = &-\frac{\partial}{\partial x^i}q_e^i + u^i\frac{\partial p_e}{\partial x^i} + \dot{w}_e^{hpci}e_{t,e}^{hpci} - \sum_{s=ion}\dot{n}_s^{eii}\hat{I}_s \\ &+ 3\hat{R}\rho_e\left(T_t - T_e\right)\sum_{s\neq e^-}\frac{\nu_{es}^*}{M_s} - \sum_{s=mol.}\left(\dot{n}_s^{ied}\hat{D}_s + \rho_s\frac{e_{v,s}^{T_e} - e_{v,s}}{\tau_{es}}\right) \\ &- Q_{el.-e} - Q_{rad}^e\end{aligned} \tag{98}$$

where

$$E_e = e_{t,e} + \frac{1}{2}u^i u^i \quad \text{and} \quad H_e = E_e + \frac{p_e}{\rho_e}. \tag{99}$$

Further simplification can be done by neglecting, based on the previous example, the remaining inertial terms, $\frac{1}{2}u^i u^i$. The terms on the left side of Equation (98) then

become

$$\frac{\partial}{\partial t}\rho_e e_{t,e} + \frac{\partial}{\partial x^i}\left(\rho_e e_{t,e} + p_e\right) u^i. \tag{100}$$

2.14 Final Form of the Governing Equations

The governing equations, presented in the previous sections, are recast in the form

$$\frac{\partial}{\partial t}\mathbf{W} + \frac{\partial}{\partial x^j}\left(\mathbf{F}_\mathbf{c}^j - \mathbf{F}_\mathbf{v}^j\right) = \mathbf{Q}, \tag{101}$$

where $\mathbf{W}$ is the vector of conserved variables, $\mathbf{F_c}^j$ and $\mathbf{F_v}^j$ are the vector of convective and viscous fluxes, respectively, and $\mathbf{Q}$ is the vector of source terms. Equation (101) can be transformed into integral form, suitable for implementation into a finite volume computational scheme, by integrating over a control volume, Ω, and using Guass's divergence theorem:

$$\int_\Omega \frac{\partial}{\partial t}\mathbf{W} dV + \oint_{\partial\Omega}\left(\mathbf{F}_\mathbf{c}^j - \mathbf{F}_\mathbf{v}^j\right)\hat{n}^j dS = \int_\Omega \mathbf{Q} dV. \tag{102}$$

2.14.1 Two-Temperature Model

The two-temperature model combines the conservation equations for vibrational, electronic, and free-electron energies by summation of Equations (39), (41), and (98). The resulting vector of conserved variables is

$$\mathbf{W} = \left\{\rho_s \quad \rho u^i \quad \rho E \quad \rho E_{vee}\right\}^T, \tag{103}$$

the convective and viscous flux vectors are, respectively,

$$\mathbf{F}_{\mathbf{c}}^{j} = \begin{Bmatrix} \rho_s u^j \\ \rho u^i u^j + p\delta^{ij} \\ \rho H u^j \\ \left[\rho E_{vee} + p_e\right] u^j \end{Bmatrix} \quad \text{and} \quad \mathbf{F}_{\mathbf{v}}^{j} = \begin{Bmatrix} -\rho_s V_s^j \\ \tau^{ij} \\ u^i \tau^{ij} - q^j \\ -q_{vee}^j \end{Bmatrix}, \tag{104}$$

and the source vector is

$$\mathbf{Q} = \{w_s \quad 0 \quad -Q_{rad} \quad Q_{vee}\}^T, \tag{105}$$

where $E_{vee} = e_v + e_e + c_e E_e$, $q_{vee}^i = q_v^i + q_{el.}^i + q_e^i$, and

$$\begin{aligned} Q_{vee} = & \sum_{s=mol.} \left(\rho_s \frac{e_{v,s}^{T_t} - e_{v,s}}{\tau_s^{t-v}} + \dot{w}_s \hat{e}_{v,s} - \dot{n}_s^{eid} \hat{D}_s \right) + \sum_s \dot{w}_s \hat{e}_{e,s} + u^i \frac{\partial p_e}{\partial x^i} \\ & + 3\rho_e \hat{R} \left(T_t - T_e\right) \sum_{s \neq e^-} \frac{\nu_{es}^*}{M_s} - \sum_{s=ion} \dot{n}_s^{eii} \hat{I}_s + \dot{w}_e^{hpci} e_{t,e}^{hpci} - Q_{rad}^v - Q_{rad}^{el.} - Q_{rad}^e. \end{aligned} \tag{106}$$

2.14.2 Free-Electron Three-Temperature Model

The free-electron three-temperature model groups the vibrational and electronic energies together, by addition of Equations (39) and (41), and retains a separate equation for the free-electron energy, Equation (98). Inherent in this model is the assumption that the vibrational-electronic exchange process is the dominant electronic energy source term. This assumption holds true for very weakly ionized plasmas, where the electron-impact electronic-excitation process, $Q_{el.-e}$, is small due to the insufficient number of free-electrons available to activate this mechanism. Therefore, the electron-impact electronic excitation process is neglected within this model. The

resulting vector of conserved variables is

$$\mathbf{W} = \left\{ \rho_s \quad \rho u^i \quad \rho E \quad \rho e_{ve} \quad \rho_e E_e \right\}^T, \tag{107}$$

the convective and viscous flux vectors are, respectively,

$$\mathbf{F}_\mathbf{c}^j = \left\{ \begin{array}{c} \rho_s u^j \\ \rho u^i u^j + p\delta^{ij} \\ \rho H u^j \\ \rho e_{ve} \\ \rho_e H_e u^j \end{array} \right\} \quad \text{and} \quad \mathbf{F}_\mathbf{v}^j = \left\{ \begin{array}{c} -\rho_s V_s^j \\ \tau^{ij} \\ u^i \tau^{ij} - q^j \\ -q_{ve}^j \\ -q_e^j \end{array} \right\}, \tag{108}$$

and the source vector is

$$\mathbf{Q} = \{ w_s \quad 0 \quad -Q_{rad} \quad Q_{ve} \quad Q_e \}^T, \tag{109}$$

where $e_{ve} = e_v + e_e$, $q_{ve}^i = q_v^i + q_{el.}^i$,

$$\begin{aligned} Q_{ve} = \sum_{s=mol.} \left(\rho_s \frac{e_{v,s}^{T_t} - e_{v,s}}{\tau_s^{t-v}} + \rho_s \frac{e_{v,s}^{T_e} - e_{v,s}}{\tau_s^{v-e}} + \dot{w}_s \hat{e}_{v,s} \right) \\ + \sum_s \dot{w}_s \hat{e}_{e,s} - Q_{rad}^v - Q_{rad}^{el.}, \end{aligned} \tag{110}$$

and

$$\begin{aligned} Q_e = - \sum_{s=mol.} \left(\rho_s \frac{e_{v,s}^{T_e} - e_{v,s}}{\tau_s^{v-e}} + \dot{n}_s^{eid} \hat{D}_s \right) + u^i \frac{\partial p_e}{\partial x^i} + 3\rho_e \hat{R} \left(T_t - T_e \right) \sum_{s \neq e^-} \frac{\nu_{es}^*}{M_s} \\ - \sum_{s=ion} \dot{n}_s^{eii} \hat{I}_s + \dot{w}_e^{hpci} e_{t,e}^{hpci} + \sum_s \dot{w}_s e_{e,s} - Q_{rad}^e. \end{aligned} \tag{111}$$

2.14.3 Electron-Electronic Three-Temperature Model

The electron-electronic three-temperature model retains a separate equation for the vibrational energy, Equation (39), but combines the equations for electronic and free-electron energies, Equations (41) and (98). As ionization levels increase, the electron-impact electronic-excitation process begins to dominate the electronic energy equation and the vibrational-electronic exchange mechanism becomes less significant. The resulting vector of conserved variables is

$$\mathbf{W} = \left\{ \rho_s \quad \rho u^i \quad \rho E \quad \rho e_v \quad \rho_e E_{ee} \right\}^T, \tag{112}$$

the inviscid and viscous flux vectors are, respectively,

$$\mathbf{F}_\mathbf{c}^j = \begin{Bmatrix} \rho_s u^j \\ \rho u^i u^j + p\delta^{ij} \\ \rho H u^j \\ \rho e_v \\ \left[\rho_e E_{ee} + p_e\right] u^j \end{Bmatrix} \quad \text{and} \quad \mathbf{F}_\mathbf{v}^j = \begin{Bmatrix} -\rho_s V_s^j \\ \tau^{ij} \\ u^i \tau^{ij} - q^j \\ -q_v^j \\ -q_{ee}^j \end{Bmatrix}, \tag{113}$$

and the source vector is

$$\mathbf{Q} = \left\{ w_s \quad 0 \quad -Q_{rad} \quad Q_e \quad Q_{ee} \right\}^T, \tag{114}$$

where $E_{ee} = e_e + c_e E_e$, $q_{ee}^i = q_{el.}^i + q_e^i$,

$$Q_v = \sum_{s=mol.} \left(\rho_s \frac{e_{v,s}^{T_t} - e_{v,s}}{\tau_s^{t-v}} + \rho_s \frac{e_{v,s}^{T_e} - e_{v,s}}{\tau_s^{v-e}} + \dot{w}_s \hat{e}_{v,s} \right) - Q_{rad}^v, \tag{115}$$

and

$$Q_{ee} = -\sum_{s=mol.}\left(\rho_s \frac{e_{v,s}^{T_e} - e_{v,s}}{\tau_s^{v-e}} + \dot{n}_s^{eid}\hat{D}_s\right) + u^i\frac{\partial p_e}{\partial x^i} + 3\rho_e\hat{R}\left(T_t - T_e\right)\sum_{s\neq e^-}\frac{\nu_{es}^*}{M_s} - \sum_{s=ion}\dot{n}_s^{eii}\hat{I}_s + \dot{w}_e^{hpci}e_{t,e}^{hpci} + \sum_s \dot{w}_s\hat{e}_{e,s} - Q_{rad}^{el.} - Q_{rad}^{e}. \tag{116}$$

2.15 Numerical Method

A node-centered, finite volume CFD method was used to numerically solve the governing equations [5, 11, 13, 68, 90, 103]. Discretization of Equation (102) results in the following linear system

$$[\mathbf{A}]^n \Delta^n \{\mathbf{W}\} = -\{\mathbf{R}\}^n, \tag{117}$$

where $\{\mathbf{W}\}$ and $\{\mathbf{R}\}$ are the vector of conserved variables and the residual, respectively, for all nodes in the domain. These vectors each have the length of

$$(number\ of\ conserved\ variables)\cdot(number\ of\ nodes).$$

The residual for a specific node, I, is the sum of the fluxes along each intersecting edge and the contribution from volume sources:

$$\mathbf{R}_I = \sum_{m=1}^{N_E}\left(\mathbf{F}_{\mathbf{c}}^j - \mathbf{F}_{\mathbf{v}}^j\right)_m n_m^j \Delta S_m - \Omega_I \mathbf{Q}_I. \tag{118}$$

The temporal operator, Δ^n, is

$$\Delta^n \{\mathbf{W}\} = \{\mathbf{W}\}^{n+1} - \{\mathbf{W}\}^n, \tag{119}$$

where n is the current iteration level, and the implicit matrix operator, $[\mathbf{A}]$, is

$$[\mathbf{A}]^n = \frac{\Omega_I}{\Delta^n t}[\mathbf{I}] + \frac{\partial \{\mathbf{R}\}^n}{\partial \{\mathbf{W}\}^n}. \tag{120}$$

A steady solution is sought iteratively for $\Delta^n \{\mathbf{W}\}$ until $\{\mathbf{R}\}^n$ is converged to zero. A point-implicit method is utilized where $\Delta^n \{\mathbf{W}\}$ is found by completing subiterations to obtain a solution update for each node, $\Delta^n \{\mathbf{W}_I\}^i$, which converge to $\Delta^n \{\mathbf{W}\}$. Equation (117) is recast into the following form

$$\left[\frac{\Omega_I}{\Delta t^n}[\mathbf{I}] + \frac{\partial \{\mathbf{R}_I\}^n}{\partial \{\mathbf{W}_I\}^n}\right] \Delta^n \{\mathbf{W}_I\}^i = -\{\mathbf{R}_I\}^n - \sum_{J \neq I} \frac{\partial \{\mathbf{R}_I\}^n}{\partial \{\mathbf{W}_J\}} \Delta^n \{\mathbf{W}_J\}^\star \tag{121}$$

where $\Delta^n \{\mathbf{W}_I\}^i$ is now obtained directly through matrix inversion of the terms in the bracket on the left side, where $\Delta^n \{\mathbf{W}_J\}^\star$ represents the most current solution update through the iterative procedure [5].

The convective fluxes, $\mathbf{F}^j_{\mathbf{c}}$, were computed obtained using a Roe approximate Riemann solver [96, 103] and second order accuracy was obtained with Yee's [113] Symmetric Total Variation Diminishing (STVD) scheme. The solution was reduced to first order accuracy near shock waves with the use of the minmod limiter [113]. Flow-field gradients were calculated using a Green-Guass formulation [13] and the viscous flux, $\mathbf{F}^j_{\mathbf{v}}$, is calculated by adding the contributions from each cell adjacent to the edge [5].

III. Zero-Dimensional Simulation

The equations governing the thermochemical non-equilibrium processes present in hypersonic flows are dominated by the volumetric source terms. Therefore, the models developed in Chapter II were investigated within the context of zero-dimensional simulations. The equations that were numerically solved were thus

$$\frac{\partial}{\partial t}\mathbf{W} = \mathbf{Q}, \tag{122}$$

where $\mathbf{W}$ and $\mathbf{Q}$ are given in Section 2.14. In completing this investigation, the non-equilibrium processes predicted by the free-electron and electron-electronic three-temperature models were characterized in regions of heating (compression) and cooling (expansion). Additionally, the sensitivity of the thermochemical non-equilibrium processes to the vibrational-electron relaxation time, $\tau_{N_2}^{v-e}$, was investigated by completing simulations with the both the Lee [64] and Mertens [74] models, which were presented in Section 2.9.3. Lastly, the suitability of an approximate Landau-Teller formulation for translational-vibrational relaxation was investigated.

A fourth-order Runge-Kutta time integration scheme [7] was used to numerically integrate Equation (122) given a set of initial conditions until equilibrium was reached. The base physics modules from FUN3D were modified to include the three-temperature models and then incorporated inside a newly developed architecture to run these simulations. Table 2 presents the details of the initial conditions for each case that was considered. Three compression cases were considered where the initial conditions for the density and translational-rotational temperatures were that of the jump conditions of normal shock waves at Mach 20, 30, and 40 at 61 kilometers altitude. This altitude was chosen to be consistent with the RAM C-II simulations presented in Chapter IV. Additionally, an expansion case was considered where the

Table 2. Zero-Dimensional Study Initial Conditions

	Case	Density [kg m^{-3}]	T_{tr} [K]	T_v and T_e [K]
1	Compression (Mach = 20)	1.505×10^{-3}	19129	243
2	Compression (Mach = 30)	1.516×10^{-3}	42754	243
3	Compression (Mach = 40)	1.519×10^{-3}	75829	243
4	Expansion	3.901×10^{-5}	1350	7112

Table 3. Expansion Simulation Initial Species Concentrations

Species	Concentration, X_s	Species	Concentration, X_s
N_2	4.97×10^{-1}	N_2^+	3.29×10^{-9}
O_2	1.42×10^{-3}	O_2^+	5.00×10^{-8}
N	1.99×10^{-1}	N^+	4.06×10^{-6}
O	3.03×10^{-1}	O^+	2.60×10^{-5}
NO	3.71×10^{-4}	NO^+	1.41×10^{-5}
		e^-	4.42×10^{-5}

initial conditions were taken from a point in the expansion region of the RAM C-II simulation using the two-temperature model; Table 3 presents the initial concentrations of each species for the this case.

The electron energy source terms are detailed in many figures throughout this study and Table 4 presents the key to interpreting the legend for these figures. The energy decrease from electron-impact dissociation reactions, $\sum_{s=mol.} \dot{n}_s^{eid} \hat{D}_s$, was considered but never obtained a magnitude that was comparable to other terms for each case. Therefore, this term is not reported in the results presented below.

Table 4. Legend Key for the Electron Energy Source Terms

Process	Label	Term
Translational-Electron	t − e	$3\rho_e \hat{R}\left(T_t - T_e\right) \sum_{s \neq e^-} \frac{\nu^*_{es}}{M_s}$
Vibrational-Electron	v − e	$-\rho_{N_2} \frac{e^{T_e}_{v,N_2} - e_{v,N_2}}{\tau^{v-e}_{N_2}}$
Electron Impact Ionization	eii	$-\sum_{s=ion} \dot{n}^{eii}_s \hat{I}_s$
Heavy-Particle Collision Ionization	hpci	$\dot{w}^{hpci}_e e^{hpci}_{t,e}$

3.1 Case 1: Compression – Mach 20 Shock

3.1.1 Free-Electron Model

The results for Case 1, the simulated Mach 20 normal shock, using the free-electron three-temperature model and the relaxation time of Lee [64] are presented in Figure 4. The temperatures and charged species time histories are shown, as well as results obtained using the two-temperature model; neutral species are not presented because there was no discernible difference between the two-temperature and three-temperature results. The electron temperature, Figure 4(a), exhibited an incubation period where it lagged behind the vibrational temperature due to the low number of electrons early in the simulation. This lag was aided by the slow relaxation time for the vibrational-electron coupling at low electron temperatures, as shown in Figure 3. As the electron temperature and number of electrons increased, the vibrational-electron coupling strengthened and equilibration between the two modes occurred very quickly. The translational-rotational temperatures, T_{tr}, between the two models were indistinguishable from each other, as was the vibrational-electronic-electron temperature, T_{vee}, and the vibrational-electronic temperature, T_{ve}.

The charged species concentrations, as shown in Figure 4(b), were in good agree-

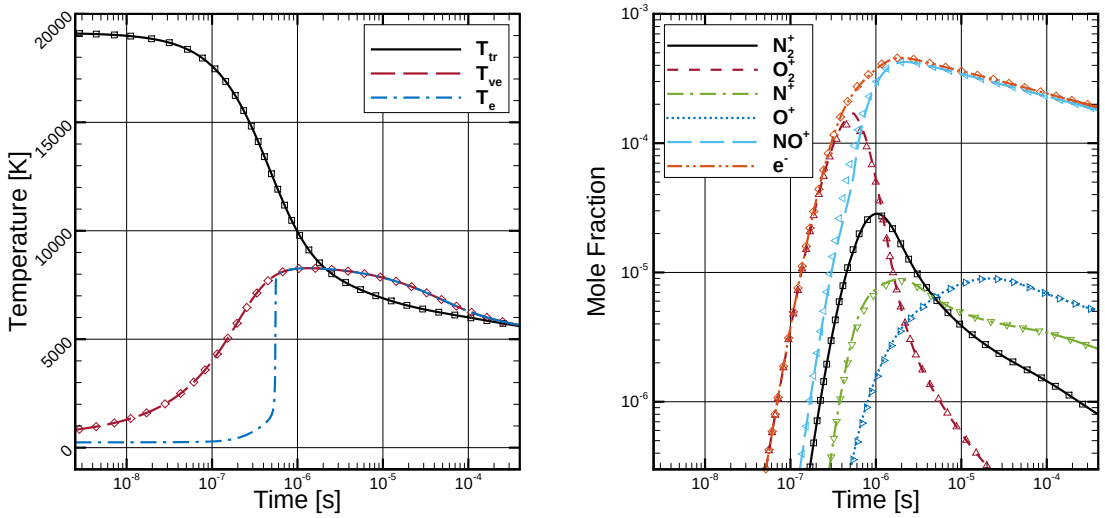

(a) Temperatures. ■ $= T_{tr}$ ♦ $= T_{vee}$

(b) Charged species. ■ $= N_2^+$ ▲ $= O_2^+$ ▼ $= N^+$ ►$= O^+$ ◄$= NO^+$ ♦ $= e^-$

Figure 4. Zero-dimensional Case 1, Mach 20 shock, comparison between the two-temperature and free-electron three-temperature models. Lee's [64] relaxation time was utilized for the vibrational-electron energy exchange. Symbols are results from the two-temperature model.

ment between the two-temperature and three-temperature models. Initially, the free-electrons were produced mainly from the associative ionization reaction

$$O + O \;\leftrightarrow\; O_2^+ + e^-.$$

The three-temperature model predicted a larger peak concentration of O_2^+ because the backward rate of the above reaction, the electron-associative dissociation reaction, is controlled by T_e and the low electron temperature dictated a low reaction rate and thus more O_2^+. As the simulation continued, the dominant ionic species switched from O_2^+ to NO^+. The concentration of NO^+ is largely controlled by the associative ionization reaction

$$N + O \;\leftrightarrow\; NO^+ + e^-,$$

and as the forward reaction, controlled by T_{tr}, progressed, the three-temperature

model predicted a slight stall in the concentration of NO^+. The backward rate of the above reaction, controlled by T_e, decreases with increasing temperature. Thus, due to the low temperature early in the simulation this rate was relatively high and the resulting concentration of NO^+ was lower for the three-temperature model.

Simulations using the vibrational-electron relaxation times of Lee [64] and Mertens [74] are compared in Figure 5. Lee's model predicted the electron energy equilibrated with the vibrational energy sooner than Mertens', which was as expected after examining the behavior of the relaxation times at low temperatures. As shown in Figure 3, the relaxation time of Lee is approximately five times lower than that of Mertens over the electron temperature range from 1,000 K to 3,000 K. The stall in the concentration of NO^+ was more pronounced with Mertens' model due to the electron temperature remaining at lower values for a longer period of time.

Figure 5(b) presents the source terms to the free-electron energy. The vibration-electron energy exchange process was the dominant mechanism for free-electron equilibration. The only other terms that significantly contributed to the electron energy balance were the translational-electron exchange and heavy-particle collision ionization terms; however, both were small in comparison to the vibrational-electron exchange term.

3.1.2 Electron-Electronic Model

The simulation of Case 1 using the electron-electronic three-temperature model, compared to results using the two-temperature model, is presented in Figure 6. The relaxation process for the electron-electronic model was an order of magnitude slower than that of the free-electron model, which was attributed to the larger energy manifold of the electron-electronic model with which the free-electrons transfer energy. This slower electron energy equilibration did not affect the translational-rotational

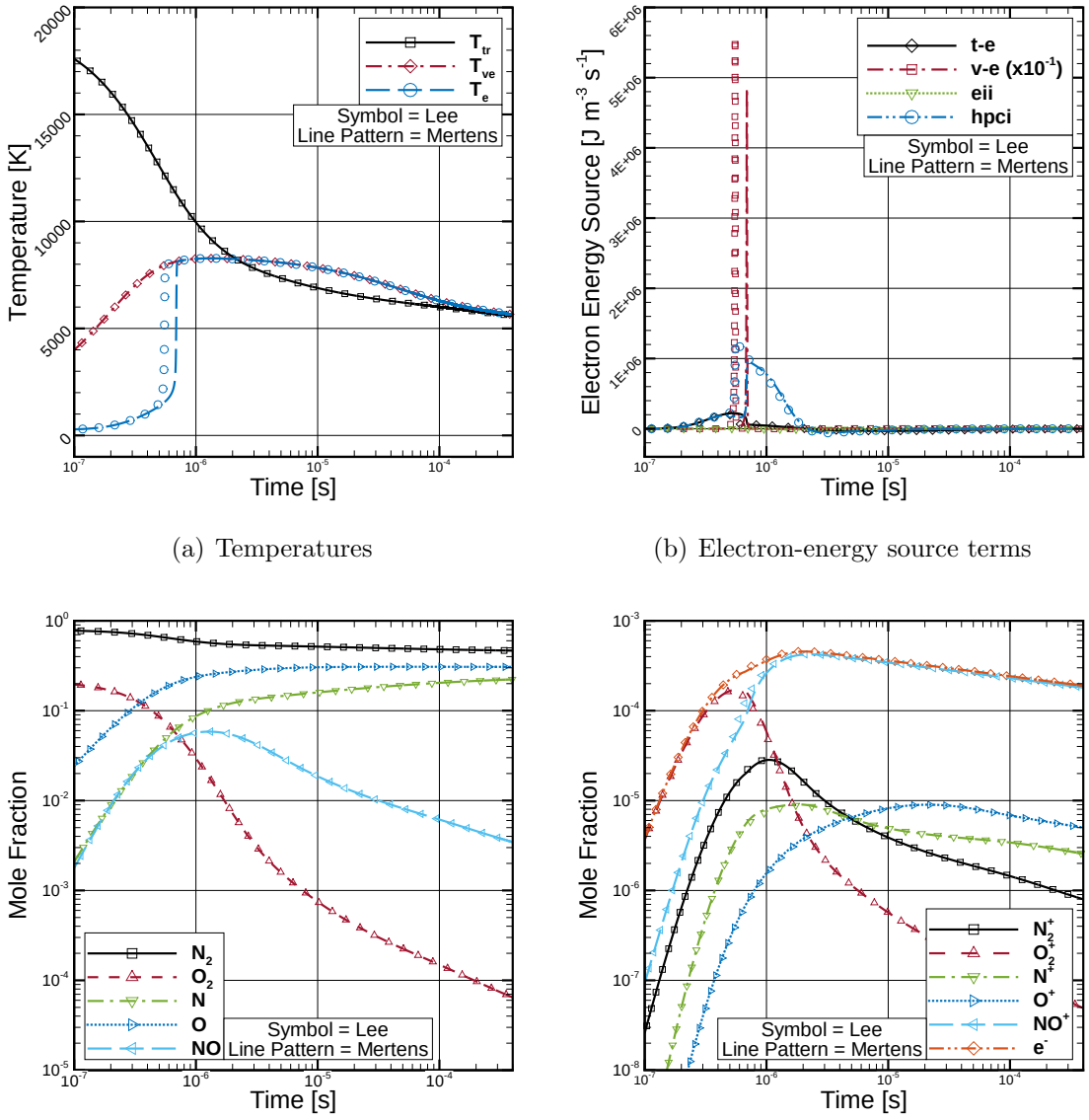

(a) Temperatures

(b) Electron-energy source terms

(c) Neutral species

(d) Charged species

Figure 5. Zero-dimensional Case 1, Mach 20 shock, comparison between the vibrational-electron energy relaxation times of Lee [64] and Mertens [74] for the free-electron three-temperature model.

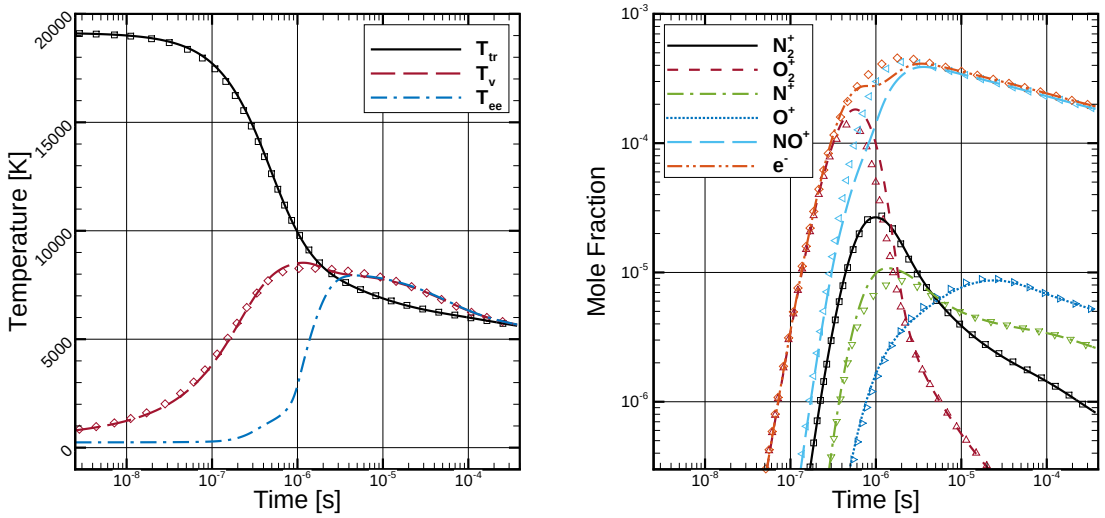

(a) Temperatures. ■ $= T_{tr}$ ♦ $= T_{vee}$

(b) Charged species. ■ $= N_2^+$ ▲ $= O_2^+$ ▼ $= N^+$ ►$= O^+$ ◄$= NO^+$ ♦ $= e^-$

Figure 6. Zero-dimensional Case 1, Mach 20 shock, comparison between the two-temperature and electron-electronic three-temperature models. Lee's [64] relaxation time was utilized for the vibrational-electron energy exchange. Symbols are results from the two-temperature model.

and vibrational temperatures, which matched closely between the two models. The increased peak O_2^+ concentration and the stall in the NO^+ production of the three-temperature model was much more evident in the electron-electronic model than the free-electron model, which was due to the longer electron-temperature incubation period. Additionally, the NO^+ stall translated to a decreased peak prediction of the electron concentration as compared to the two-temperature model.

Simulations using the relaxation times of Lee [64] and Mertens [74] are compared in Figure 7. Similar to the result using the free-electron model, the relaxation time of Lee predicted the electron-electronic energy equilibrated with the vibrational energy sooner than that of Mertens'. Additionally, the stall in the NO^+ production was more pronounced when using Mertens' model.

The source terms to the electron-electronic manifold, Figure 7(b), were dominated by the vibrational-electron exchange process. The translational-electron exchange and

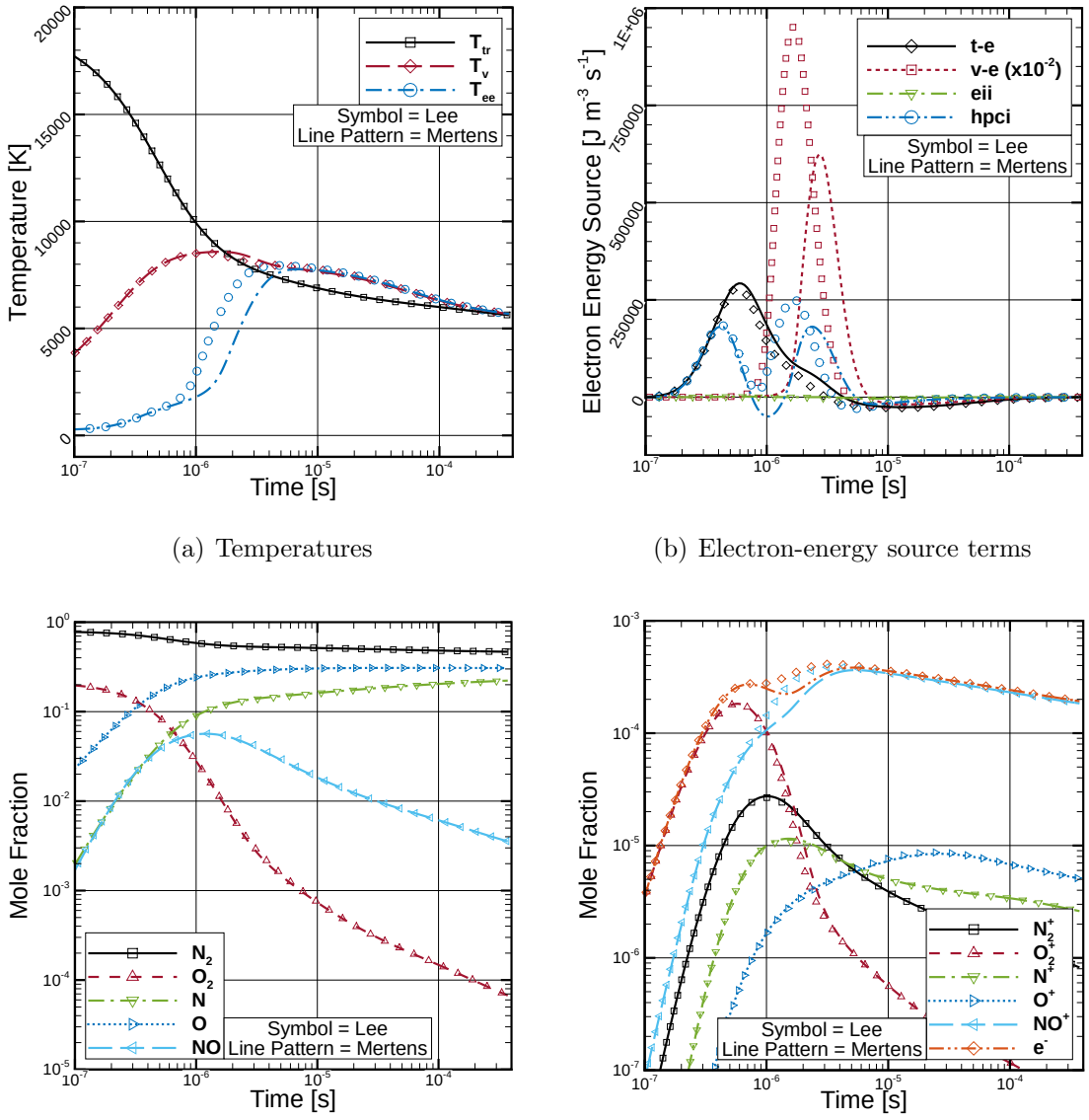

(a) Temperatures

(b) Electron-energy source terms

(c) Neutral species

(d) Charged species

Figure 7. Zero-dimensional Case 1, Mach 20 shock, comparison between the vibrational-electron energy relaxation times of Lee [64] and Mertens [74] for the electron-electronic three-temperature model.

heavy-particle collision ionization terms were comparable in magnitude to each other and were large enough to significantly contribute to the energy balance. Note that the simulation using the relaxation time of Mertens predicted the heavy-particle collision ionization term to dip below zero and become negative for a brief period. This was due to the Mertens' model predicting that the concentration of free-electrons to decrease thus causing the electron-ion recombination process to remove energy from the electrons. Lastly, the electron-impact ionization term was negligible when compared to the other terms, as well as the electron-impact dissociation term which is not shown in the figure.

The dominance of the NO^+ ion concentration toward the end of the simulation suggests that the seven-species air model, where NO^+ and e^- are the only charged species, would be appropriate. Figure 8 presents a comparison between the seven-species and eleven-species air models. Agreement was observed between the temperatures and electron concentrations toward the end of the simulation. However, the

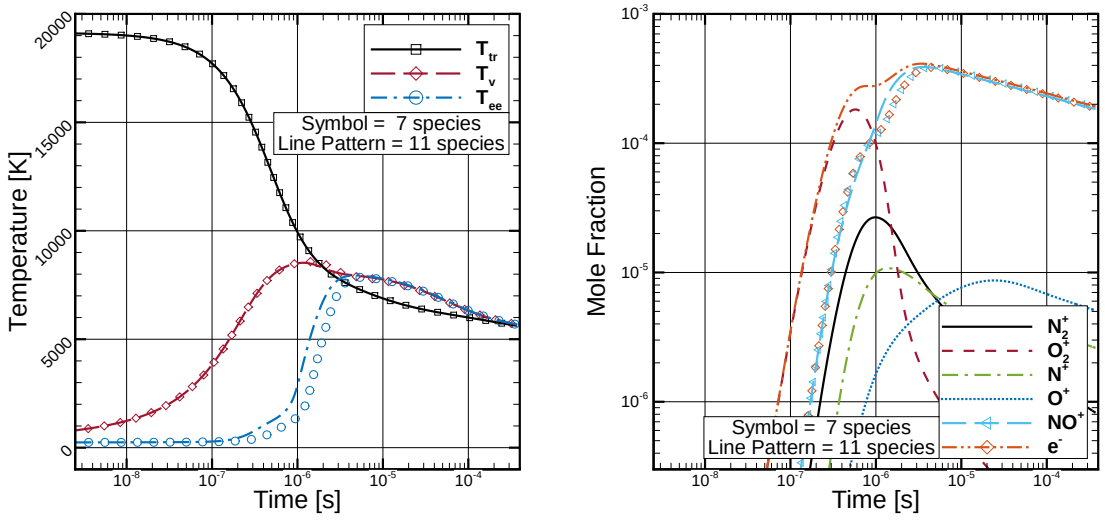

(a) Temperatures

(b) Charged species

Figure 8. Zero-dimensional Case 1, Mach 20 shock, comparison between the 7-species and 11-species air model for the electron-electronic three-temperature model. Lee's [64] relaxation time was utilized for the vibrational-electron energy exchange.

initial ionization reaction of O_2^+ produced the first electrons for the eleven-species model, thus the incubation period was shorter and equilibrium to the vibrational temperature occurred slightly sooner than the seven-species model.

3.2 Case 2: Compression – Mach 30 Shock

3.2.1 Case 2: Free-Electron Model

The results of Case 2, the simulated Mach 30 normal shock, using the free-electron model are presented in Figure 9 compared to results using the two-temperature model. The electron-vibration equilibration process was quicker than was observed for Case 1, which was expected due to the higher degree of non-equilibrium in the initial conditions for this case. After the very brief incubation period, the electron temperature remained in equilibrium with the vibrational temperature for the remainder of the

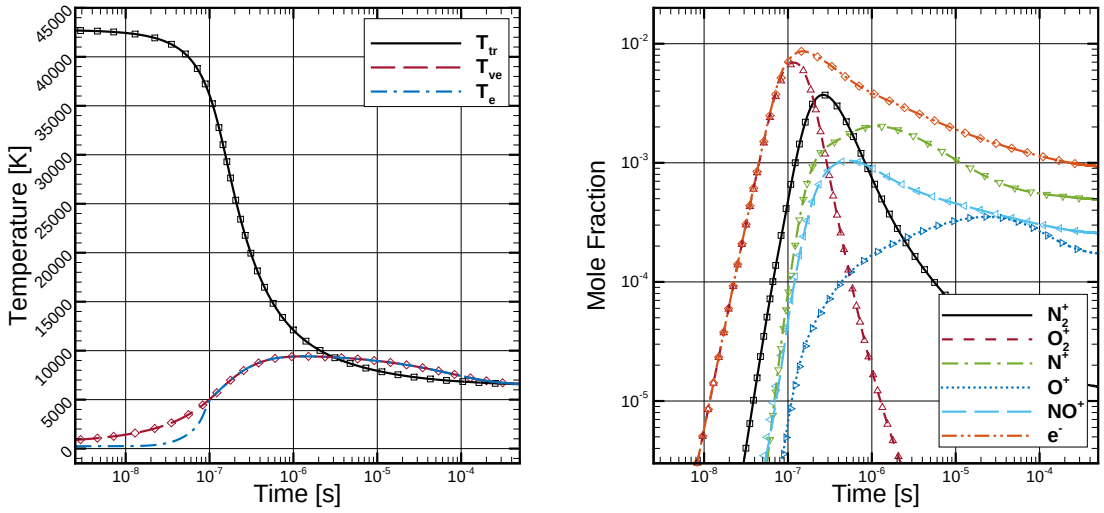

(a) Temperatures. ■ = T_{tr} ♦ = T_{vee}

(b) Charged species. ■ = N_2^+ ▲ = O_2^+ ▼ = N^+ ►= O^+ ◄= NO^+ ♦ = e^-

Figure 9. Zero-dimensional Case 2, Mach 30 shock, comparison between the two-temperature and free-electron three-temperature models. Lee's [64] relaxation time was utilized for the vibrational-electron energy exchange. Symbols are results from the two-temperature model.

simulation.

The charged species histories, Figure 9(b), agreed well with those predicted by the two-temperature simulation. The NO^+ stall, that was observed for Case 1, was not noticeable for Case 2 which is explained by the sooner equilibration of the electron temperature with the vibrational temperature. At the time of vibrational-electron equilibration the associated temperatures were lower than those of Case 1 which resulted in the electron-associative dissociation rate of NO^+ to be similar between the two models. Thus the stall in the production of NO^+ was less than what was observed in Case 1. Additionally, the dominant ionic species through the simulation varied from O_2^+ to N_2^+ then finally to N^+.

Figure 10 compares simulations using the relaxation times of Lee [64] and Mertens [74]. The results were almost indiscernible between the two relaxation models. The magnitudes of the translation-electron exchange, vibration-electron exchange, and production terms were all comparable, as can be seen in Figure 10(b). Similar to Case 1, the electron-impact ionization and dissociation terms were negligible.

3.2.2 Case 2: Electron-Electronic Model

Figure 11 presents the simulation of Case 2 using the electron-electronic three-temperature model compared to results using the two-temperature model. Similar to Case 1, there was an incubation period associated with the electron energy due to the limited number of electrons available for energy transfer early in the simulation. The electron-electronic temperature was less than the vibrational temperature, by approximately 1,000 K, through the early portion of the simulation until equilibrium between these two modes was reached.

The charged species concentrations, shown in Figure 11(b), were comparable between the electron-electronic three-temperature model and the two-temperature

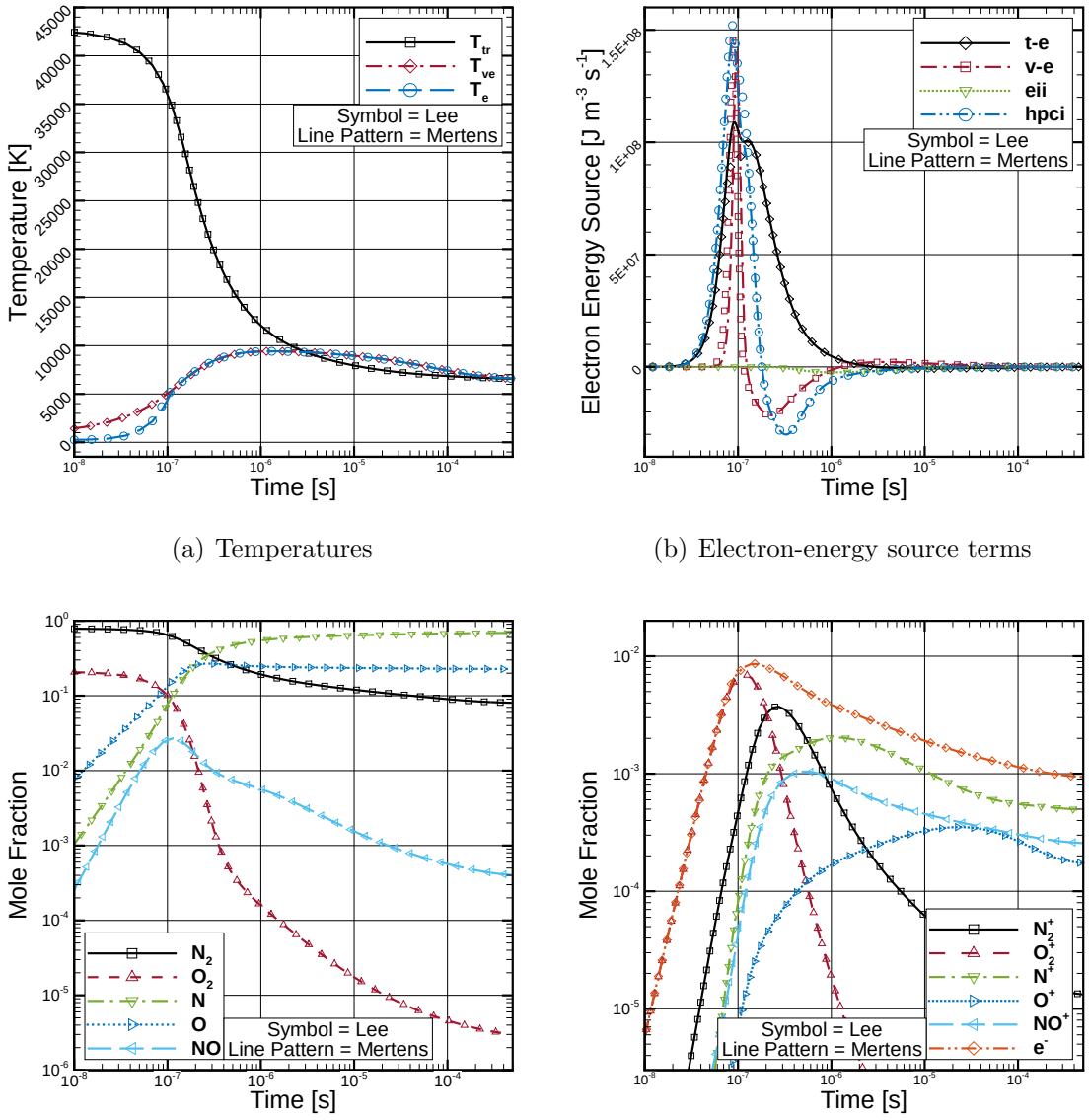

(a) Temperatures

(b) Electron-energy source terms

(c) Neutral species

(d) Charged species

Figure 10. Zero-dimensional Case 2, Mach 30 shock, comparison between the vibrational-electron energy relaxation times of Lee [64] and Mertens [74] for the free-electron three-temperature model.

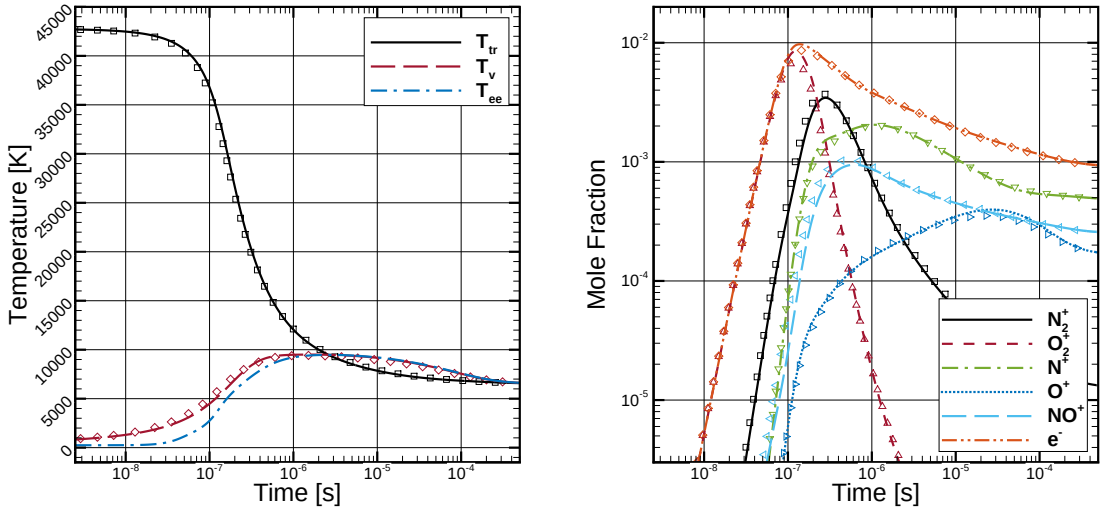

(a) Temperatures. ■ = T_{tr} ♦ = T_{vee}

(b) Charged species. ■ = N_2^+ ▲ = O_2^+ ▼ = N^+ ►= O^+ ◄= NO^+ ♦ = e^-

Figure 11. Zero-dimensional Case 2, Mach 30 shock, comparison between the two-temperature and electron-electronic three-temperature models. Lee's [64] relaxation time was utilized for the vibrational-electron energy exchange. Symbols are results from the two-temperature model.

model. The increased peak O_2^+ and stall in the NO^+ concentrations were still present in this simulation, but the magnitude of the differences were less than those observed for Case 1. The dominant charged species through the simulation were the same as those discussed for the free-electron model (O_2^+, N_2^+, and N^+), which indicates that the seven-species air model would be ill-suited for this case.

Simulations using the vibrational-electron relaxation times of Lee [64] and Mertens [74] are compared in Figure 12; results between the two simulations showed little differences. Again, the vibrational-electron exchange was the dominant term, but the contributions from the translational-electron exchange and production terms increased as compared to Case 1. However,the electron-impact ionization and dissociation terms were still negligibly small.

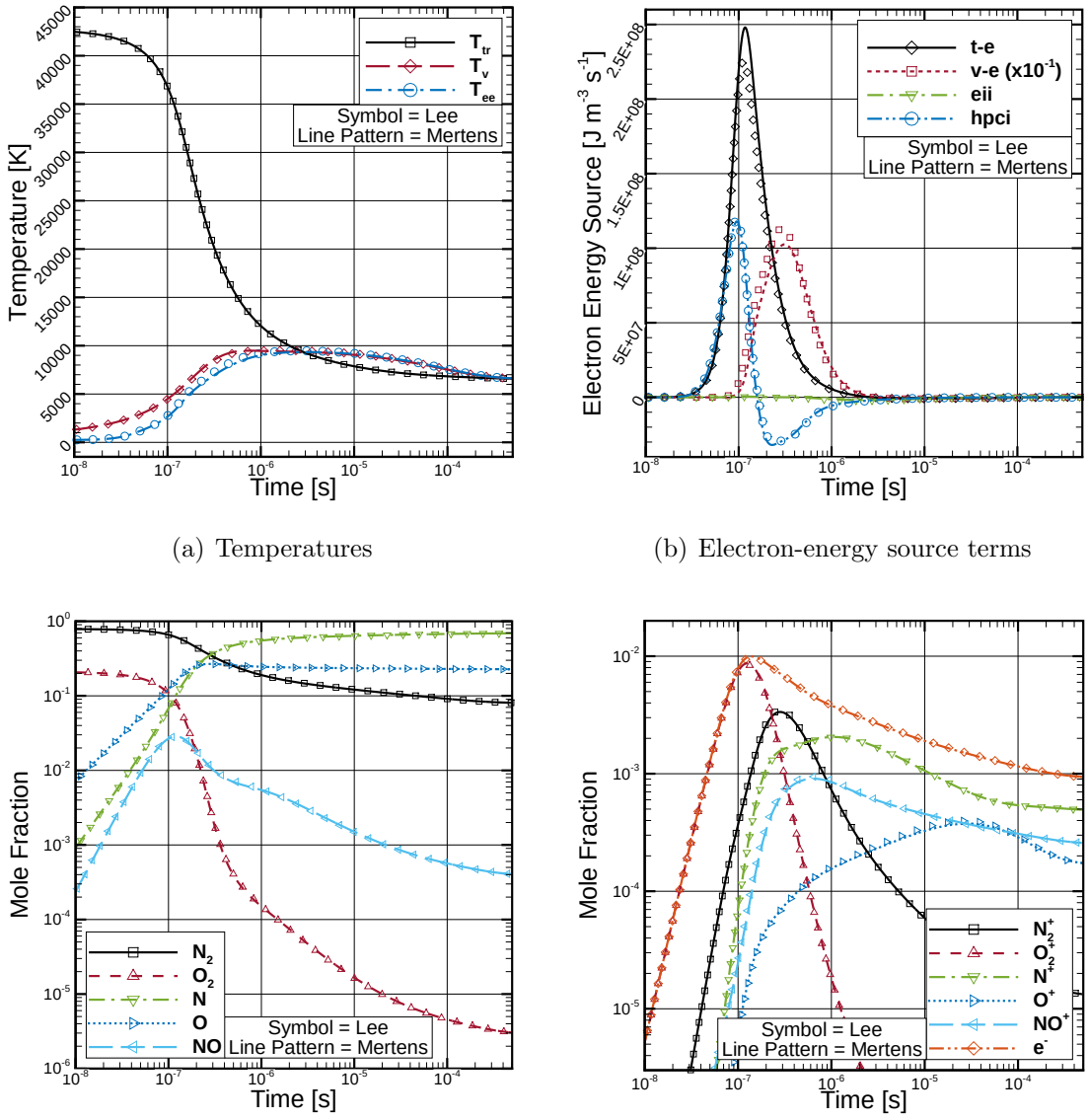

(a) Temperatures

(b) Electron-energy source terms

(c) Neutral species

(d) Charged species

Figure 12. Zero-dimensional Case 2, Mach 30 shock, comparison between the vibrational-electron energy relaxation times of Lee [64] and Mertens [74] for the electron-electronic three-temperature model.

3.3 Case 3: Compression – Mach 40 Shock

3.3.1 Case 3: Free-Electron Model

The results of the simulated Mach 40 normal shock, Case 3, using the free-electron three-temperature model are presented in Figure 13 compared to the results obtained using the two-temperature model. Unlike the previous cases, the electron temperature increased above the vibrational temperature during equilibration. The large amount of energy present in the translational-rotational temperature at the beginning of the simulation drove the ionization reactions to levels above those observed for the previous cases, which strengthened the translational-electron energy exchange process, thus increasing the electron temperature. The vibrational temperature of the free-electron model closely matched the two-temperature prediction very early in the simulation. However, as the simulation progressed the vibrational temperature

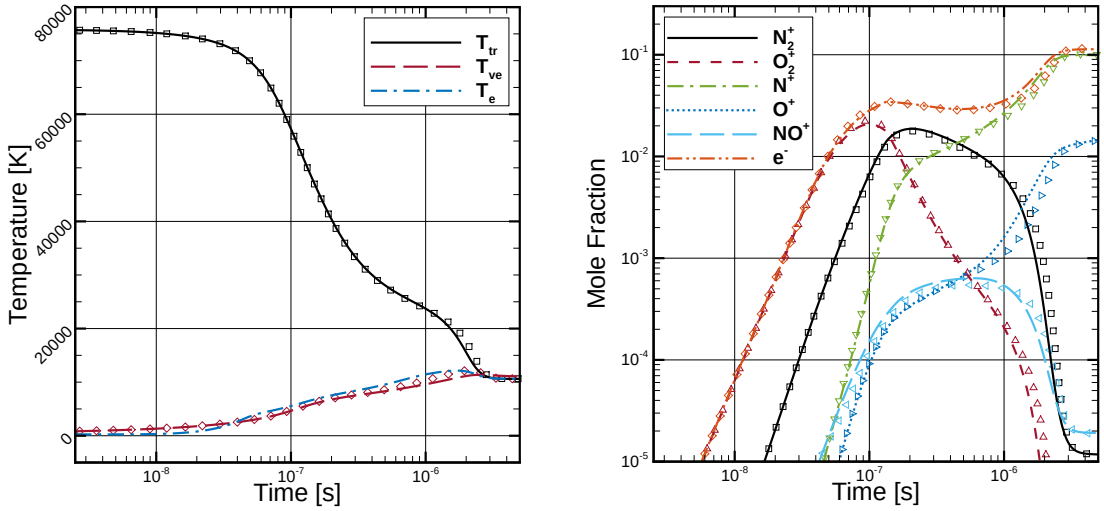

(a) Temperatures. ■ = T_{tr} ♦ = T_{vee}

(b) Charged species. ■ = N_2^+ ▲ = O_2^+ ▼ = N^+ ►= O^+ ◄= NO^+ ♦ = e^-

Figure 13. Zero-dimensional Case 3, Mach 40 shock, comparison between the two-temperature and free-electron three-temperature models. Lee's [64] relaxation time was utilized for the vibrational-electron energy exchange. Symbols are results from the two-temperature model.

of three-temperature model was lower than that of the two-temperature due to the inclusion of the free electron energy with vibrational for the two-temperature model.

The charged species concentrations matched closely between the two models early in the simulation. However, the free-electron model predicted a slightly higher level of ionization during the avalanche reaction at the final stages of the simulation. This reaction resulted from the large quantities of free-electrons and high temperatures which caused an explosion in ionization levels via the reactions

$$O + e^- \rightarrow O^+ + 2e^- \quad \text{and} \quad N + e^- \rightarrow N^+ + 2e^-.$$

The avalanche proceeded as two electrons were produced for every one electron involved in a reaction; thus, a cascading effect was created where more electrons were available to react. During this process, the higher electron temperature of the three-temperature model resulted in the rate coefficients of the forward reactions to be larger, leading to slightly higher ionization levels. The larger electron density increased the coupling of the translational-electron energy exchange, resulting in the translational-rotational temperature dropping rapidly, and final thermal equilibrium being attained quickly.

Figure 14 compares simulations using the relaxation times of Lee [64] and Mertens [74] for Case 3 using the free-electron three-temperature model. The stronger coupling of the vibrational and electron energies predicted by the Lee model resulted in these temperatures remaining closer together through the initial relaxation process. Figure 14(b) shows that all source terms, except electron-impact dissociation, contributed to the energy balance. The appearance of the electron-impact ionization source term as a contributing factor indicated that this term becomes important for conditions between those of Case 3 (Mach 30), where this term was negligible, and the present case (Mach 40).

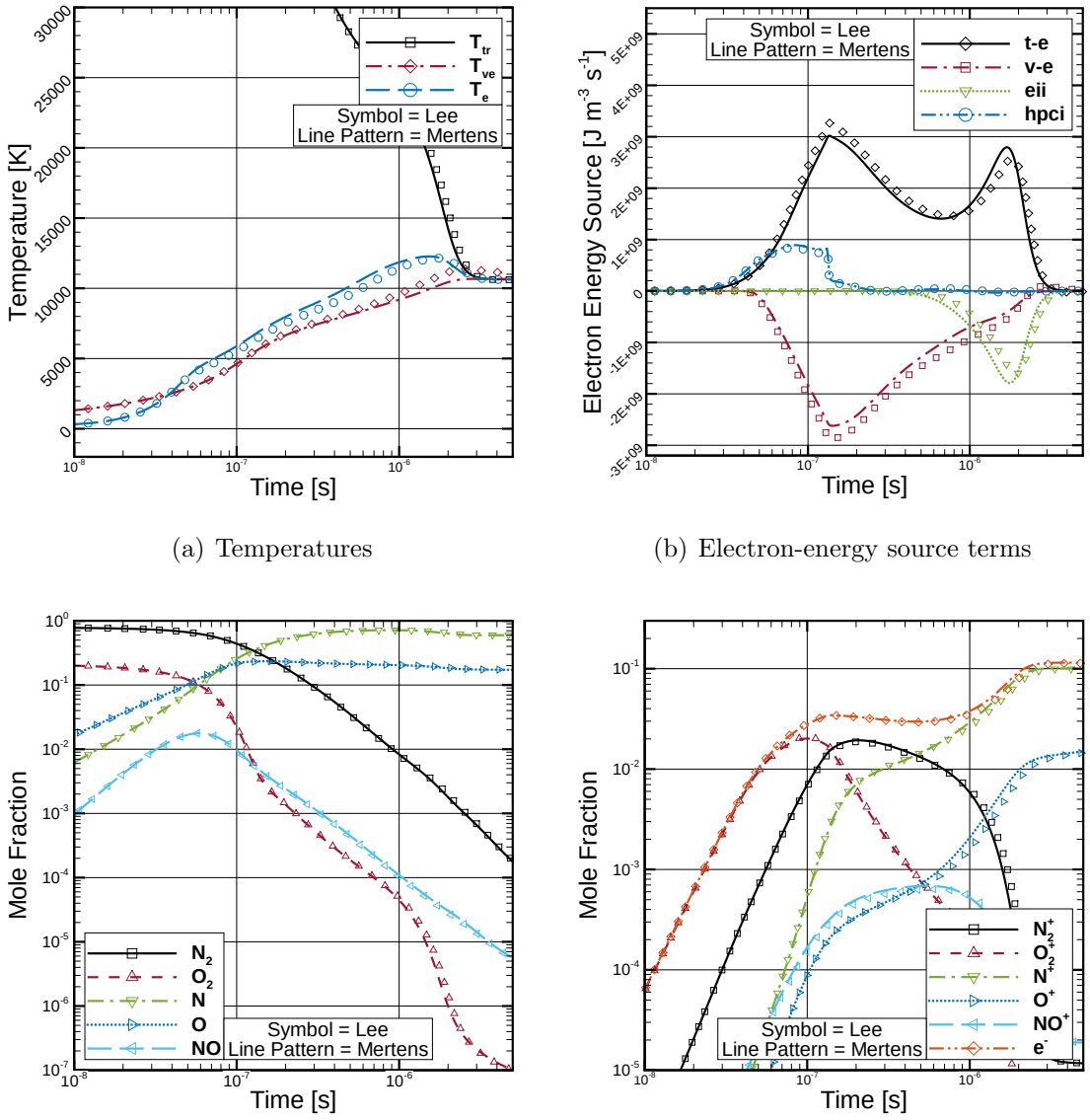

(a) Temperatures

(b) Electron-energy source terms

(c) Neutral species

(d) Charged species

Figure 14. Zero-dimensional Case 3, Mach 40 shock, comparison between the vibrational-electron energy relaxation times of Lee [64] and Mertens [74] for the free-electron three-temperature model.

3.3.2 Case 3: Electron-Electronic Model

The simulation of Case 3 using the electron-electronic three-temperature model is presented in Figure 15. The first 2×10^{-7} seconds were characterized by the initial production of free-electrons which increased the strength of translation-electron coupling. The resulting electron temperature was greater than the vibrational temperature by as much as 1,000 K. After this initial period, the electron-vibrational coupling worked to equilibrate these modes for the remainder of the simulation.

The electron avalanche ionization reaction, and thus the species concentrations, predicted by this model closely matched that of the two-temperature model since the electron-electronic energy was equilibrated with the vibrational energy at this point in the simulation.

Simulations using the relaxation times of Lee [64] and Mertens [74] are compared in Figure 16 which show the differences between the models were minimal for this

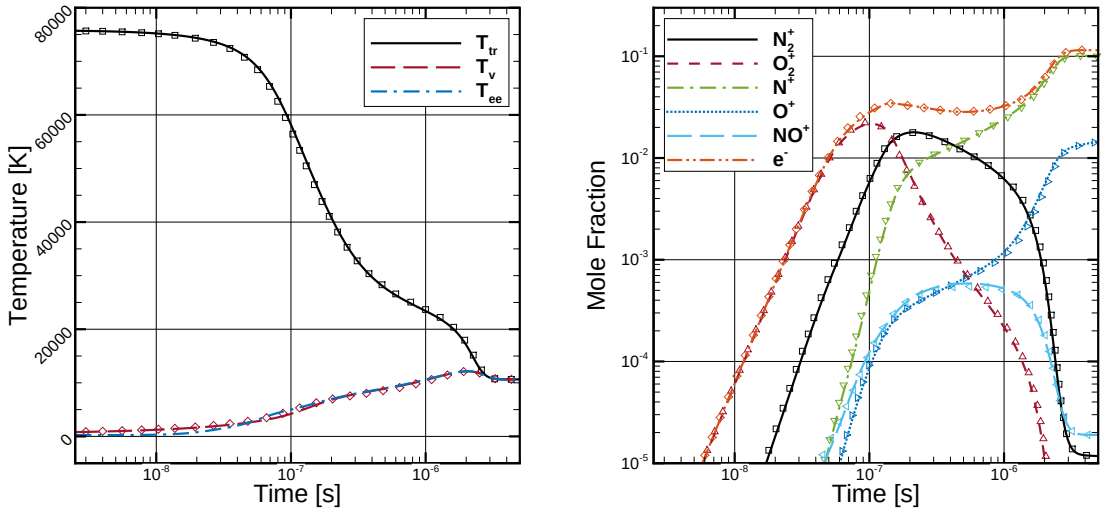

(a) Temperatures. ■ = T_{tr} ♦ = T_{vee}

(b) Charged species. ■ = N_2^+ ▲ = O_2^+ ▼ = N^+ ►= O^+ ◄= NO^+ ♦ = e^-

Figure 15. Zero-dimensional Case 3, Mach 40 shock, comparison between the two-temperature and electron-electronic three-temperature models. Lee's [64] relaxation time was utilized for the vibrational-electron energy exchange. Symbols are results from the two-temperature model.

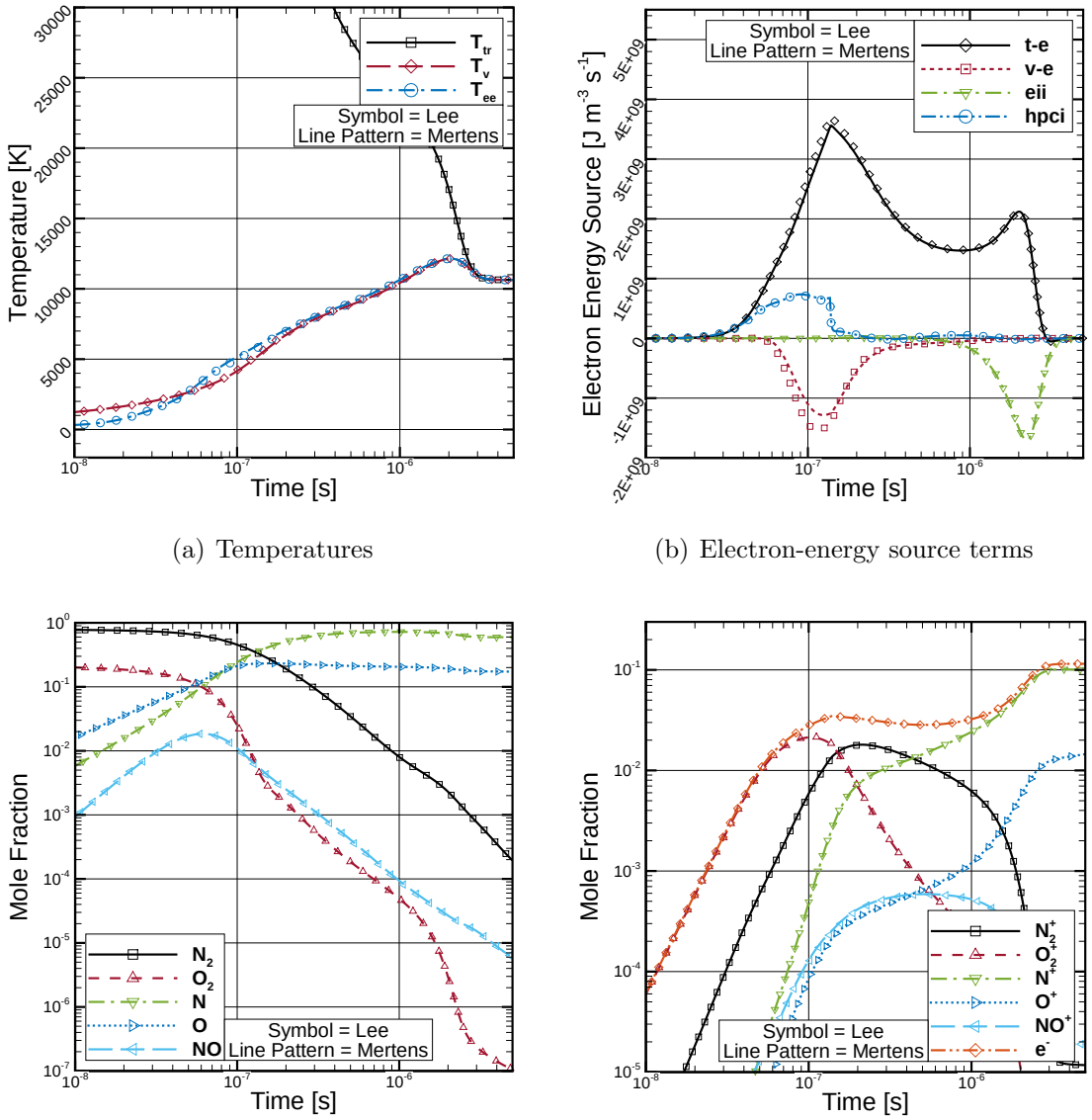

(a) Temperatures

(b) Electron-energy source terms

(c) Neutral species

(d) Charged species

Figure 16. Zero-dimensional Case 3, Mach 40 shock, comparison between the vibrational-electron energy relaxation times of Lee [64] and Mertens [74] for the electron-electronic three-temperature model.

case. Unlike the previous cases, the electron-impact ionization source term, shown in Figure 16(b), contributed significantly to the electron energy balance and cannot be neglected for this case. Cases 1 and 2 both exhibited similar energy flow patterns from the translational-rotational to vibrational and then to the electron translational mode; however, this case predicted a different energy cascade where the translational-rotational energy flowed to both the free-electron and vibrational modes with similar efficiencies. The beginning of the simulation even showed energy transfer from the electron translational mode to the vibrational mode.

3.4 Case 4: Expansion

3.4.1 Case 4: Free-Electron Model

Results using the free-electron model for the expansion simulation, Case 4, did not differ from results using the two-temperature model and are therefore not presented. A sufficient amount of free-electrons was available throughout the simulation to ensure the vibrational-electron coupling was strong, which resulted in these two energy modes staying in equilibrium with each other throughout the simulation.

3.4.2 Case 4: Electron-Electronic Model

The results of the expansion simulation, Case 4, using the electron-electronic three-temperature model is presented in Figure 17 compared to results using the two-temperature model. The time required for the simulation to relax to equilibrium was on the order of tens of seconds while all of the compression cases reached equilibrium in times on the order of 10^{-4} seconds. This long relaxation time suggests that a large portion of the wake of a hypersonic vehicle would remain in a state of non-equilibrium. During the relaxation process, the three-temperature model predicted a stall in the electron-electronic energy due to the depletion of free-electrons.

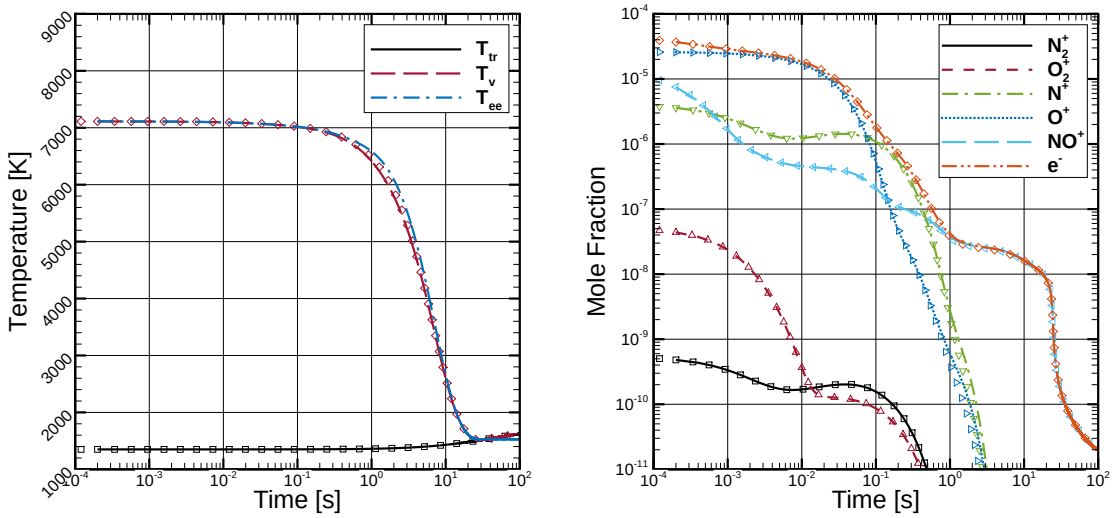

(a) Temperatures. ■ = T_{tr} ♦ = T_{vee}

(b) Charged species. ■ = N_2^+ ▲ = O_2^+ ▼ = N^+ ►= O^+ ◄= NO^+ ♦ = e^-

Figure 17. Zero-dimensional Case 4, simulated expansion conditions, comparison between the two-temperature and electron-electronic three-temperature models. Lee's [64] relaxation time was utilized for the vibrational-electron energy exchange. Symbols are results from the two-temperature model.

Therefore, the electron temperature was higher, by about 500 K, than the vibrational temperature as they both equilibrated with the translational-rotational temperature. This temperature difference is detailed in Figure 18(a) where the time axis is adjusted to highlight the thermal non-equilibrium process. Although the energy state of the electrons was only slightly higher than that of the vibrational energy, the persistence of this difference spans several seconds which suggests that the electron-electronic three-temperature model has potential to increase the fidelity of the simulations of the wake flow-fields behind hypersonic vehicles.

Figure 18 compares simulations of the expansion case using the relaxation times of Lee [64] and Mertens [74]. Similar to the compression cases, the relaxation time of Lee predicted a slightly stronger coupling of the electron-electronic energy to the vibrational energy. The source terms to the electron-electronic energy are shown in Figure 18(c): the initial abundance of free electrons forced the electron-electronic

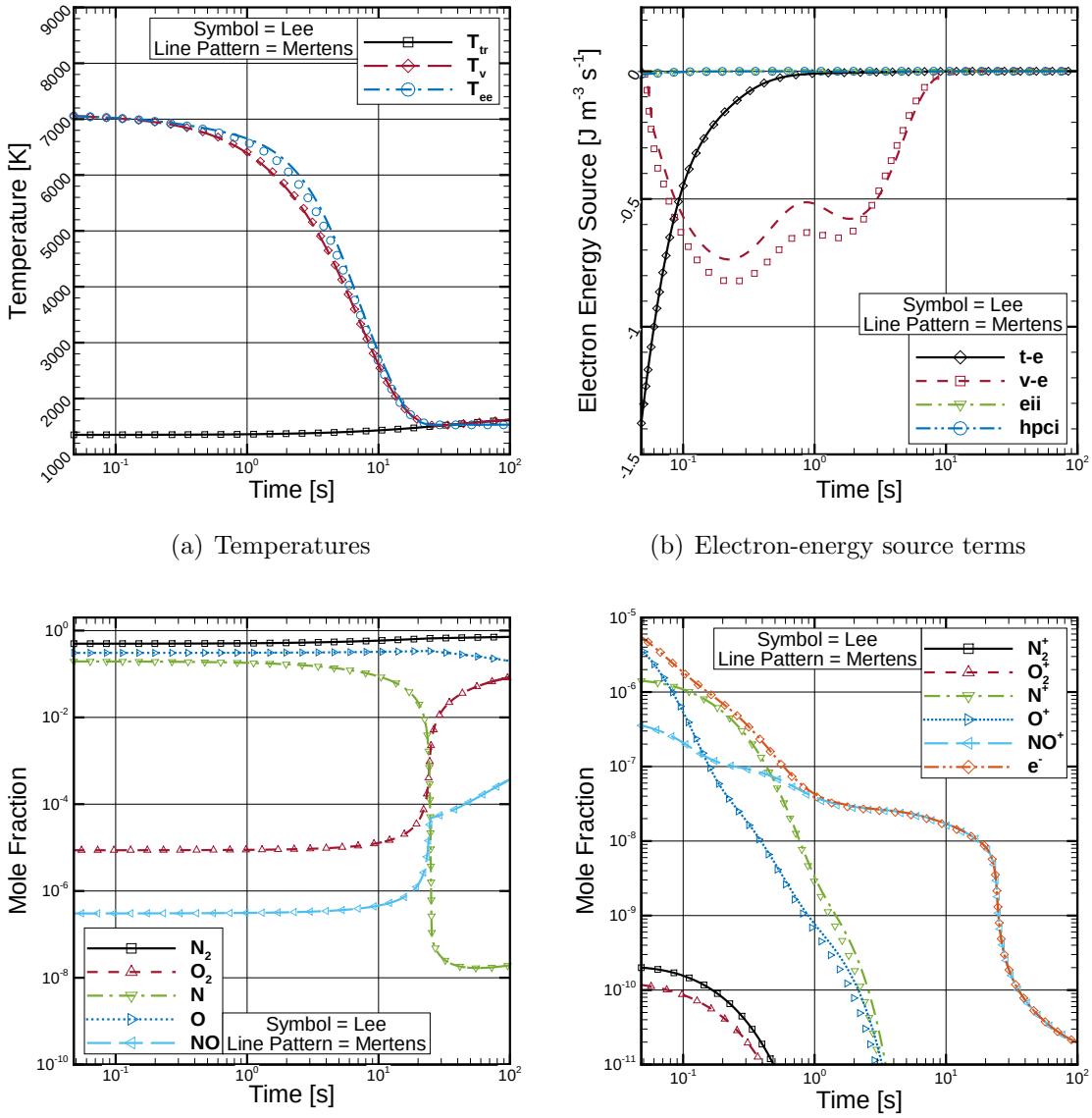

(a) Temperatures

(b) Electron-energy source terms

(c) Neutral species

(d) Charged species

Figure 18. Zero-dimensional Case 4, simulated expansion conditions, comparison between the vibrational-electron energy relaxation times of Lee [64] and Mertens [74] for the electron-electronic three-temperature model.

energy to remain equilibrated with the vibrational energy. As electron-ion recombination reactions proceeded, the relaxation time, which is proportional to the inverse of the electron number-density, increased causing the electron-electronic energy to freeze. Then, as the non-equilibrium potential between the vibrational and electron-electronic energies grew, the numerator of the vibrational-electron relaxation term, Equation (38), increased and the electron-electronic energy proceeded to equilibrate with the vibrational energy.

3.5 Approximate Vibrational Relaxation

The Landau-Teller relaxation of vibrational energy was simplified by Gnoffo, Gupta, and Shinn [39] to limit the number of species-dependent variables in order to reduce computational costs and to provide a simple relation that directly depends on the temperature difference. These approximate relations are utilized within FUN3D as well as the legacy LAURA code. In order to quantify the validity of this approximation, two zero-dimensional simulations were completed using the two-temperature model. The approximation to the Landau-Teller relaxation process is

$$\sum_s \rho_s \frac{e_{v,s}^{T_t} - e_{v,s}}{\tau_s^{t-v}} \approx \frac{\rho c_v^v}{\bar{\tau}^{t-v}} \left(T_t - T_v\right), \tag{123}$$

where

$$\frac{1}{\bar{\tau}^{t-v}} = \sum_{s=mol.} \frac{X_s}{\tau_s^{t-v}}, \tag{124}$$

and the mixture specific heat of vibrational energy is

$$c_v^v = \sum_s c_s c_{v,s}^v. \tag{125}$$

Note that the species specific heat at constant volume for vibrational energy, $c^v_{v,s}$, is evaluated at the vibrational temperature.

The first simulation was of Case 1, the simulated Mach 20 normal shock. The temperature and Landau-Teller term time-histories are presented Figure 19. The detailed Landau-Teller simulation utilized the representation on the left side of Equation (123) and the approximate results utilized the expression on the right side. Overall, the approximate model was slower to react to the initial conditions due to c^v_v being near zero at the initial vibrational temperatures of the simulation. The differences between the vibrational temperatures was as much as 3,000 K. Additionally, the approximate model resulted in less of an overshoot of the vibrational temperature above the translational-rotational temperature.

The second simulation was of Case 4, the simulated expansion flow. The time histories of the temperatures and Landau-Teller term are presented in Figure 20. Although the time to reach equilibration was similar between the two models, the

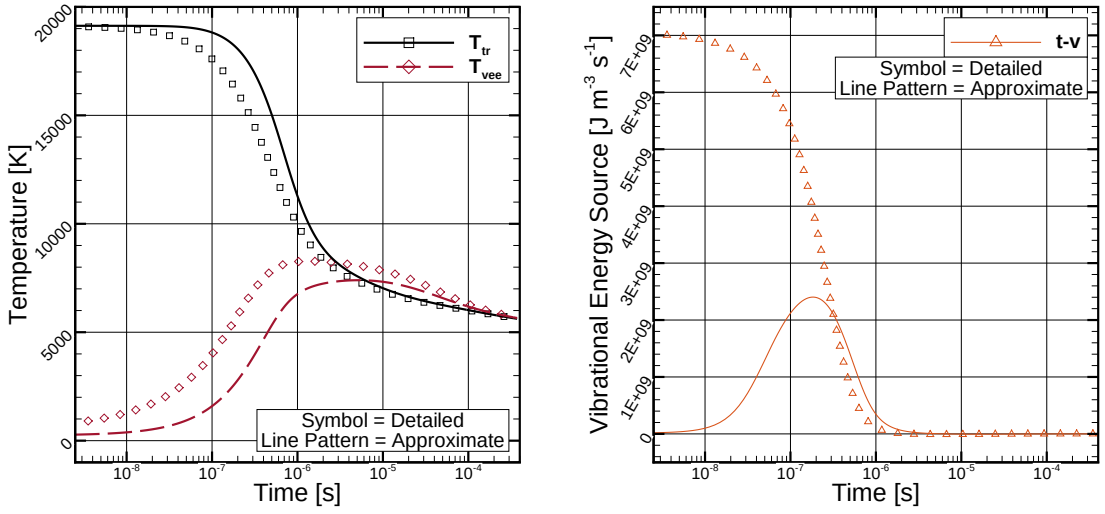

(a) Temperatures

(b) Translational-vibrational energy exchange

Figure 19. Zero-dimensional Case 1, Mach 20 shock, comparison of the detailed and approximate Landau-Teller translational-vibrational energy relaxation using the two-temperature model.

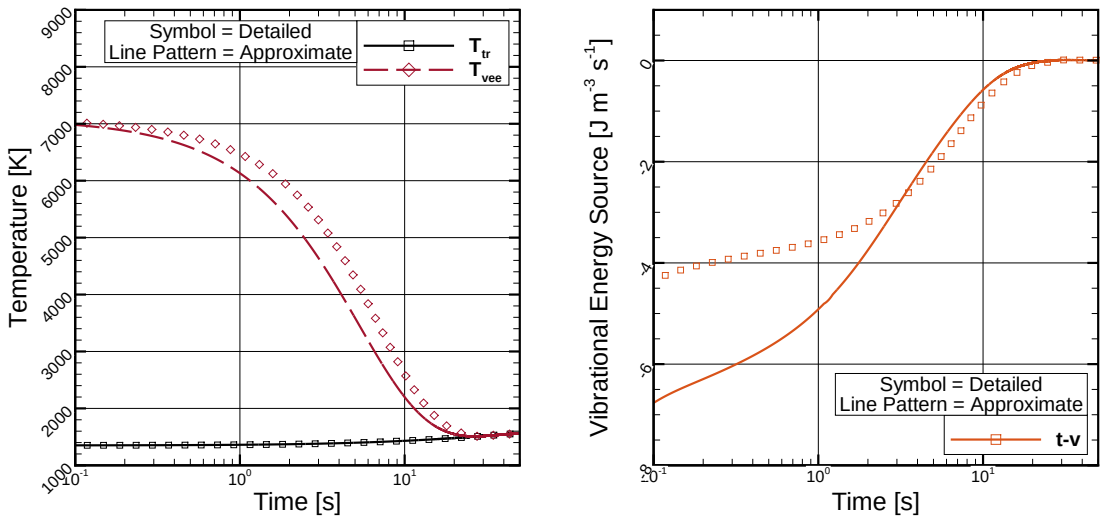

(a) Temperatures (b) Translational-vibrational energy exchange

Figure 20. Zero-dimensional Case 4, simulated expansion conditions, comparison of the detailed and approximate Landau-Teller translational-vibrational energy relaxation using the two-temperature model.

vibrational temperature of the approximate formulation was lower by approximately 500 K during the relaxation processes. The larger source term predicted by the approximate model early in the simulation was due to c_v^v being large at high vibrational temperatures.

Even though the approximate Landau-Teller relations have been used extensively in the past, the detailed, original formulation was utilized for all simulations within this dissertation. This choice is made based on the results given in this section which show that there is a significant difference in the thermal state of the gas between these two formulations.

3.6 Zero-Dimensional Simulation Conclusions

The three-temperature models developed in Chapter II were investigated by conducting several zero-dimensional simulations. Results were compared to simulations using the legacy two-temperature model in order to assess if the inclusion of a third

temperature added fidelity to the relaxation processes. Additionally, the contributions from the various electron energy source terms were highlighted to determine the importance of their inclusion to the electron energy balance. The electron-electronic three-temperature model showed the most promise in accurately capturing the physics governing electron energy non-equilibrium for the majority of conditions applicable to hypersonic flows.

Even though the free-electron three-temperature model did exhibit variations from the two-temperature model, the results need to be carefully characterized. For the Mach 20 and 30 simulations, Case 1 and 2, the electron temperature behaved as physics suggests by lagging behind the vibrational temperature during the initial equilibration. This delay was extremely brief, less than 10^{-6} seconds, before the electron and vibrational modes equilibrated, from which point the thermochemical state did not differ from that predicted by the two-temperature model. The free-electron model for the Mach 40 simulation, Case 3, resulted in the electron temperature exceeding the vibrational temperature by a significant amount and the resulting thermochemical state differing from the two-temperature model. However, the levels of ionization present in this case were high, with the equilibrium concentrations of free-electrons exceeding 10%. With these large electron concentrations, it is expected that the electron-impact electronic-excitation process, which is neglected in the free-electron model, would be significant. At this high Mach number condition, the free-electron model did not revert back to the two-temperature model but instead produced a physically improbable state of the free-electron energy. Therefore, the free-electron model is ill-suited for high Mach number flows. Additionally, the results of the expansion simulation, Case 4, using the free-electron model did not differ from the results of the two-temperature model; therefore, the utility of this model to capture additional physics and increase the accuracy of wake flow-field simulations may be limited.

On the other hand, simulations using electron-electronic three-temperature model exhibited behaviors that were explainable by physics for all cases considered. The results of the compression simulations, Cases 1-3, showed the electron temperature lagged behind the vibrational temperature throughout the relaxation process. The degree of this lag became less as the Mach number for the simulated shock increased; there was little difference between the three-temperature and two-temperature models for the simulated Mach 40 shock, Case 3. Finally, Case 4 showed the potential of the three-temperature model to more accurately predict the thermochemical state of the fluid in expansion regions, where, due to the depletion of free-electrons, the electron-electronic energy was the slowest manifold to equilibrate. It is therefore reasoned that the electron-electronic three-temperature model captured additional non-equilibrium physics and increased the accuracy of the predicted thermochemical state of the fluid above that of the two-temperature model.

The vibrational-electron relaxation times of Lee [64] and Mertens [74], presented in Section 2.9.3, were used to simulate the N_2 vibrational and electron translational energy exchange process. The Lee model predicted a quicker equilibration of these energy modes for all cases considered. However, the differences between the two models were generally small which showed that the thermochemical state of the fluid was relatively insensitive to which model was used.

The contributions from the various source terms to the electron energy balance were also characterized. The dominant source term to the electron energy balance was the vibration-electron exchange process. The contributions from the exchange of heavy-particle translational and electron translational energies and from the production of electron energy from heavy-particle collision ionization reactions increased with shock wave strength. Additionally, as the Mach number of the shock wave increased above 30, the contributions from electron-impact ionization reactions decreasing the

electron energy needed to be considered. Lastly, decrease of energy associated with electron-impact dissociation reactions did not significantly contribute to the energy balance for all cases considered.

Finally, the validity of the approximate formula for Landau-Teller vibrational relaxation, given by Gnoffo, Gupta, and Shinn [39], was investigated. For both the compression and expansion cases that were simulated, the results between the detailed and approximate formulations differed significantly; therefore, the original, detailed approach is preferred.

IV. RAM C-II

The RAM C-II flight experiment used microwave reflectometers and electrostatic probes to measure the electron number-density in the flow-field around a hypersonic spherically-blunted cone [55]. The vehicle geometry is depicted in Figure 21: the nose diameter was 30.48 cm, the cone half-angle was 9 degrees, and the overall length was 129.54 cm. Data was collected over the altitude range of 85.3 km to 53.3 km; the maximum speed of the vehicle was approximately 7,620 $\mathrm{m\,s^{-1}}$. This data has been of high importance for CFD code validation purposes due to the scarcity of flight experiments in the hypersonic regime and has been used for comparison to computational results in the development of numerous thermochemical non-equilibrium models [24, 33, 38, 43, 44, 56, 59, 91]. Therefore, the three-temperature models, developed in Chapter II, were used to simulate two trajectory points of the RAM C-II flight test to validate the models against the experimental data.

The three-temperature models were implemented within the FUN3D architecture, which is a node centered, finite volume CFD software suite. The boundary conditions included supersonic inflow and outflow, symmetry relations appropriate for axisym-

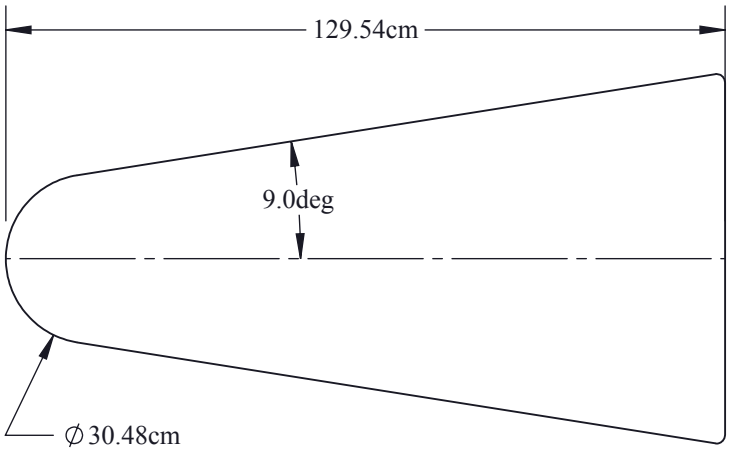

Figure 21. RAM C-II vehicle geometry.

Table 5. RAM C-II Freestream Conditions

Altitude [km]	Velocity [$\mathrm{m\,s^{-1}}$]	Temperature [K]	Density [$\mathrm{kg\,m^{-3}}$]	Mach Number
61	7651	243	2.54×10^{-4}	24.5
71	7660	215	6.42×10^{-5}	25.9

metric simulations, and viscous wall. The wall temperature was held constant at 1,000 K, which was consistent with the bulk of the previous works on this geometry, and full thermal equilibrium was assumed. Additionally, the wall was considered to be non-catalytic for neutral species and fully catalytic to ionic species [84]. Diffusion was modeled by the approximate relation of Equation (85); however, this approximation was investigated in Section 4.4 by employing two additional diffusion models. The two trajectory points considered in the current work are detailed in Table 5.

4.1 Grid Convergence

An axisymmetric grid that extended over 40 body-lengths into the wake was utilized. An example grid, highlighting the fore-body and near wake region, is shown in Figure 22. A grid convergence study was completed; the size parameters for the three grids considered are presented in Table 6. The maximum electron number-densities normal to the surface for both trajectory points and all three grid resolutions are pre-

Table 6. RAM C-II Grid Refinement

Level	Total Number of Points	Forebody Domain Nodes (normal×surface)
Coarse	107,751	107×160
Medium	429,324	215×320
Fine	1,713,072	428×639

sented in Figure 23. The translational-rotational temperature along the stagnation streamline and along a streamline in the wake is presented for the three grid resolutions in Figure 24 for the 61 km trajectory point. All of the aforementioned figures show that grid independence was sufficiently obtained throughout the domain with the medium resolution grid. Therefore, the medium resolution grid was utilized for the remainder of this study. Note that only convergence results obtained using the electron-electronic three-temperature model are presented; however, simulations were

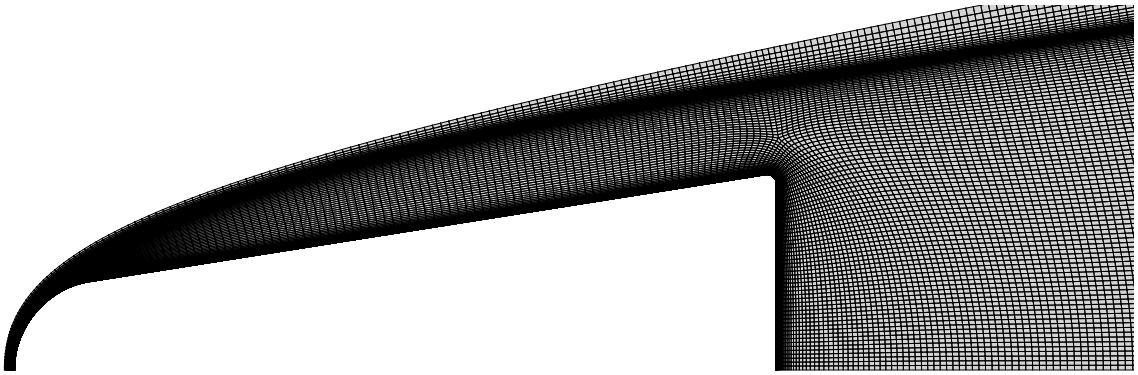

Figure 22. RAM C-II axisymmetric mesh.

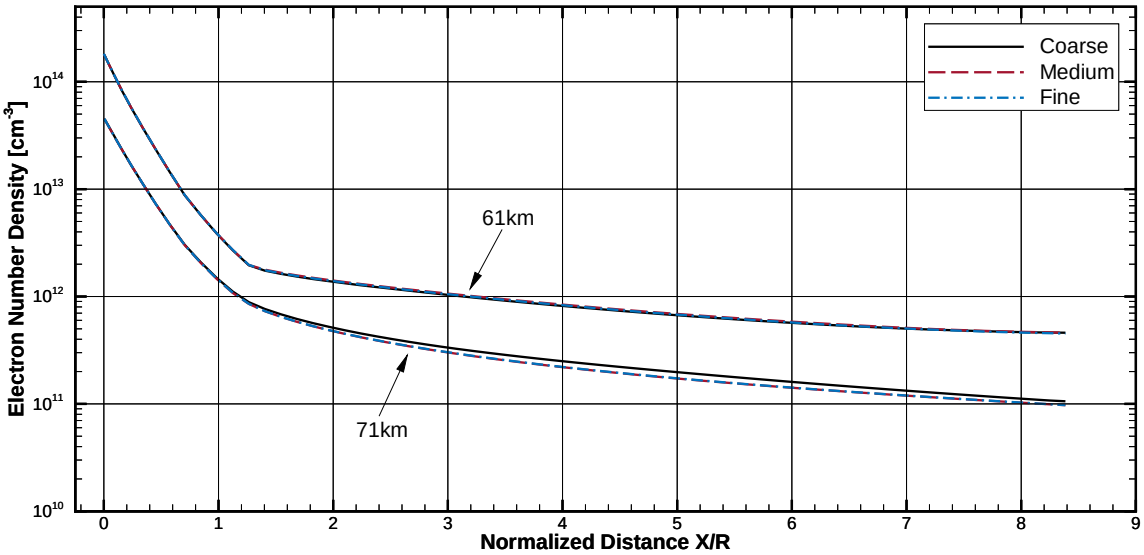

Figure 23. RAM C-II grid convergence for the electron-electronic model; maximum electron number density, normal to the surface, as a function of distance axially from the nose.

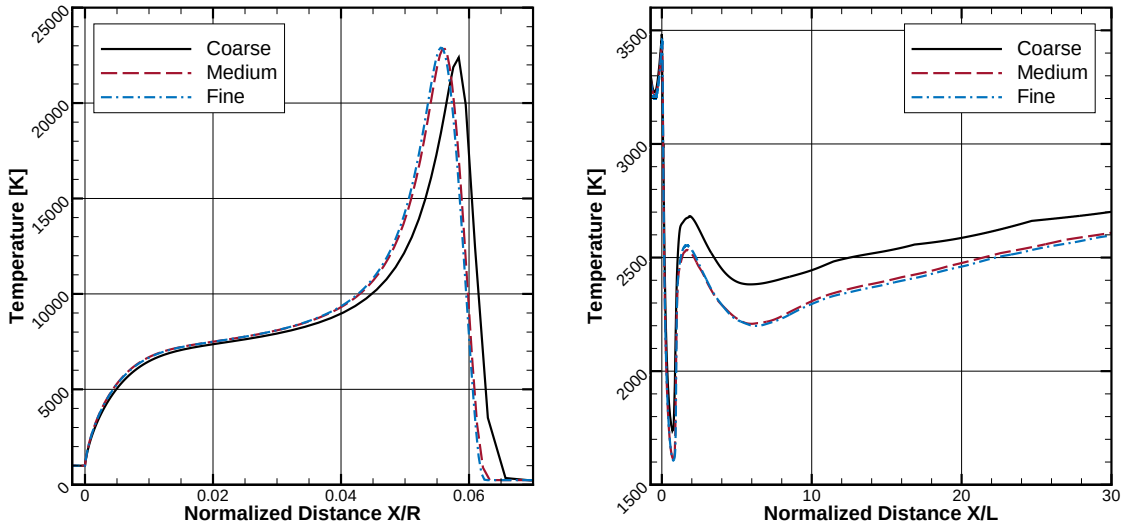

(a) Translational-rotational temperature along the stagnation streamline.

(b) Translational-rotational temperature along a streamline in the wake. $X/L = 0$ is the base of vehicle and L is the vehicle length.

Figure 24. RAM C-II grid convergence for the electron-electronic model and the 61 km trajectory point.

completed using the two-temperature and free-electron three-temperature models and identical conclusions for grid convergence were obtained.

4.2 Forebody Flow-Field

Electron number-densities computed using the three-temperature models and an eleven-species air model are compared to the RAM C-II flight test data in Figure 25. The maximum electron number-density, normal to the surface, is plotted versus the axial distance from the nose. The averaged reflectometer measurements from the flight test are represented by diamond symbols, ♦, and the electrostatic probe measurements by square symbols, ■, where the error bars represents the peak-to-peak values measured in flight [55]. Also shown for comparison are results obtained using the two-temperature model. Overall the electron number-densities computed using the three-temperature models agreed well with the experimental data for both

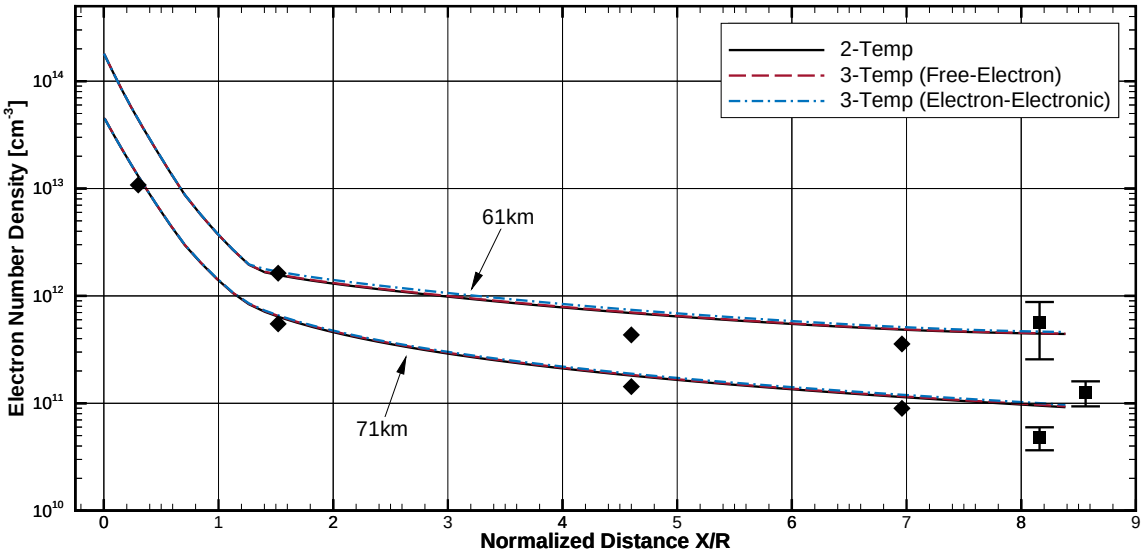

Figure 25. RAM C-II simulations compared to experimental data; maximum electron number-density, normal to the surface, as a function of distance axially from the nose. Experimental data from Jones *et al.* [55]: ♦ = average reflectometer measurements, ■ = electrostatic probe measurements where the error bars represent the peak-to-peak variation.

the 61 km and 71 km trajectory points. Additionally, the three-temperature model results were almost indistinguishable from those obtained using the two-temperature model, suggesting that the two-temperature model sufficiently captured the degree of ionization within the flow-field along the forebody.

The temperature and charged species concentrations along the stagnation streamline for the 61 km trajectory point are presented in Figures 26 and 27 for the free-electron and electron-electronic three-temperature models, respectively. Results using the two-temperature model are shown as symbols for comparison. The relaxation of the electron energy to the vibrational energy was quick for both three-temperature models. Considering the free-electron model, Figure 26(a), the electron temperature closely matched the vibrational for the majority of the shock layer, which was also indistinguishable from that predicted by the two-temperature model. There was a spike in the electron temperature immediately post-shock that has been determined to be due to a numerical instability that arose from the trace amount of free-electrons in

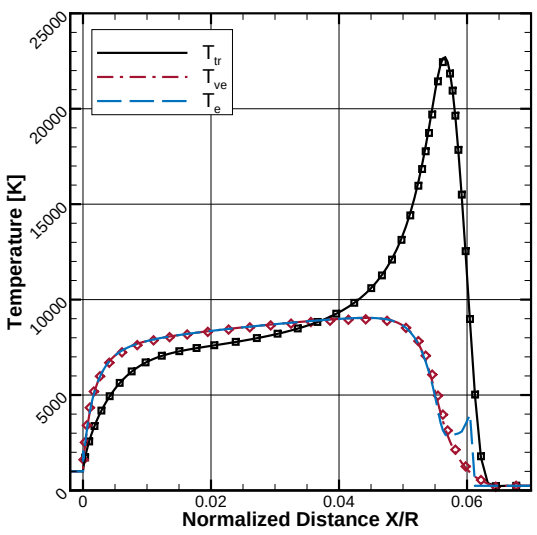

(a) Temperatures. ■ $= T_{tr}$ ♦ $= T_{vee}$

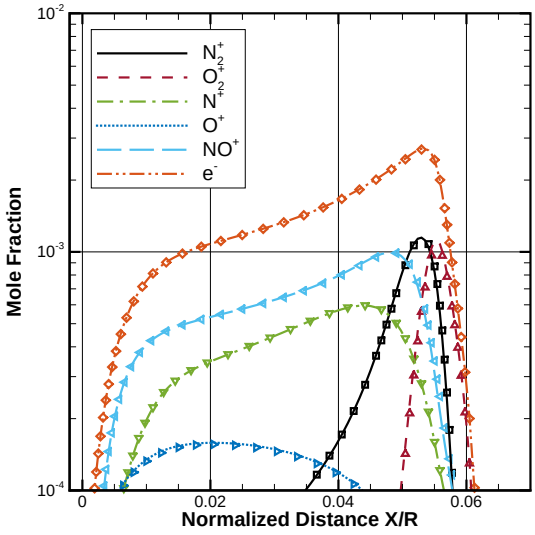

(b) Charged species. ■ $= N_2^+$ ▲ $= O_2^+$ ▼ $= N^+$ ►$= O^+$ ◄$= NO^+$ ♦ $= e^-$

Figure 26. RAM C-II stagnation streamline for the 61 km trajectory point and free-electron three-temperature model. Symbols are results from the two-temperature model.

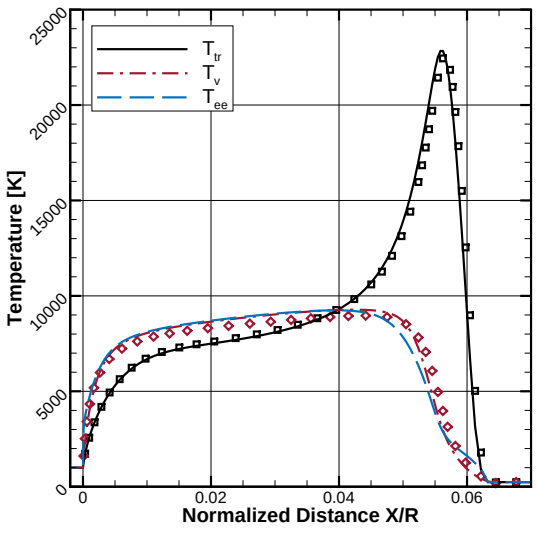

(a) Temperatures. ■ $= T_{tr}$ ♦ $= T_{vee}$

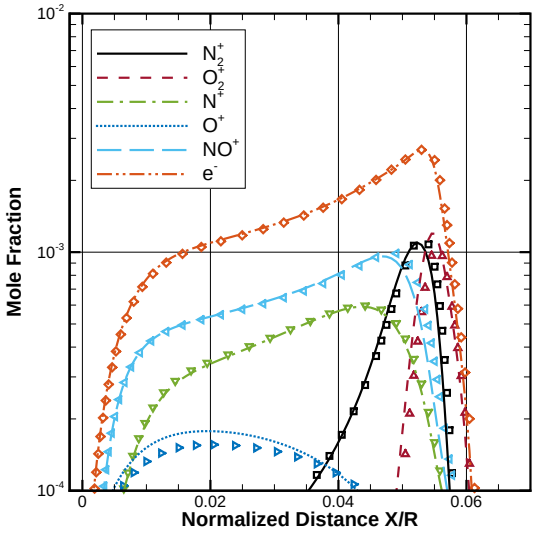

(b) Charged species. ■ $= N_2^+$ ▲ $= O_2^+$ ▼ $= N^+$ ►$= O^+$ ◄$= NO^+$ ♦ $= e^-$

Figure 27. RAM C-II stagnation streamline for the 61 km trajectory point and electron-electronic three-temperature model. Symbols are results from the two-temperature model.

the freestream. However, the error introduced by this spike was negligible due to the microscopic magnitude of the energy in this mode at that location. A greater degree of non-equilibrium between the electron and vibrational modes was observed for the electron-electronic three-temperature model, Figure 27. Equilibration of the electron-electronic and vibrational energies was slower than the free-electron model due to the larger electron-electronic energy manifold. The chemical state along the stagnation streamline for both three-temperature models closely matched that predicted by the two temperature model; the charged species mole fractions are presented in Figures 26(b) and 27(b), which demonstrates this point.

The temperatures and charged species concentrations along the stagnation streamline for the 71 km trajectory point are presented in Figures 28 and 29 for the free-electron and electron-electronic three-temperature models, respectively. The most obvious differences from the 61 km point was due to the more rarefied conditions at 71 km which resulted in the shock wave being more diffuse and the translational temperature exhibiting a smoother distribution through the shock wave. The low density conditions also resulted in the Landau-Teller translational-vibrational relaxation process being weaker than the 61 km point; thus, the vibrational temperature was slower to equilibrate. The free-electron model predicted the electron temperature to be larger than the vibrational temperature post shock due to it's coupling with the translational mode. The spike in the electron temperature, commensurate with the shock wave, was more pronounced than the 61 km point; again, the error introduced was minimal due to the trace number of electrons at the spike location. After the electron and vibrational modes equilibrated, their temperatures remained identical over the remainder of the streamline. The electron-electronic model predicted the electron-electronic energy to remain in a state of non-equilibrium with the vibrational energy for a majority of the shock layer, with the final equilibrium temperatures be-

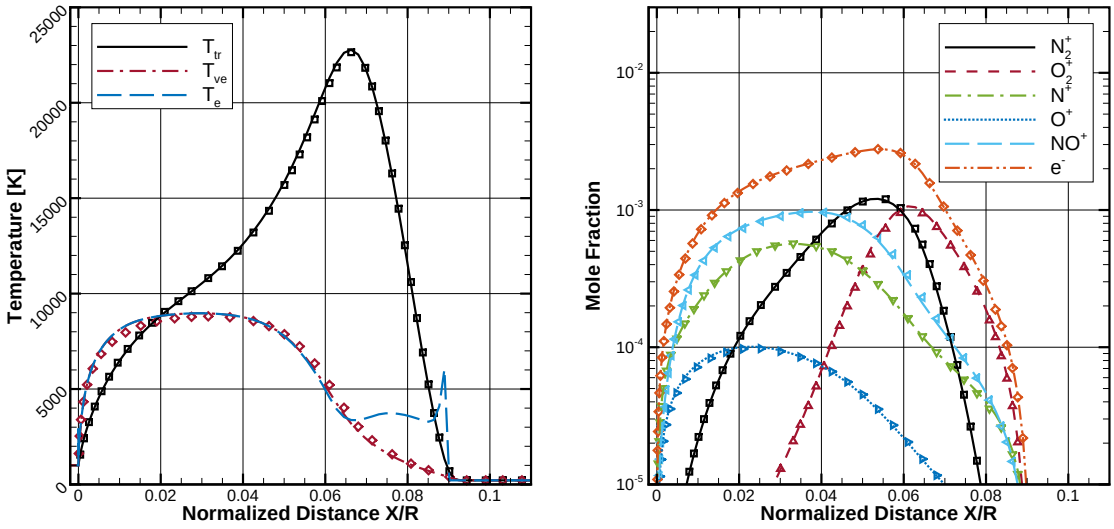

(a) Temperatures. ■ $= T_{tr}$ ♦ $= T_{vee}$

(b) Charged species. ■ $= N_2^+$ ▲ $= O_2^+$ ▼ $= N^+$ ►$= O^+$ ◄$= NO^+$ ♦ $= e^-$

Figure 28. RAM C-II stagnation streamline for the 71 km trajectory point and free-electron three-temperature model. Symbols are results from the two-temperature model.

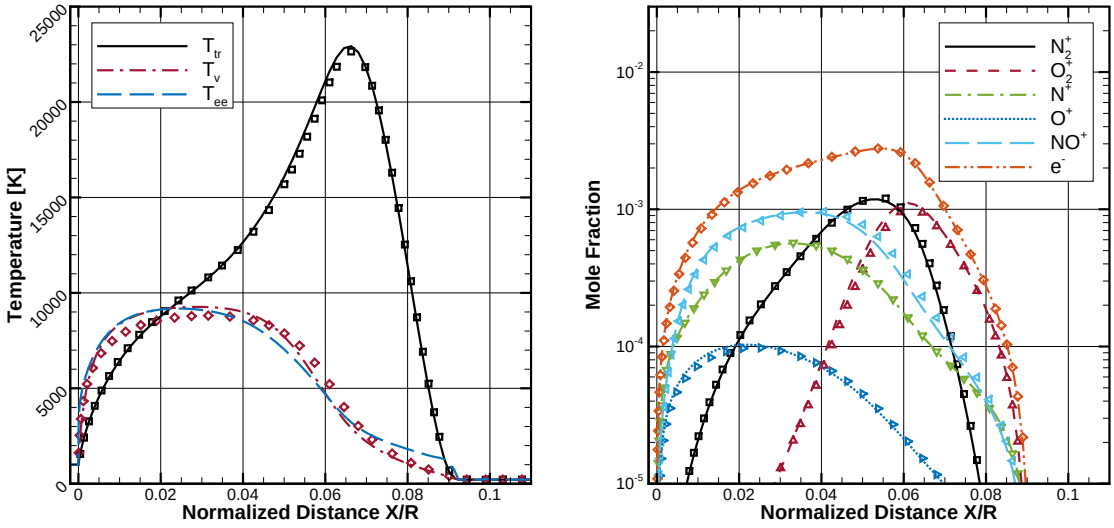

(a) Temperatures. ■ $= T_{tr}$ ♦ $= T_{vee}$

(b) Charged species. ■ $= N_2^+$ ▲ $= O_2^+$ ▼ $= N^+$ ►$= O^+$ ◄$= NO^+$ ♦ $= e^-$

Figure 29. RAM C-II stagnation streamline for the 71 km trajectory point and electron-electronic three-temperature model. Symbols are results from the two-temperature model.

ing slightly higher than the vibrational temperature of the two-temperature model. Lastly, the chemical state predicted by the three-temperature models closely matched those predicted by the two-temperature model.

The comparison of the simulations using the three-temperature models to the experimental data demonstrate that the these models accurately predict the thermochemical state of the fluid. However, the results were very similar to the legacy two-temperature model, which suggests that the physics of the forebody flow-field were accurately captured by the two-temperature model.

4.3 Wake Flow-Field

Temperature contour plots of the electron-electronic three-temperature model, highlighting the wake of the RAM C-II, are shown in Figure 30 and Figure 31 for the 61 km and 71 km trajectory points, respectively. Results using the free-electron model are not presented for the wake region because the electron temperature was indistinguishable from the vibrational temperature. The equilibration of the electron and vibrational energies in the wake for the free-electron model was due to both the strong coupling between the free-electron and vibrational energies and the small amount of energy within the free-electron manifold. This result was consistent with what was observed for the zero-dimensional simulation of the expansion case, Section 3.4.1.

The 61 km trajectory point, Figure 30, was characterized by a significant population inversion over a large region of the wake. The electron-electronic temperature was seen to be closely coupled to the vibrational temperature but had a larger region of greater temperature that persisted downstream. The wake-shock was apparent in the translational-rotational temperature where the streamlines abruptly changed direction and the temperature rose. However, the shock wave was too weak to directly

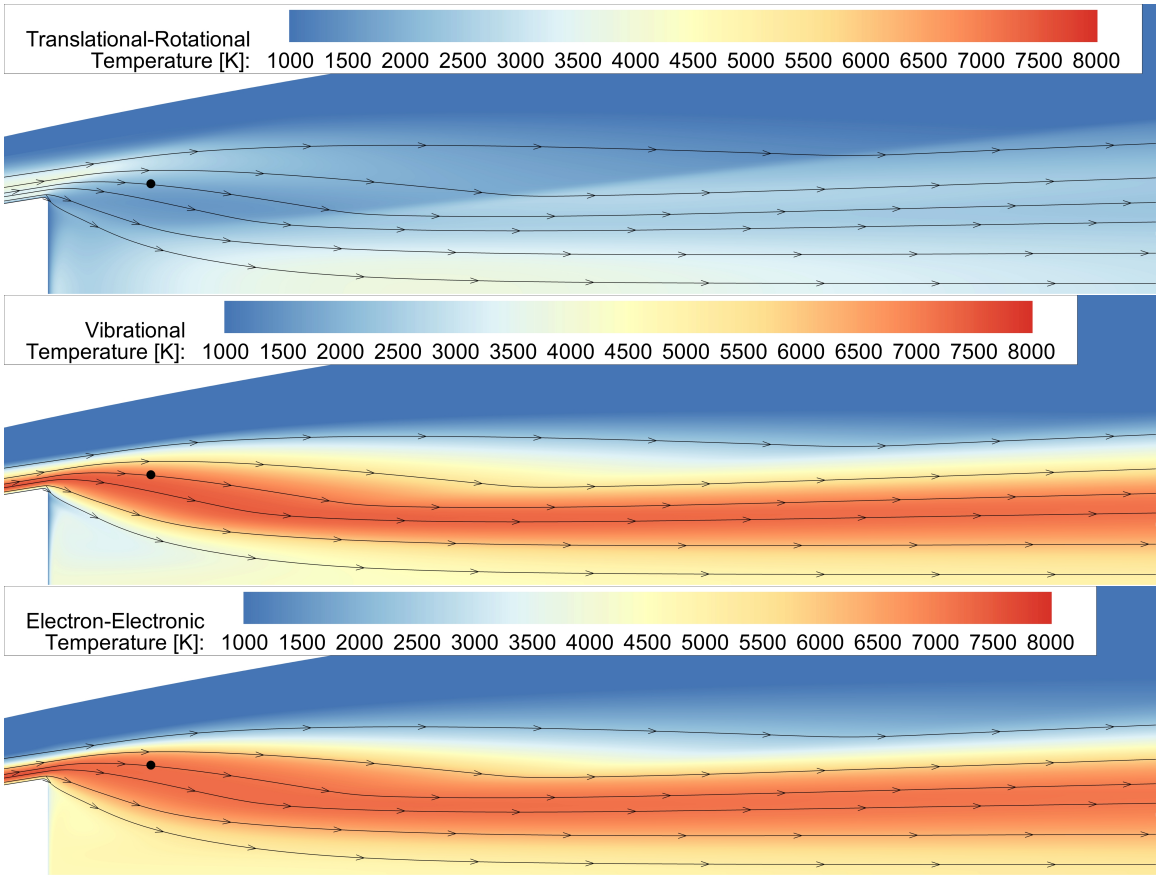

Figure 30. RAM C-II temperature contours for the 61 km trajectory point and electron-electronic three-temperature model.

affect the other energy modes.

The 71 km trajectory point contours, Figure 31, show different characteristics for the non-equilibrium state in the wake as compared to the 61 km point. As the fluid passed over the shoulder the three-energy manifolds were more closely equilibrated than the 61 km point. However, the electron-electronic temperature was greater than the other temperatures as it froze through the expansion zone and slowly equilibrated downstream. These temperature contours show, qualitatively, that the three-temperature model predicted a large region within the wake where the electron-electronic temperature was in a state of non-equilibrium with the other energy manifolds.

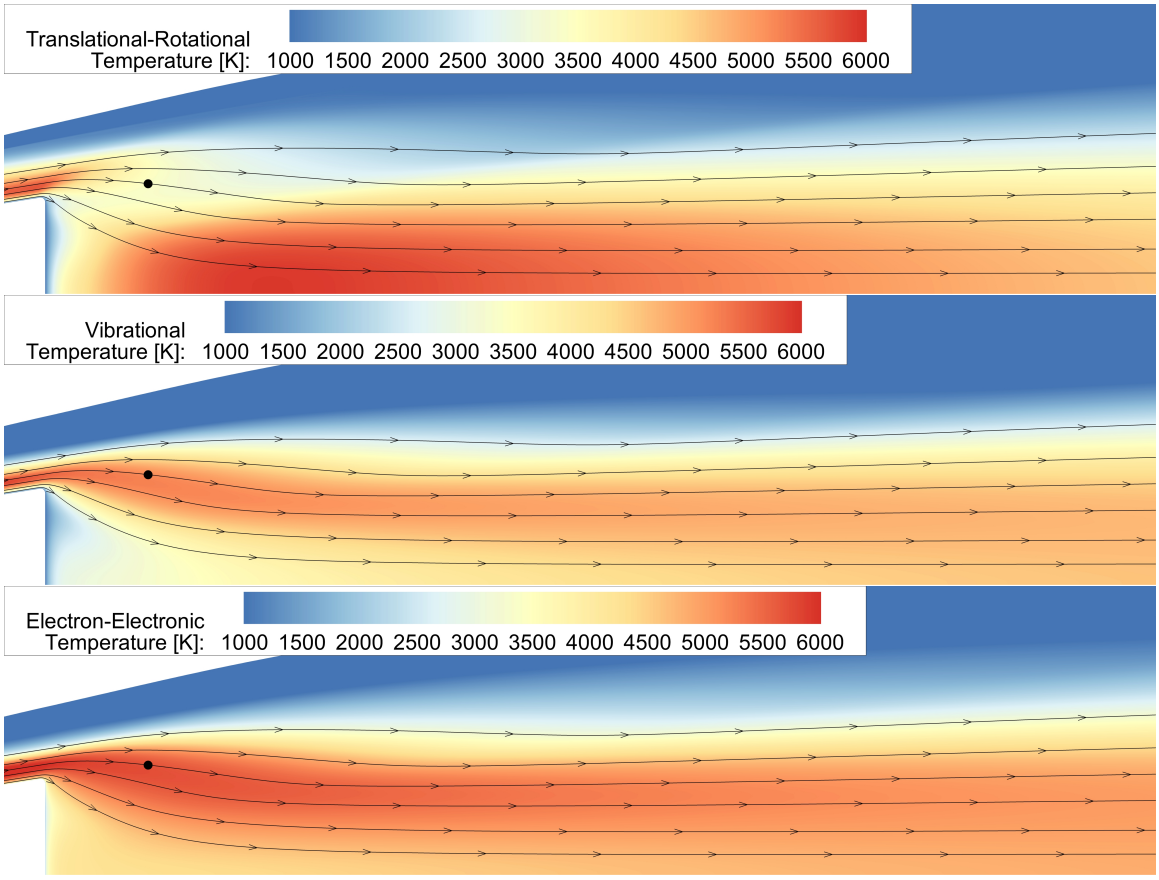

Figure 31. RAM C-II temperature contours for the 71 km trajectory point and electron-electronic three-temperature model.

The data along the streamlines annotated by a black dot in Figures 30 and 31 are presented in Figures 32 and 33 for the 61 km and 71 km trajectory points, respectively. The top sub-figures (32(a), 32(b), 33(a), and 33(b)) show the streamlines as they traversed over the forebody and the bottom sub-figures (32(c), 32(d), 33(c), and 33(d)) show the streamlines from the base of the vehicle to 30 body-lengths into the wake. Results using the two temperature model are also presented for comparison. Both trajectory points show that the electron-electronic energy was in a higher energy state than both the vibrational and translational-rotational temperature for the entire extent downstream.

Over the forebody of the 61 km trajectory point, Figures 32(a) and 32(b), the

translational-rotational temperature spiked as the fluid passed through the shock wave and then dropped considerably as the streamline expanded around the nose of the vehicle. The vibrational and electron-electronic temperatures were closely coupled throughout the forebody flow and both remained essentially frozen after the initial equilibration to the translational-rotational energy. As the streamline entered the wake, Figures 32(c) and 32(d), the translational-rotational temperature dropped further, to below $2,000\,\mathrm{K}$, before passing through the wake-shock, $X/L \approx 1$, where the temperature slightly rose. The vibrational temperature exhibited a slight decrease through the expansion over the vehicle shoulder due the exchange process with the translational energy. However, as the density dropped, the vibrational and electron-electronic temperatures froze before slowly equilibrating with the translational-rotational manifold.

The streamline along the forebody for the 71 km trajectory point, Figures 33(a) and 33(b), shows that the energy modes equilibrated to a greater extent than the 61 km point as the fluid moved towards the vehicle base. Additionally, after the fluid passed through the wake-shock the translational temperature continually decreased downstream, where the 61 km point showed the translational-rotational temperature rising downstream. The electron-electronic temperature was again observed to be the highest temperature throughout the wake.

Continuing far downstream into the wake for the 61 km and 71 km trajectory points, both the two-temperature and three-temperature models predicted a large region of non-equilibrium and thermal inversion. The electron-electronic energy, given by the three-temperature model, was predicted to equilibrate more slowly than the vibrational energy and remain in an excited state throughout the wake.

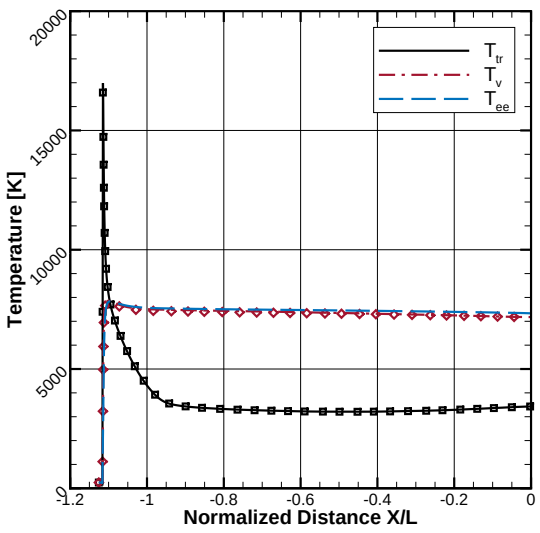

(a) Forebody temperatures.

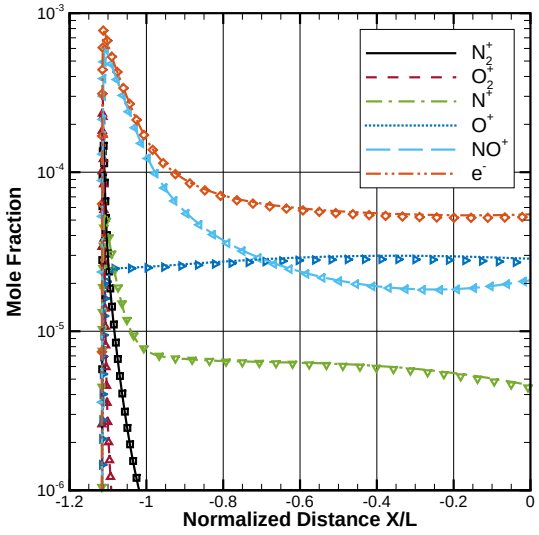

(b) Forebody charged species.

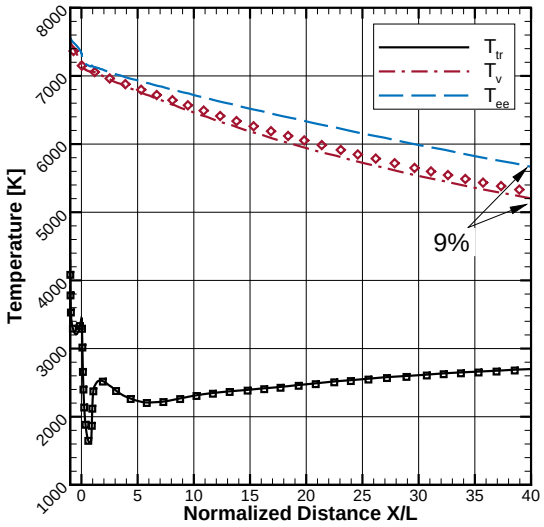

(c) Wake temperatures. ■ = T_{tr} ♦ = T_{vee}

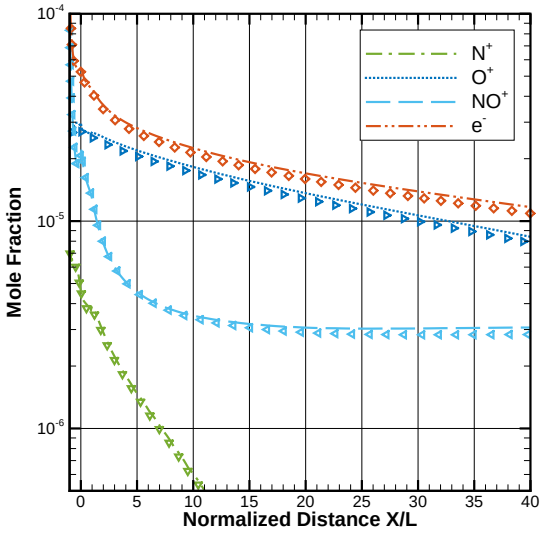

(d) Wake charged species. ■ = N_2^+ ▲ = O_2^+ ▼ = N^+ ►= O^+ ◄= NO^+ ♦ = e^-

Figure 32. RAM C-II 61 km wake streamline using the electron-electronic three-temperature model. $X/L = 0$ is the base of vehicle where L is the vehicle length. Symbols are results from the two-temperature model.

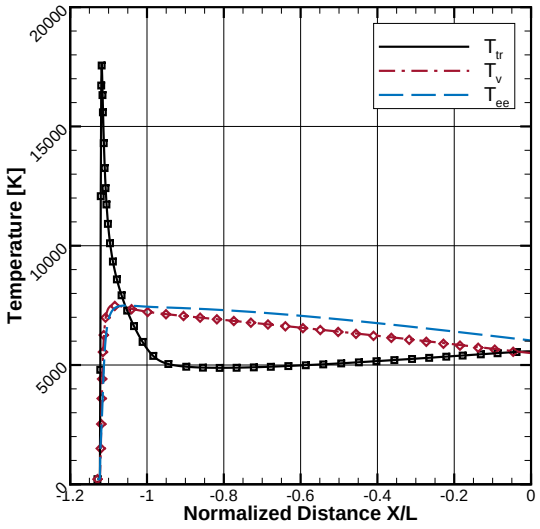

(a) Forebody temperatures.

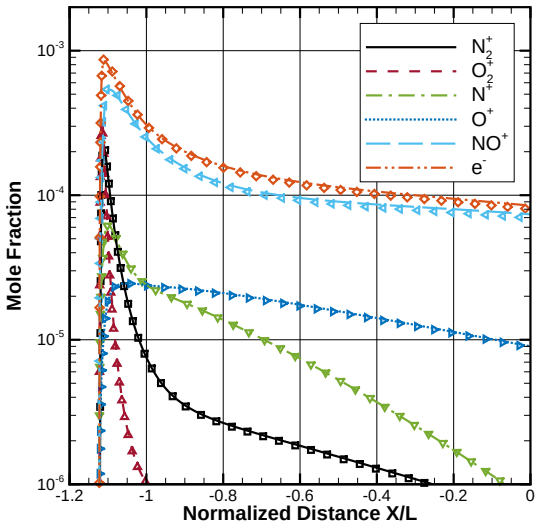

(b) Forebody charged species.

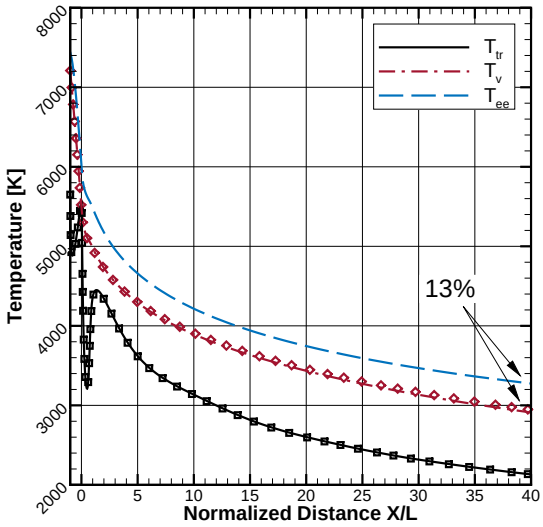

(c) Wake temperatures. ■ = T_{tr} ♦ = T_{vee}

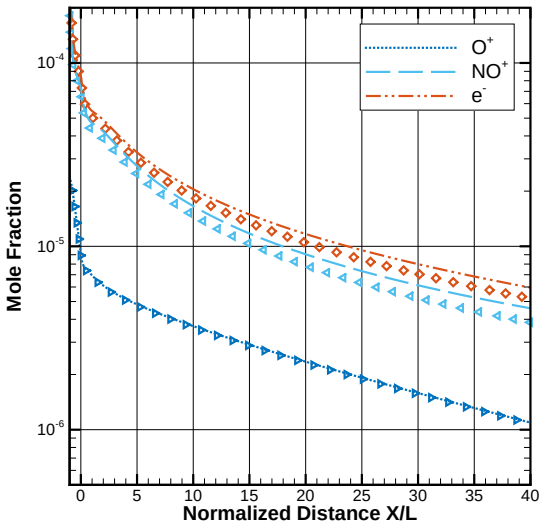

(d) Wake charged species. ■ = N_2^+ ▲ = O_2^+ ▼ = N^+ ►= O^+ ◄= NO^+ ♦ = e^-

Figure 33. RAM C-II 71 km wake streamline using the electron-electronic three-temperature model. $X/L = 0$ is the base of vehicle where L is the vehicle length. Symbols are results from the two-temperature model.

4.4 Diffusion Modeling

The previous RAM C-II simulations were all conducted using the approximate diffusion model as given by Equation (85). The validity of this approximation was investigated by utilizing two additional higher-fidelity diffusion models in conjunction with the electron-electronic three-temperature model. The approximate diffusion (AD) model provides a direct relation for the diffusion velocity based on the mole fraction gradient. The second model, termed the multicomponent diffusion (MD) model, utilizes the Stefan-Maxwell equations to iteratively solve for the diffusion velocities; this particular implementation neglected thermal and pressure diffusion effects. The third model, the multi-temperature multicomponent diffusion (MMD) model directly accounts for the electric field and separate electron temperature within the Stefan-Maxwell equations; additionally, pressure diffusion is included in this model. The details of these models are presented in Section 2.12.1, and the final form of the equations are repeated for convenience:

- Approximate diffusion (AD) [29, 101]:

$$V_s^i = -a_s \left(\sum_{r \neq s} \frac{X_r}{\mathscr{D}_{sr}} \right)^{-1} \frac{1 - c_s}{X_s} \frac{\partial X_s}{\partial x^i} \quad (a_{ion} = 2) \tag{126}$$

- Multicomponent diffusion (MD) [29, 101]:

$$V_s^i = a_s \left(\sum_{r \neq s} \frac{X_r}{\mathscr{D}_{sr}} \right)^{-1} \left[-\frac{1}{X_s} \frac{\partial X_s}{\partial x^i} + \sum_{r \neq s} \frac{X_r}{\mathscr{D}_{sr}} V_r^i \right] \quad (a_{ion} = 1 + \frac{T_e}{T_t}) \tag{127}$$

- Multi-temperature multicomponent diffusion (MMD) [92, 93]:

$$V_s^i = \left(\sum_{r \neq s} \frac{z_r}{\mathscr{D}_{sr}} \right)^{-1} \left[-\frac{1}{z_s} \frac{\partial z_s}{\partial x^i} - \frac{z_s - c_s}{z_s} \frac{\partial \ln p}{\partial x^i} + \frac{n_s \mathsf{e} Z_s}{z_s p} \mathsf{E}^i + \sum_{r \neq s} \frac{z_r}{\mathscr{D}_{sr}} V_r^i \right] \tag{128}$$

Figure 34 presents the comparison of the electron number-density along the fore-body to the experimental data for the three diffusion models. The two higher-fidelity models, MD and MMD, improved the agreement of the simulation to the experimental data for both the 61 km and 71 km trajectory points. However, the MMD model was largely indistinguishable from the MD model suggesting that the direct consideration of a separate electron temperature, electric field model, and pressure diffusion within the Stefan-Maxwell equations did not significantly contribute to the diffusion velocities for these conditions.

The temperatures and species concentrations along the stagnation streamline for the 61 km trajectory point are presented in Figure 35 for the MD and MMD models compared to the AD model. Figure 36 similarly presents the stagnation streamlines for the 71 km trajectory point. The MD and MMD model were again shown to be very similar to each other and exhibited the largest differences from the AD

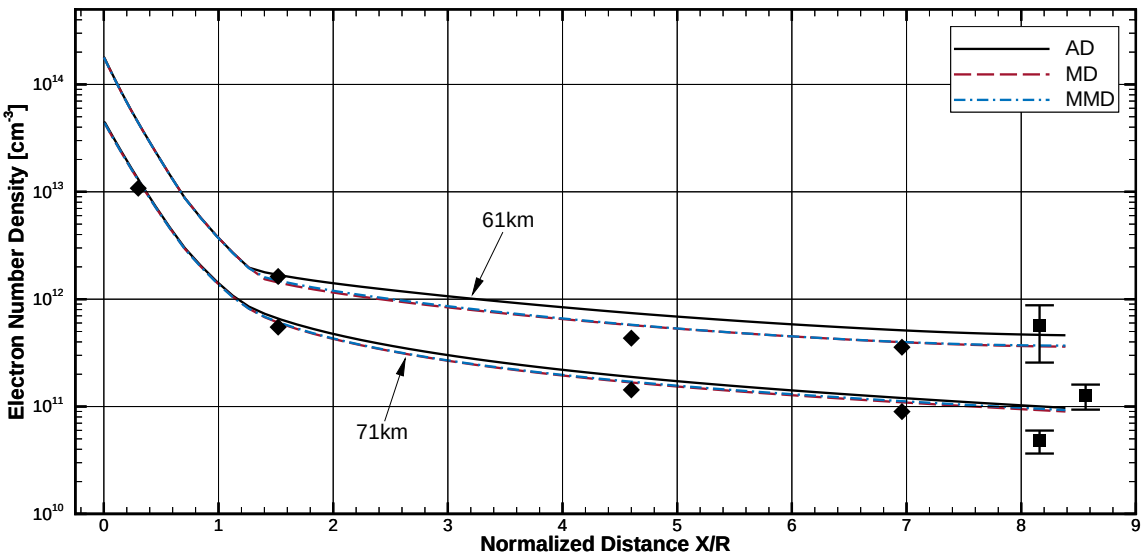

Figure 34. RAM C-II simulations comparing diffusion models and experimental data; maximum electron number density, normal to the surface, as a function of distance axially from the nose. Experimental data from Jones *et al.* [55]: ♦ = average reflectometer measurements, ■ = electrostatic probe measurements where the error bars represent the peak-to-peak variation.

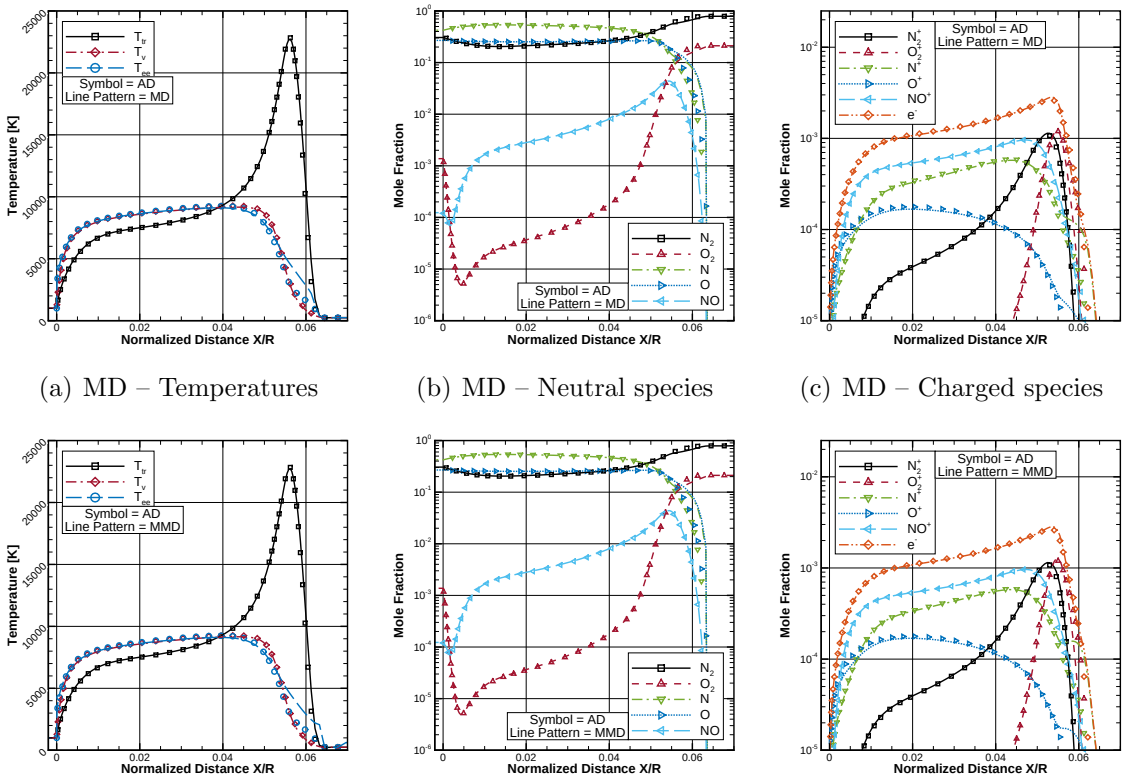

(a) MD – Temperatures (b) MD – Neutral species (c) MD – Charged species

(d) MMD – Temperatures (e) MMD – Neutral species (f) MMD – Charged species

Figure 35. RAM C-II 61 km stagnation streamline comparing diffusion models..

model in the vicinity of the shock wave. The higher-fidelity models predicted higher concentrations of the monatomic species and lower concentrations of the diatomic species immediately behind the shock. The diffusion of the high-energy monatomic species upstream, towards the shock wave, caused this discrepancy as well as increasing the energy content within the electron-electronic energy manifold. Therefore, the electron-electronic temperature was higher immediately post-shock for the MD and MMD models compared to the AD model.

The data along the streamlines from the forebody into the wake are presented in Figures 37 and 38 for the 61 km case for the MD and MMD models, respectively. Along the forebody, Figures 37(a)-37(c) and 38(a)-38(c), results between the three models were in good agreement, except for in the vicinity of the shock wave as pre-

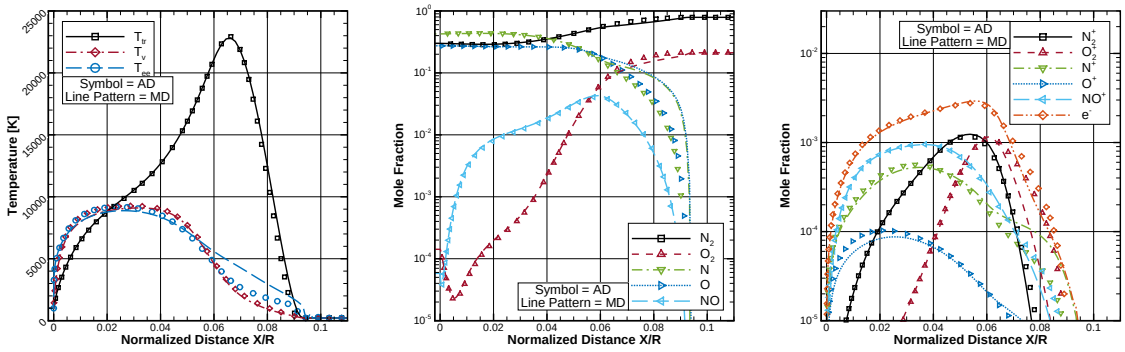

(a) MD – Temperatures (b) MD – Neutral species (c) MD – Charged species

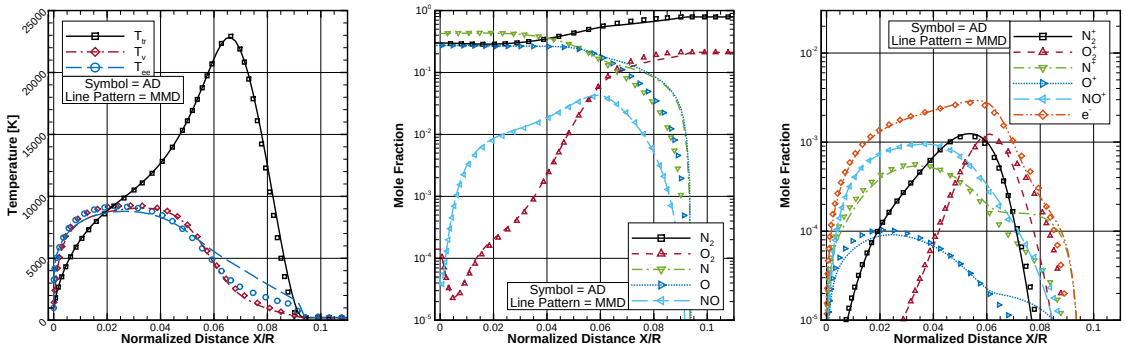

(d) MMD – Temperatures (e) MMD – Neutral species (f) MMD – Charged species

Figure 36. RAM C-II 71 km stagnation streamline comparing diffusion models..

viously detailed along the stagnation streamline. Considering streamlines within the wake, Figures 37(d)-37(f) and 38(d)-38(f), both of the higher-fidelity MD and MMD models predicted lower levels of ionization stemming from the steep decrease these models predicted for the concentration of O^+ through the expansion region. The vibrational and electron-electronic modes were predicted to have slightly less energy with the MD and MMD models as compared to the AD model and their respective temperatures remained closer in value with the higher-fidelity models for the first few body lengths downstream. The MMD model predicted the vibrational and electron-electronic energies to be equilibrated for approximately 6 body lengths into the wake, at which point the electron-electronic temperature froze and remained at a higher level for the remainder of the domain.

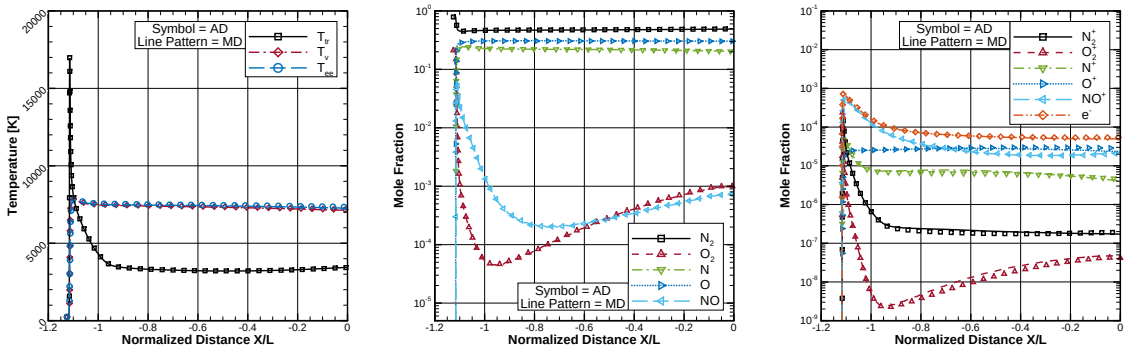

(a) Forebody temperatures (b) Forebody neutral species (c) Forebody charged species

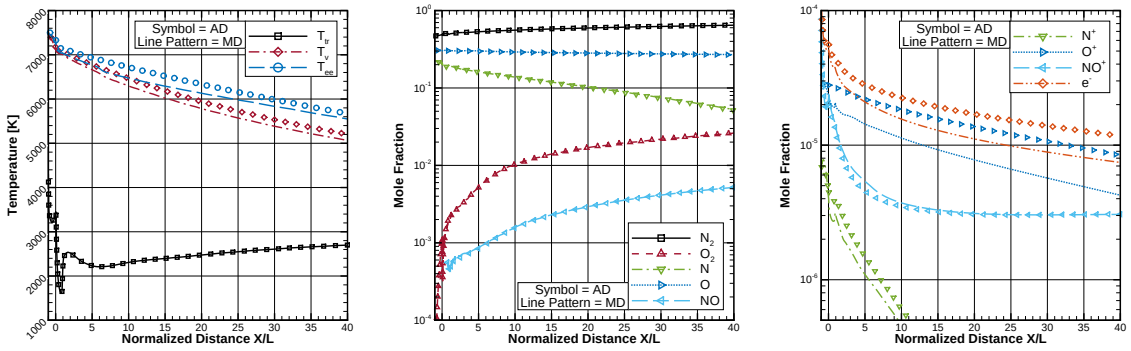

(d) Wake temperatures (e) Wake neutral species (f) Wake charged species

Figure 37. RAM C-II 61 km wake streamline using the the multicomponent diffusion model. $X/L = 0$ is the base of vehicle where L is the vehicle length.

Figures 39 and 40 present the data along the streamlines of the MD and MMD models for the 71 km case. The forebody data, Figures 39(a)-39(c) and 40(a)-40(c), show that the MD and MMD models predicted the vibrational and electron-electronic modes to be equilibrated as the fluid moves over the nose towards the base of the vehicle. The difference in the species concentrations between the higher-fidelity models and the AD model was most noticeable in O^+, where the MD and MMD models predicted a lower value than the AD model throughout the majority of the domain. As the streamlines passed into the wake, Figures 39(d)-39(f) and 40(d)-40(f), similar trends as those detailed for the 61 km trajectory point were observed. However, because the dominant ionic species was NO^+, which wasn't greatly affected by diffusion model, the levels of ionization were only slightly less for the higher-fidelity models.

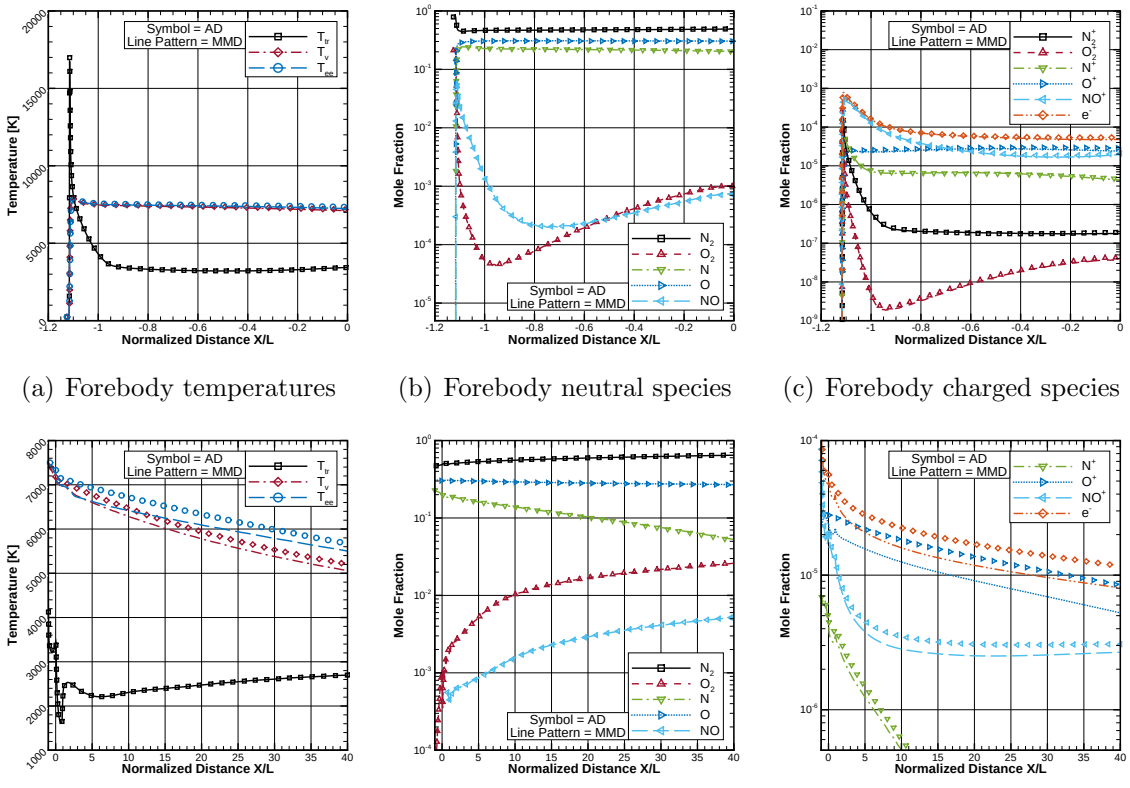

(a) Forebody temperatures (b) Forebody neutral species (c) Forebody charged species

(d) Wake temperatures (e) Wake neutral species (f) Wake charged species

Figure 38. RAM C-II 61 km wake streamline using the the multi-temperature multicomponent diffusion model. $X/L = 0$ is the base of vehicle where L is the vehicle length.

The MD and MMD models increased the fidelity of the simulations, as shown by the comparison with the experimental data in Figure 34. However, the additional consideration of pressure diffusion and directly accounting for the electric field within the Stefan-Maxwell equations, as is done in the MMD model, did not contribute significantly to increasing the accuracy of overall solution above that which was offered by the simpler MD model.

4.5 RAM C-II Conclusions

The three-temperature models, developed in Chapter II, were implemented within the FUN3D software architecture and validated against the RAM C-II experimental

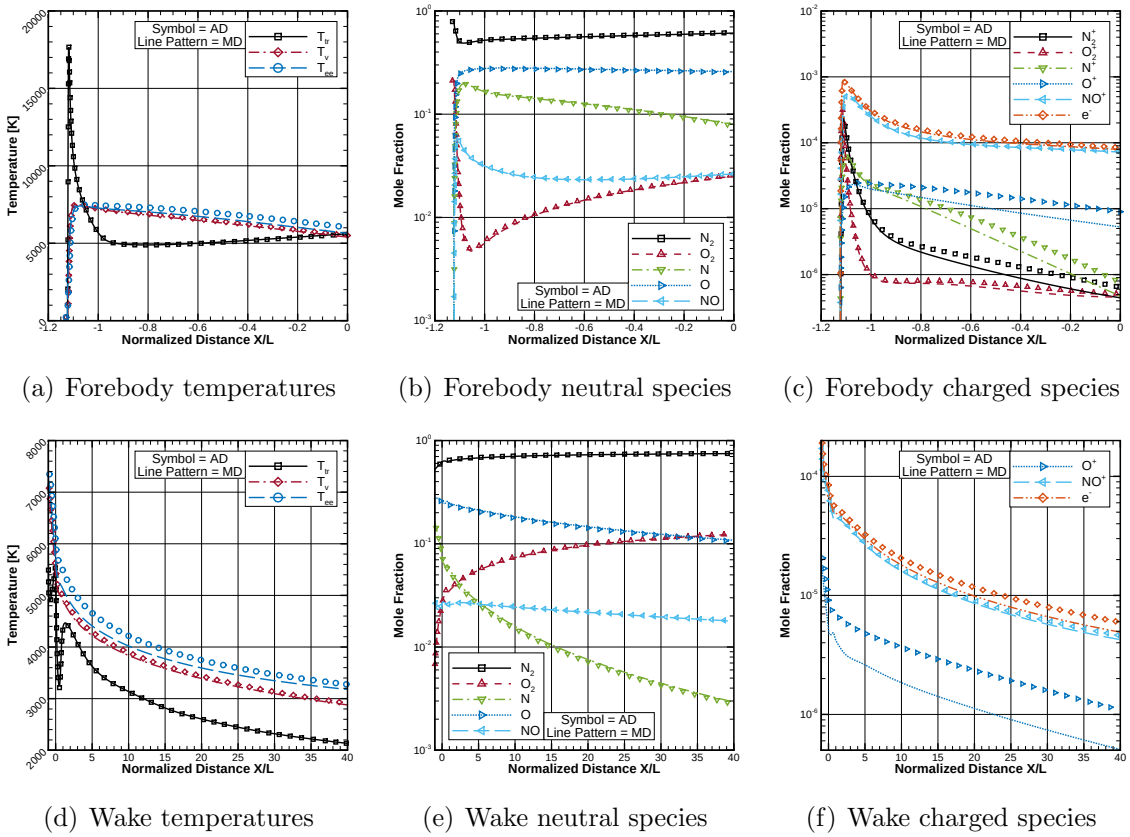

(a) Forebody temperatures (b) Forebody neutral species (c) Forebody charged species

(d) Wake temperatures (e) Wake neutral species (f) Wake charged species

Figure 39. RAM C-II 71 km wake streamline using the the multicomponent diffusion model. $X/L = 0$ is the base of vehicle where L is the vehicle length.

data. The computed electron number-densities over the forebody compared well with the flight test data for both three-temperature models. The simulations were then continued far downstream of the vehicle to investigate the non-equilibrium phenomena that the three-temperature models predict within the wake region. The results were then compared to those obtained using the legacy two-temperature model.

The free-electron three-temperature model remained in close thermal equilibrium with the vibrational energy throughout the domain resulting in the flow-field quantities being essentially the same as those predicted by the two-temperature model. Therefore, the ability of the free-electron model to capture additional physics above the two-temperature model may be limited.

The electron-electronic three-temperature model, which groups together the free-

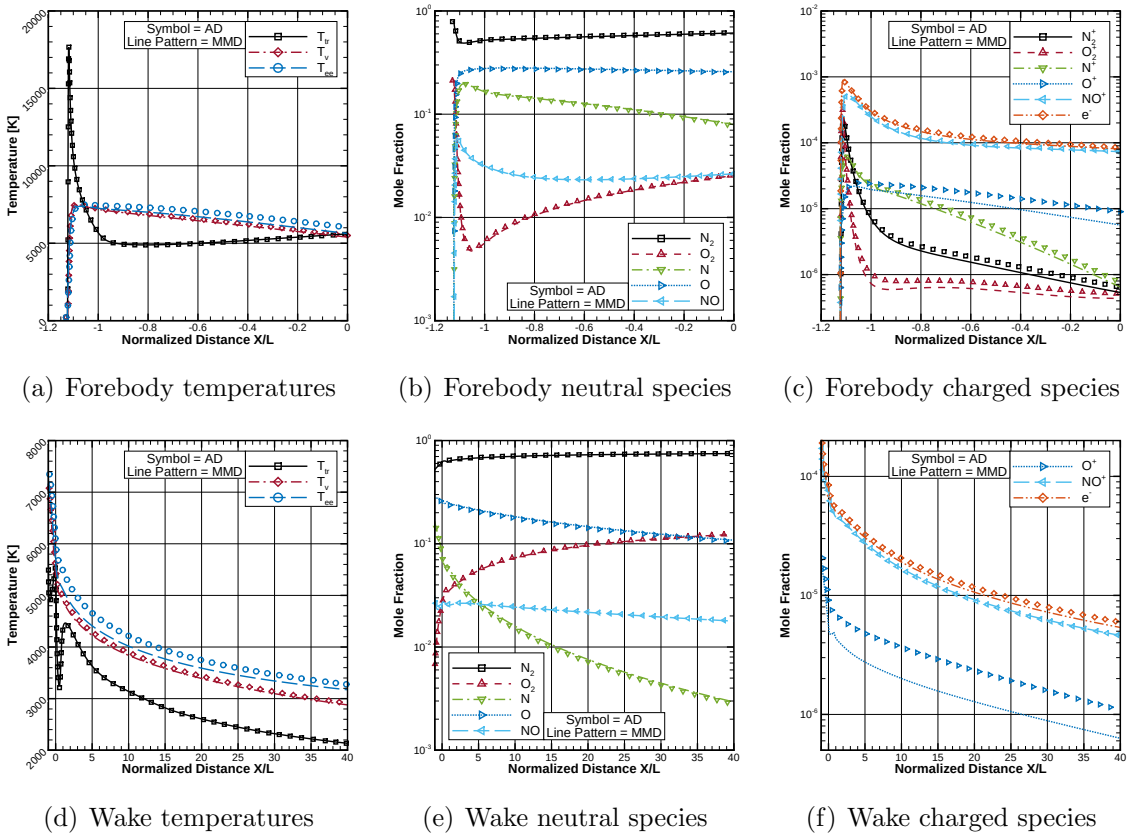

(a) Forebody temperatures (b) Forebody neutral species (c) Forebody charged species

(d) Wake temperatures (e) Wake neutral species (f) Wake charged species

Figure 40. RAM C-II 71 km wake streamline using the the multi-temperature multicomponent diffusion model. $X/L = 0$ is the base of vehicle where L is the vehicle length.

electron translational energy and electronic energy of the constituent species, was slower to equilibrate to the vibrational temperature compared to the free-electron model. Within the wake, the translational-rotational and vibrational temperatures agreed well with those predicted by the two-temperature model, but the electron-electronic energy was in a state of non-equilibrium with the other modes. The behavior of the electron-electronic model agreed with expectations throughout the flowfield, thus capturing additional physics above the two-temperature model. Therefore, for wake flows, the use of a three-temperature model, such as the electron-electronic model, may be necessary to accurately predict the thermochemical state of the fluid.

Lastly, three diffusion models were investigated in conjunction with the electron-

electronic three-temperature model. The detailed diffusion velocities obtained by means of the Stefan-Maxwell equations increased the solution fidelity and resulted in better agreement to the RAM C-II flight test data. Pressure diffusion as well as directly accounting for the electric field and the multi-temperature nature of the gas model, as is done in the MMD model, were, for the trajectory points considered, shown to not be significant contributors to the overall thermochemical state of the fluid. However, there may exist more complicated flow-fields where the differences between the MD and MMD models are more severe and the higher fidelity MMD may be necessary to predict more accurate diffusion velocities.

V. Wake Flow-Field behind a Cone at Angle of Attack

Flow-fields around slender, hypersonic vehicles are of prime importance to DoD interests. However, studies concerning the wake behind these vehicles, where many exploitative features exist, are scarce. To address this gap, a parametric study, varying altitude and angle of attack, characterizing the wake behind a slender cone geometry was completed. Of particular interest in completing this investigation was the performance of the electron-electronic three-temperature model within the wake, where a population inversion was expected and the thermochemical state of the complex wake structure would benefit from a high-fidelity three-temperature model.

Slender-vehicle geometry is of particular interest for military applications where the objectives are to maximize speed and range; therefore, a slender, low-drag configuration is ideal as compared to a blunt, reentry-type capsule. A simple cone geometry, as detailed in Figure 41, was considered in this study: 0.05 m spherically-blunted nose, 6 degree half-angle cone, 1.0 m base diameter, and an overall length of approximately 4.33 m. The freestream conditions for the eight cases that were considered are presented in Table 7. A velocity of $5\,\mathrm{km\,s^{-1}}$ was considered for all cases while the altitude was varied between 40 km and 50 km and angle of attack (α) varied from 0 degrees to 30 degrees. The velocity was chosen to remain constant to reduce the number of computational grids that needed to be created. Since the Mach number for all cases was relatively similar, the grid could be aligned to the shock wave for one

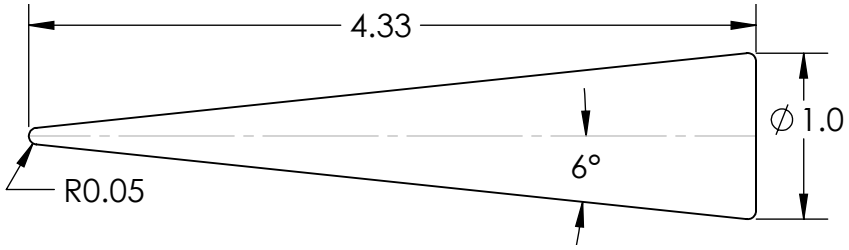

Figure 41. Wake investigation cone geometry; units are in meters.

Table 7. Wake Investigation Cases

Case	AoA (α) [deg]	Altitude [km]	Density [$\mathrm{kg\,m^{-3}}$]	Mach Number	Reynolds Number†
1	0	40	3.851×10^{-3}	15.7	1.19×10^{6}
2	10				
3	20				
4	30				
5	0	50	9.775×10^{-4}	15.2	2.84×10^{5}
6	10				
7	20				
8	30				

* The freestream velocity for all cases is $V_{\infty} = 5\,\mathrm{km/s}$
† Reynolds number is based on cone base diamter, 1 m

altitude and each angle of attack and then utilized for the second altitude without having to realign to the shock wave.

A seven-species air model was utilized, and turbulence was modeled by a compressible from of the Spalart-Allmaras turbulence model [98, 99] developed by Catris and Aupoix [26]. Since the thrust of this study was not towards the turbulent nature of the wake, the Spalart-Allmaras model was chosen for its simplicity and general acceptance. Diffusion velocities were calculated via the Stefan-Maxwell equations developed by Ramshaw and Chang [92, 93] for a multi-temperature ambipolar plasma, Equation (72), termed the MMD model within Chapter IV. Lastly, the vibrational-electron energy relaxation time of Lee [64] was utilized.

The vehicle surface was modeled to be in a state of radiative equilibrium with the convective heat flux [4]. The surface temperature was found, assuming a gray-body, by

$$\left|q^{i}\right|_{wall} = \bar{\epsilon}\sigma T^{4}, \tag{129}$$

where the surface emissivity, ϵ, was assumed to be 0.89 and σ is the Stefan-Boltzmann

constant. Additionally, the vehicle surface was assumed to be non-catalytic to neutral species and fully catalytic to ionic species.

5.1 Grid Generation and Convergence

A multi-block, structured grid utilized that was highly aligned to the shock wave over the entirety of the domain. Only half the domain was modeled, which took advantage of flow symmetry along the lateral axis. A structured grid was employed since, for hypersonic simulations, alignment with the bow shock wave is greatly advantageous to flow-field solution quality [22]. The domain was extended 20 base-diameters into the wake for each case, and the grid was refined in the near wake region to sufficiently capture important flow features. Four grids, one for each angle of attack, were constructed which were all based on the same topological structure. The shock-surface was obtained after six iterations of grid generation for the 40 km cases. The same grid was then utilized for the 50 km cases because the freestream Mach number did not vary much between the two altitudes and the shock-wave position was not expected to differ significantly. The grid topology consisted of 4,852 blocks for each grid; Figure 42 shows the complexity of the topology as well as the attention paid to the refinement within the wake region.

A grid convergence study was completed for Case 4, $\alpha = 30$ degrees and 40 km altitude, using the two-temperature model with three grid refinement levels. Case 4 was expected to exhibit the largest and most complex wake structure as well as the steepest gradients in the flow-field variables due to the higher Reynolds number of the initial conditions. Therefore, it was reasoned that if grid convergence was demonstrated for this case the same topology could be transfered to the other cases with confidence that grid independence could be assumed. Additionally, considering the results obtained in Chapter IV that showed that grid independence was obtained

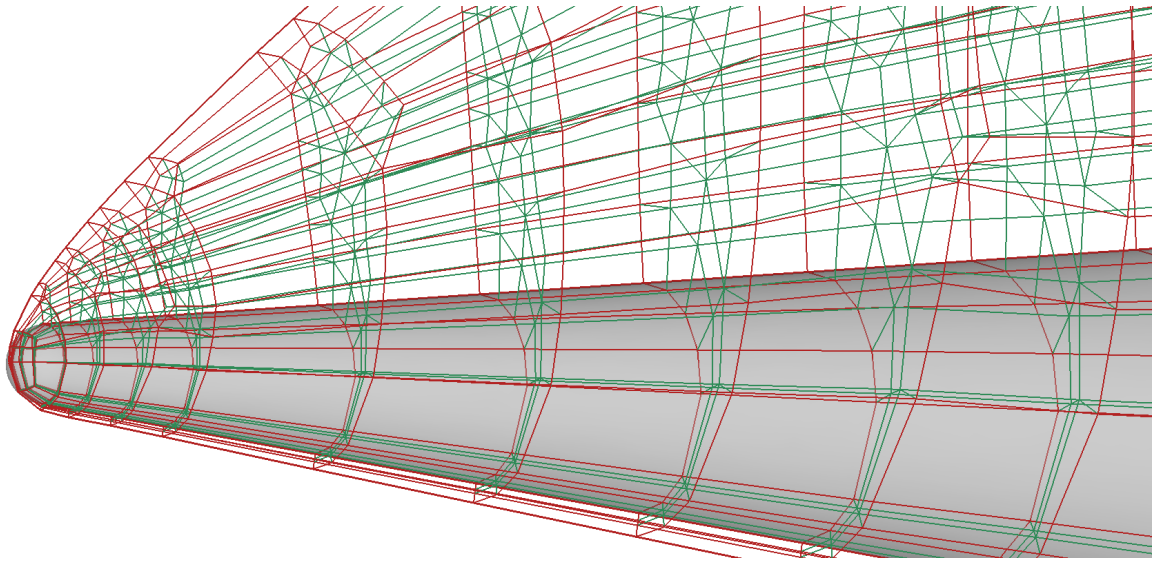

(a) Nose detail.

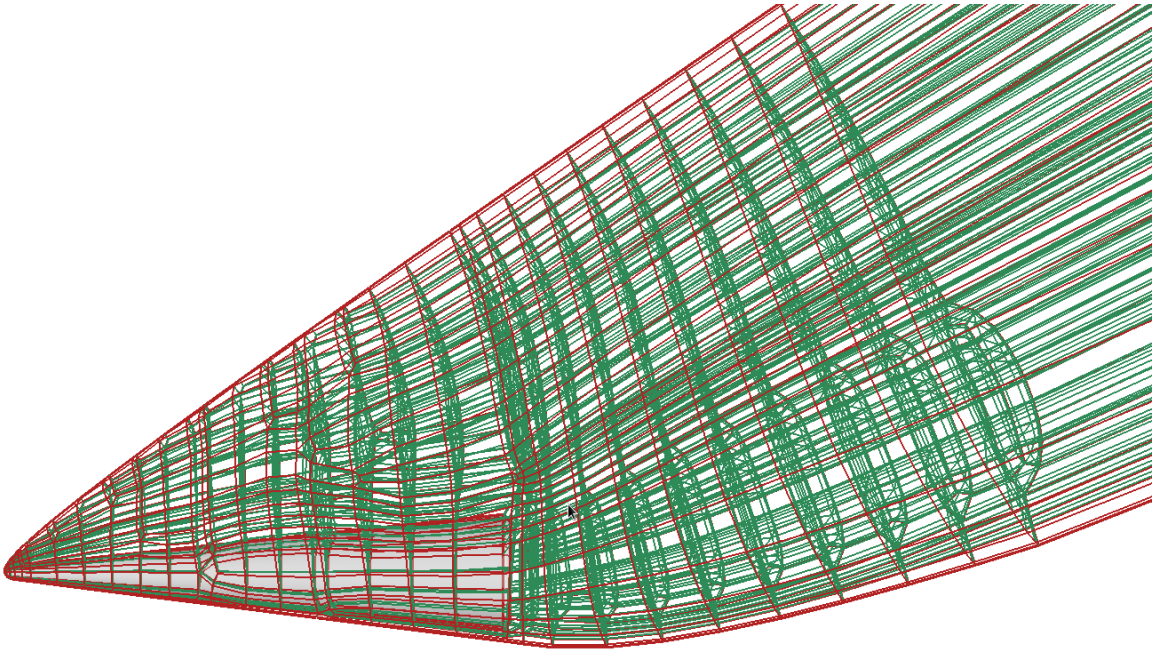

(b) Full domain.

Figure 42. Wake investigation grid topology for the 30 degree angle of attack grid.

at the same refinement level for the two-temperature and three-temperature models, the lower computationally-expensive two-temperature model was utilized. The coarse grid had 14,295,385 nodes, the medium grid had 24,580,959 nodes, and the fine grid had 42,281,069 nodes. The total electron-count within the domain was chosen as the prime figure for determining grid convergence due to the sensitivity of the thermo-chemical state to the electron number-density. Figure 43(a) presents the total number of free-electrons within the domain for each of the grid resolutions; from the coarse to the medium grid there was a 14% drop in the number of electrons and less than 1% change from the medium to the fine which indicated that the medium resolution grid was sufficiently resolved for a grid independent solution.

Additional figures were explored including integrated surface quantities and data along selected streamlines throughout the domain. Figure 43(b) presents the total surface heat flux and coefficients of lift and drag for all three grid resolutions. Again, the medium resolution grid was determined to be sufficiently resolved. The surface tem-

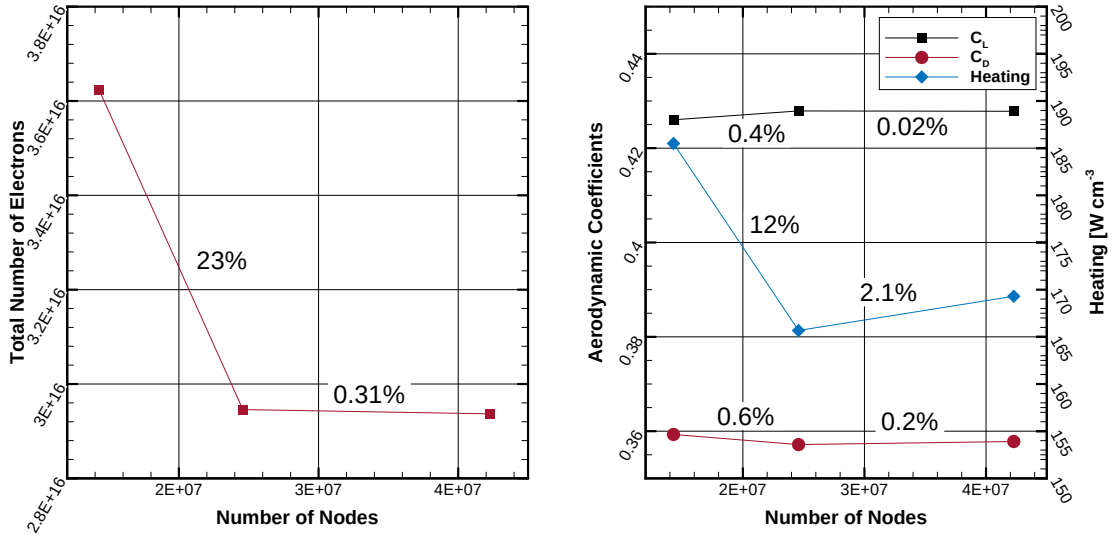

(a) Total number of electrons within the solution domain.

(b) Vehicle surface quantities.

Figure 43. Wake investigation grid convergence: total electron count and surface quantities.

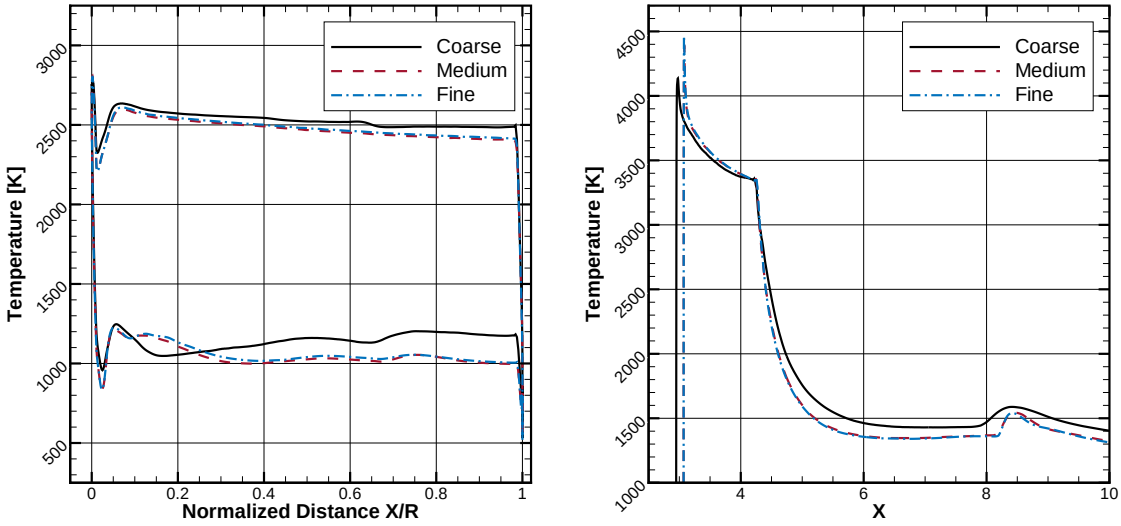

(a) Vehicle surface temperature along symmetry plane.

(b) Translational-rotational temperature along selected streamline.

Figure 44. Wake investigation grid convergence: surface and streamline temperatures.

perature along the symmetry plane, presented in Figure 44(a), reinforced the previous conclusion based on the heat flux. Lastly, Figure 44(b) presents the translational-rotational temperature along a streamline on the symmetry plane which traversed the windward side under the vehicle and into the wake. The medium and fine grids showed little variation between their predicted temperatures throughout the domain, demonstrating that the medium resolution grid was sufficiently resolved. Additional streamlines as well as vibrational temperature, density, pressure, and species concentrations were examined for convergence; the same conclusion was reached in each case.

5.2 Stagnation Streamline

The complexity of the thermochemical state of flow-field around hypersonic vehicles begins by the fluid traversing the shock wave, especially the strong shock near the stagnation streamline. By ensuring that the processes along the stagnation stream-

line are physically explainable for the three-temperature model, the confidence in the flow-field solution throughout the domain is increased. Therefore, Figures 45 and 46 present temperatures and species concentrations along the stagnation streamline for the 40 km and 50 km conditions, respectively. Results using the two-temperature model are also presented for comparison.

Consistent with expectations, the electron-electronic temperature was the last to equilibrate for both altitudes. The 50 km case was slower to respond, due to the lower density, to the post-shock non-equilibrium potential. For both altitudes, the low electron temperature post shock resulted in a slight decrease in the prediction of the NO^+ and e^- species during the equilibration process of the three-temperature model compared to the two-temperature model. This mechanism was observed in the zero-dimensional simulations of Chapter III and the RAM C-II simulations of Chapter IV. These results suggest that the three-temperature model captured additional physics, compared to the two-temperature model, through the bow shock wave. Along the fore-body, especially in the nose region, the increased fidelity from the separate electron-electronic mode would alter radiative heating predictions. For the cases considered here, the $5\,\mathrm{km\,s^{-1}}$ velocity was generally to low for radiative heating along the fore-body to be significant. However, for higher velocity simulations, the significance of radiation to the fore-body would increase and the three-temperature model would be more advantageous.

The stagnation streamline results also serve as a first verification for the use the same grid for both altitudes since the position of the shock waves were similar between the 40 km and 50 km cases. The location of the peak translational-rotational temperatures differed by approximately $0.01R$ which demonstrated the applicability of the grid, that was carefully aligned to the 40 km case, to the 50 km conditions.

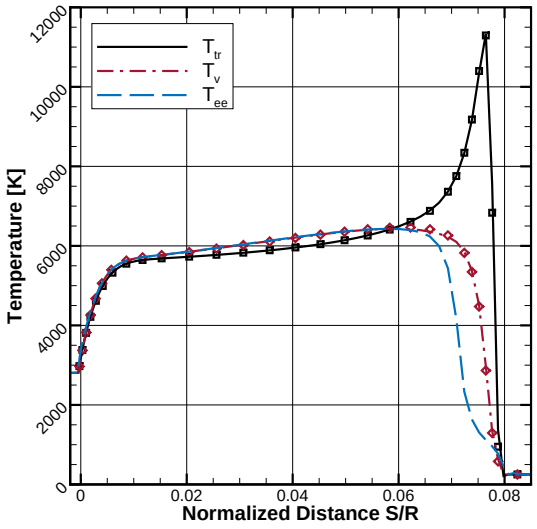

(a) Temperatures. ■ $= T_{tr}$ ♦ $= T_{vee}$

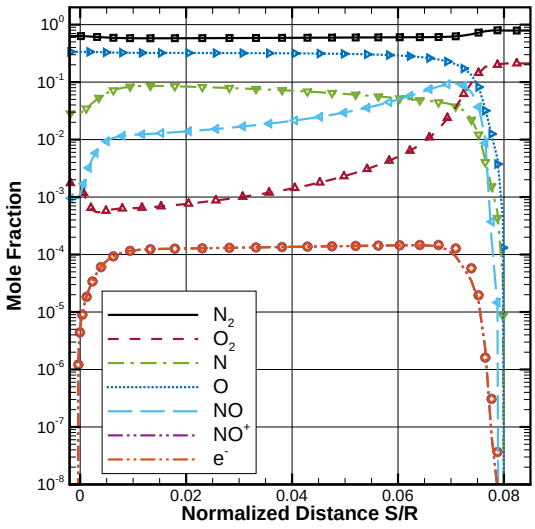

(b) Species concentrations. ■ $= N_2$ ▲ $= O_2$ ▼ $= N$ ►$= O$ ◄$= NO$ ● $= NO^+$ ♦ $= e^-$

Figure 45. Wake investigation 40 km stagnation streamline. The horizontal axis is the distance normal to the surface, *S*, normalized by the nose radius, *R*. Symbols are data from the two-temperature model.

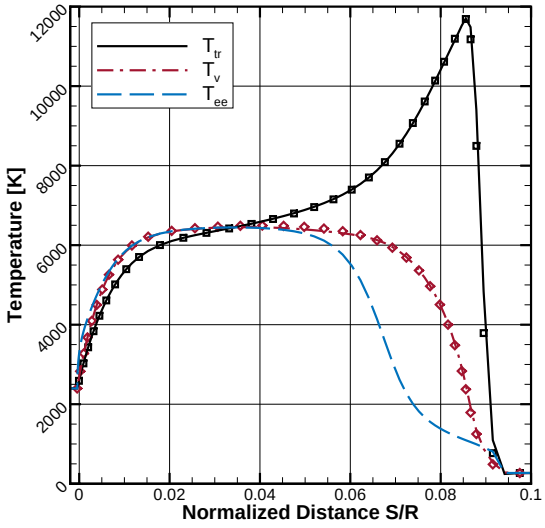

(a) Temperatures. ■ $= T_{tr}$ ♦ $= T_{vee}$

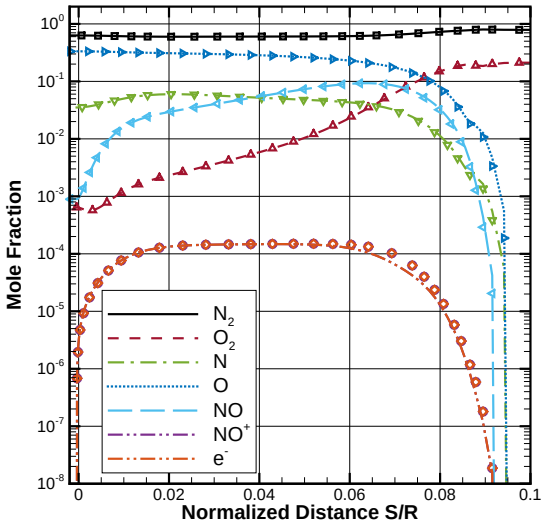

(b) Species concentrations. ■ $= N_2$ ▲ $= O_2$ ▼ $= N$ ►$= O$ ◄$= NO$ ● $= NO^+$ ♦ $= e^-$

Figure 46. Wake investigation 50 km stagnation streamline. The horizontal axis is the distance normal to the surface, *S*, normalized by the nose radius, *R*. Symbols are results from the two-temperature model.

5.3 Wake Characteristics

The wake behind the slender, cone geometry was a complex structure of recirculation zones, stagnation regions, and shock waves. Figure 47 presents Mach number contour plots along the symmetry plane and selected cross-sectional slices for all eight cases to highlight the main flow features. Immediately evident was that the complexity of the wake structure increased with angle of attack as the vehicle became more blunt to the freestream: the overall cross-sectional size of the wake increased, the Mach number within the wake generally decreased, and the location of the wake stagnation point and shock waves rotated toward the leeward side.

Also evident in the Mach contour plots was the formation of a vortex along the leeward side for cases with an angle of attack greater than zero. Fluid from the windward side, that originated near the stagnation streamline, flowed over the nose toward the leeward side and coalesced into a vortex that traversed the leeward side eventually collapsing into the wake stagnation and compression zones. Additionally, fluid along the windward side traversed the bow shock wave and rotated around the body and separated as it entered the leeward side finally coalescing into the leeward vortex. The location of this vortex is apparent in the streamlines, in particular the streamline immediately above the leeward edge of the vehicle. Interestingly, the size and location of the nose tip vortex remained essentially unchanged with increasing angle of attack.

The Mach contour plots also hint that the wake could be split into two separate regions: the first was that originating form the leeward side and made up the upper half of the wake which was characterized by lower Mach number flows, the second was the lower half of the wake whose fluid originated from the windward side and traversed under the vehicle into the wake and was characterized by higher Mach numbers. The line of separation between these two zones was the core flow which originated at the

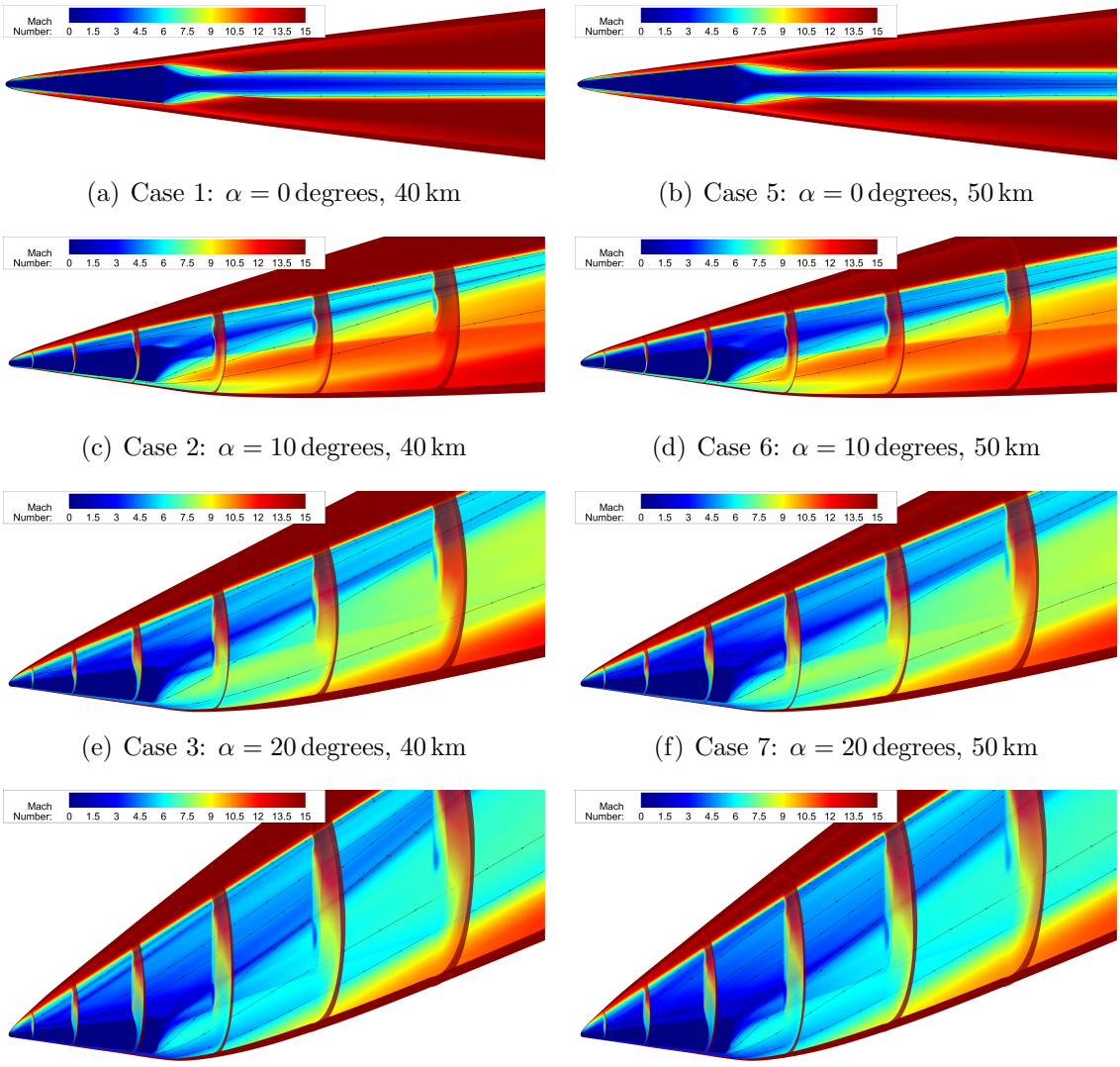

(a) Case 1: $\alpha = 0$ degrees, 40 km

(b) Case 5: $\alpha = 0$ degrees, 50 km

(c) Case 2: $\alpha = 10$ degrees, 40 km

(d) Case 6: $\alpha = 10$ degrees, 50 km

(e) Case 3: $\alpha = 20$ degrees, 40 km

(f) Case 7: $\alpha = 20$ degrees, 50 km

(g) Case 4: $\alpha = 30$ degrees, 40 km

(h) Case 8: $\alpha = 30$ degrees, 50 km

Figure 47. Wake investigation Mach contour plots.

rear stagnation point and compression zone. Additionally, as seen in Figure 47, the bow shock waves between the two altitudes were in similar locations thus justifying the use of the same grid between the 40 km and 50 km cases.

The following sections present additional details regarding the characteristics of the wake for each case. Contour plots of the temperatures and electron number-densities are shown to highlight the large region of non-equilibrium among the energy manifolds and the predicted ionization levels. Overall, it was apparent the electron-

electronic temperature was predicted to be significantly different, generally lower, than the vibrational temperature which indicates the three-temperature model is better suited than the two-temperature model for accurately predicting the thermo-chemical state within the wake. Additionally, properties along specified streamlines that traverse the domain are presented to quantitatively compare results of the three-temperature model to those of the two-temperature model.

5.3.1 0 degrees Angle of Attack

Figures 48 and 49 detail the temperatures and electron number-density in the wake for the 0 degrees angle of attack cases at 40 km (Case 1) and 50 km (Case 5), respectively. Due to the higher kinetic energy content in the freestream, the 40 km case obtained a higher translational-rotational temperature within the neck region of the wake, which translated to the other energy manifolds as well as the electron number-densities. These quantities were generally lower for the 50 km case. Additionally, the electron-electronic temperature was in a state of non-equilibrium with the vibrational, exceeding the vibrational temperature through the expansion region and along the edges of the core flow downstream.

Data along the streamlines identified in the top left contour plots of Figures 48 and 49 are presented in Figures 50 and 51, respectively. Also shown for comparison are results along those streamlines obtained using the two-temperature model. The initial spike in the temperatures was due to the passage through the bow shock wave, and the subsequent relaxation processes were similar to those observed along the stagnation streamlines. As the fluid moved around the nose cap it expanded causing the translational temperature to drop. The vibrational and electron-electronic energies were slow to respond to the new non-equilibrium potential and therefore their temperatures were higher than T_{tr} over the first half of the body, $X/L < 0.5$. Along the

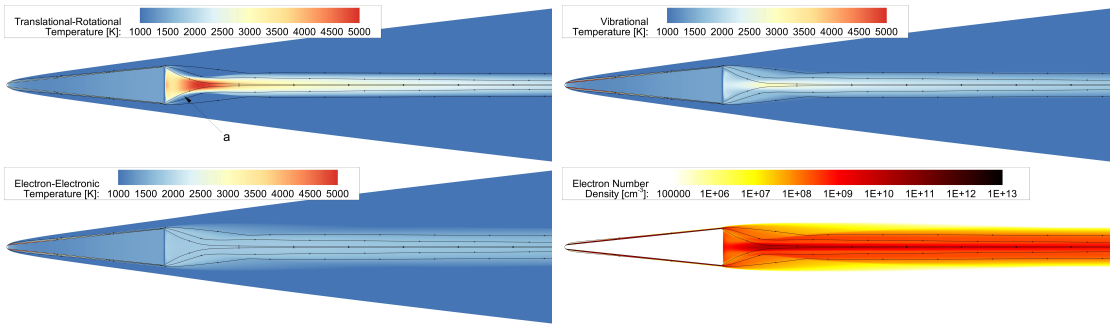

Figure 48. Wake investigation Case 1: $\alpha = 0$ degreese, 40 km

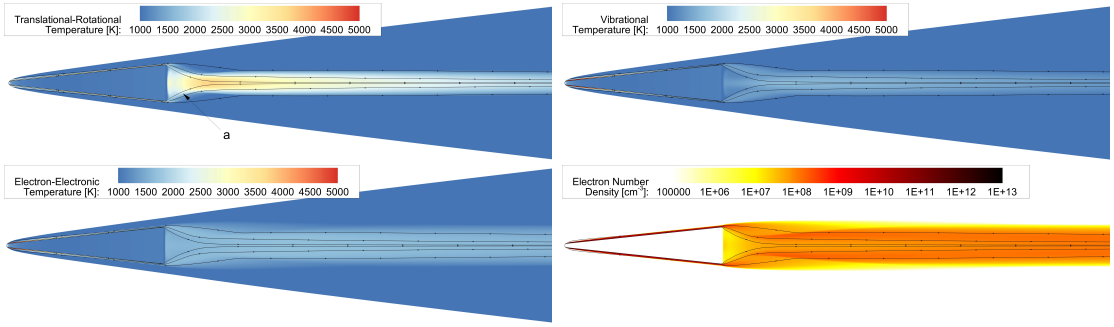

Figure 49. Wake investigation Case 5: $\alpha = 0$ degreese, 50 km

second have of the body, $0.5 < X/L < 1.0$, the streamline entered into the boundary layer and viscous dissipation caused the translational temperature to rise above the vibrational and electron-electronic temperatures. Within the wake, the translational-rotational and vibrational temperatures agreed well between the two models. The electron-electronic temperature, which closely followed the vibrational temperature over the forebody, froze just below 2,000K as the streamline expanded in the wake. The electron-electronic temperature remained low downstream due to the low quantity of electrons available for equilibration processes. Additionally, due to the smaller kinetic energy of the freestream, the 50 km case differed in that the translational-rotational and vibrational temperatures were predicted to be lower within the wake. The electron-electronic temperature was similar between the 40 km and 50 km cases, but was predicted to be higher than the vibrational temperature within the wake for the 50 km case.

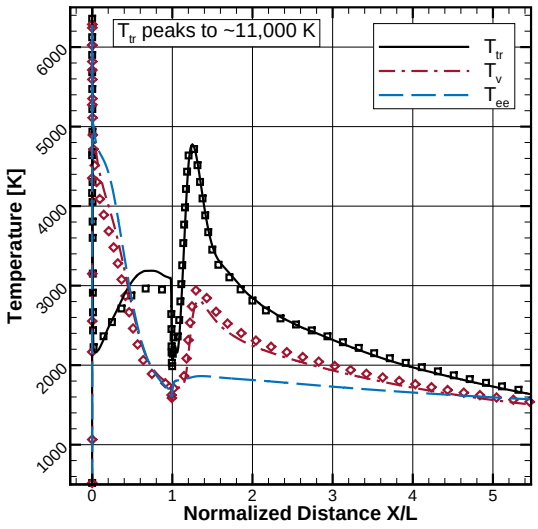

(a) Temperatures. ■ $= T_{tr}$ ♦ $= T_{vee}$

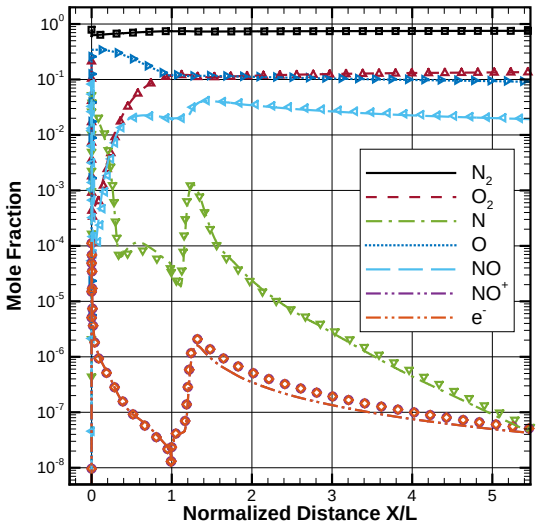

(b) Species concentrations. ■ $= N_2$ ▲ $= O_2$ ▼ $= N$ ►$= O$ ◄$= NO$ ● $= NO^+$ ♦ $= e^-$

Figure 50. Wake investigation Case 1 ($\alpha = 0$ degreese, 40 km) streamline *a*. $X/L = 0$ corresponds to the tip of the nose where L is the vehicle length. Symbols are results from the two-temperature model.

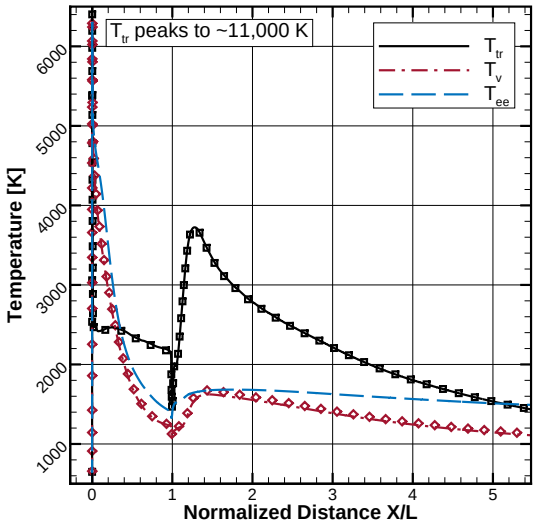

(a) Temperatures. ■ $= T_{tr}$ ♦ $= T_{vee}$

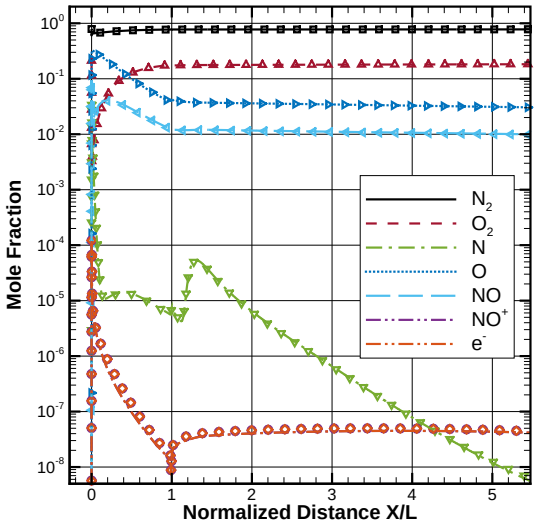

(b) Species concentrations. ■ $= N_2$ ▲ $= O_2$ ▼ $= N$ ►$= O$ ◄$= NO$ ● $= NO^+$ ♦ $= e^-$

Figure 51. Wake investigation Case 5 ($\alpha = 0$ degreese, 50 km) streamline *a*. $X/L = 0$ corresponds to the tip of the nose where L is the vehicle length. Symbols are results from the two-temperature model.

5.3.2 10 degrees Angle of Attack

The temperature and electron number-density contour plots detailing the wake for the 10 degrees angle of attack case at 40 km (Case 2) and 50 km (Case 6) are presented in Figures 52 and 53, respectively. With the increase in angle of attack, from that of Cases 1 and 5, came the formation of a vortex along the upper half the wake that was observed to be highly vibrationally and electron-electronically excited. This excited fluid flowed downstream, maintaining a high energy state for over two body lengths. Additionally, the leeward side of the vehicle was significantly populated by free-electrons that formed on the windward side and traversed around the vehicle to the leeward side. Concerning the lower half of the wake, the electron-electronic temperature was lower than the vibrational as the fluid from the forebody traversed under the vehicle into the wake.

The streamlines highlighted in the upper left contour plots of the 40 km altitude, 10 degrees angle of attack case, Figure 52, are detailed in Figures 54 and 55. Similarly, for the 50 km case Figures 56 and 57 detail the streamlines highlighted in Figure 53. Streamline a followed the flow within the highly vibrationally and electron-electronically excited fluid extending into the wake that originated from a fluid element that traversed the shock wave near the stagnation streamline. Streamline b followed a fluid element from the windward side underneath the vehicle and through the wake compression zone. Subsequent presentations of streamlines follow the same designations.

The initial temperature spike along streamline a for the 40 km case, Figure 54, was due to the passage through the bow shock wave. Subsequently, the fluid expanded over the nose where the translational-rotational temperature dropped while the vibrational and electron-electronic temperatures froze at approximately 5,000 K. The equilibration of these modes to the translational proceeded slowly, with the electron-

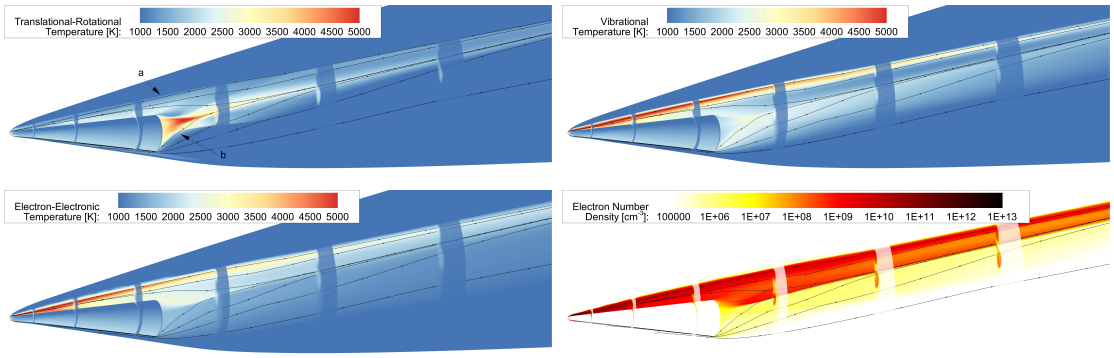

Figure 52. Wake investigation Case 2: $\alpha = 10$ degreese, 40 km

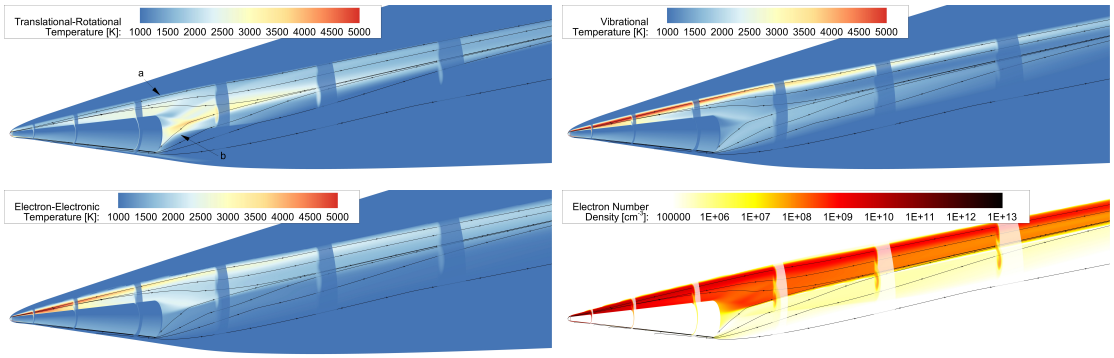

Figure 53. Wake investigation Case 6: $\alpha = 10$ degreese, 50 km

electronic temperature remaining lower than the vibrational for several body lengths into the wake. A slow ionic recombination rate was observed along this streamline, which resulted in a large concentration of free electrons in the wake. Similar results were observed along streamline a and the 50 km case, Figure 56; however, the equilibration of the electron-electronic energy to the translational-rotational energy was slightly faster than the 40 km case.

The streamline through the wake compression region, streamline b, for the 40 km case, Figure 54, hints at the complex nature of the flow-field over the windward side into the wake. The small spike near $X/L = 0$ was the passage through the shock wave, and the subsequent rise of the translational-rotational temperature was due to the streamline compressing towards the vehicle into the boundary layer as adjacent streamlines, off the symmetry plane, flowed around the cone towards the lee-ward

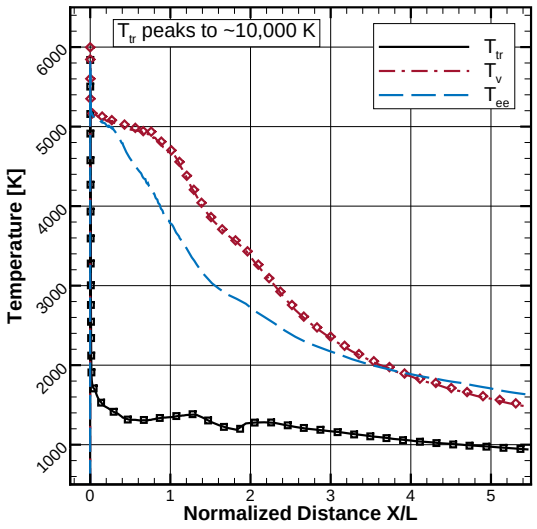

(a) Temperatures. ■ $= T_{tr}$ ♦ $= T_{vee}$

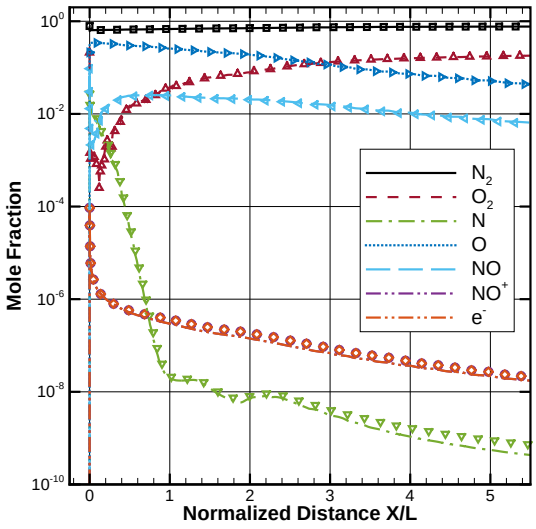

(b) Species concentrations. ■ $= N_2$ ▲ $= O_2$ ▼ $= N$ ►$= O$ ◄$= NO$ ● $= NO^+$ ♦ $= e^-$

Figure 54. Wake investigation Case 2 ($\alpha = 10$ degreese, 40 km) streamline *a*. $X/L = 0$ corresponds to the tip of the nose where L is the vehicle length. Symbols are results from the two-temperature model.

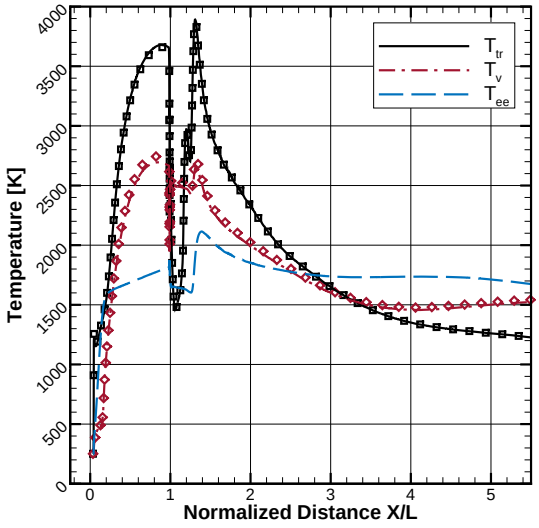

(a) Temperatures. ■ $= T_{tr}$ ♦ $= T_{vee}$

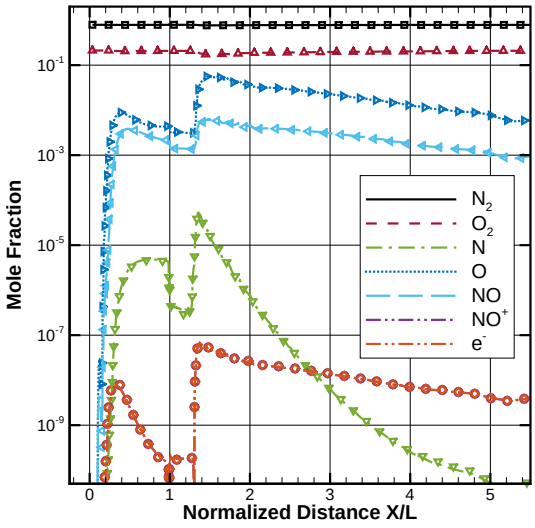

(b) Species concentrations. ■ $= N_2$ ▲ $= O_2$ ▼ $= N$ ►$= O$ ◄$= NO$ ● $= NO^+$ ♦ $= e^-$

Figure 55. Wake investigation Case 2 ($\alpha = 10$ degreese, 40 km) streamline *b*. $X/L = 0$ corresponds to the tip of the nose where L is the vehicle length. Symbols are results from the two-temperature model.

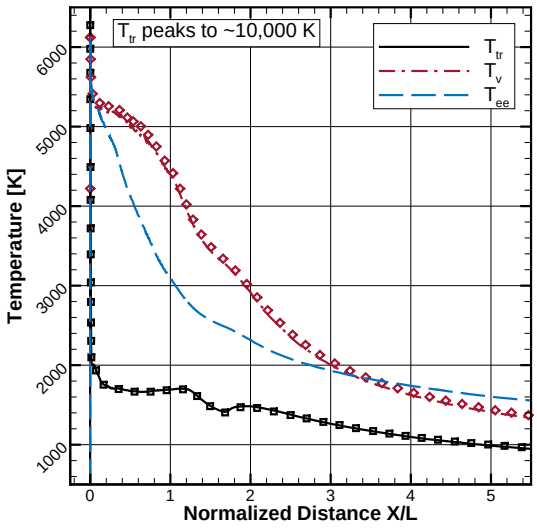

(a) Temperatures. ■ $= T_{tr}$ ♦ $= T_{vee}$

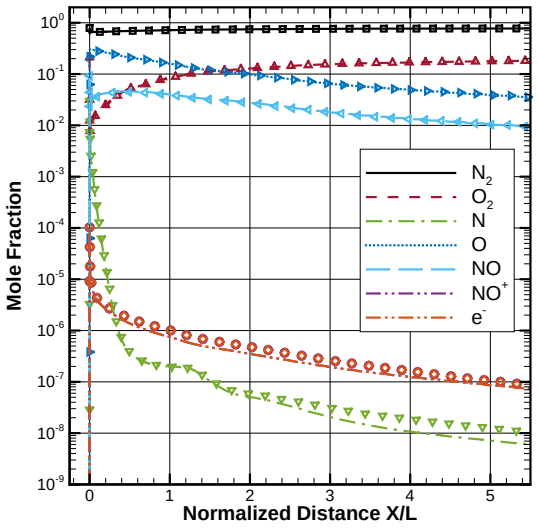

(b) Species concentrations. ■ $= N_2$ ▲ $= O_2$ ▼ $= N$ ►$= O$ ◄$= NO$ ●$= NO^+$ ♦ $= e^-$

Figure 56. Wake investigation Case 6 ($\alpha = 10$ degreese, 50 km) streamline *a*. $X/L = 0$ corresponds to the tip of the nose where L is the vehicle length. Symbols are results from the two-temperature model.

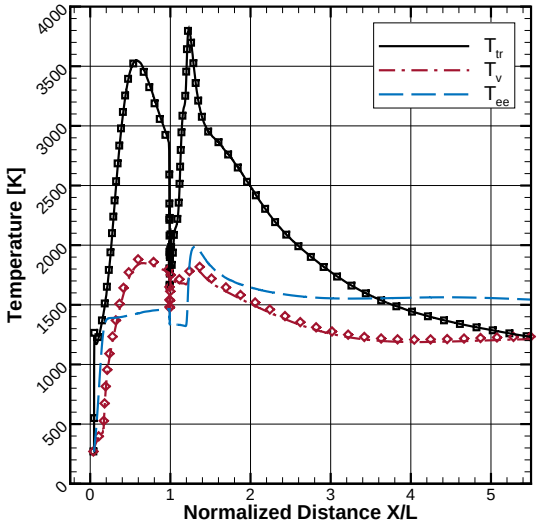

(a) Temperatures. ■ $= T_{tr}$ ♦ $= T_{vee}$

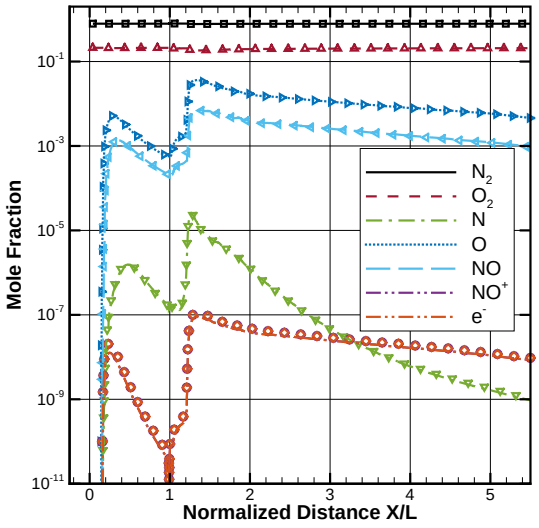

(b) Species concentrations. ■ $= N_2$ ▲ $= O_2$ ▼ $= N$ ►$= O$ ◄$= NO$ ●$= NO^+$ ♦ $= e^-$

Figure 57. Wake investigation Case 6 ($\alpha = 10$ degreese, 50 km) streamline *b*. $X/L = 0$ corresponds to the tip of the nose where L is the vehicle length. Symbols are results from the two-temperature model.

side. The vibrational temperature attempted to equilibrate with the translational-rotational, as did the electron-electronic, as the streamline approached the shoulder, $X/L = 1$. The low temperatures and small quantity of free-electrons resulted in the electron-electronic mode remaining in a low state over the forebody. The expansion region resulted in a sharp dip within the energy modes, and the compression region reheated the translational-rotational energy which then diffused to the vibrational and electron-electronic modes. The high translational temperature drove ionization reactions and additional free-electrons were produced. Proceeding downstream past the neck, $X/L > 1.1$, the translational-rotational and vibrational energies cooled while the electron-electronic manifold remained nearly frozen at an excited state. Similar trends were observed for the 50 km case, Figure 57.

5.3.3 20 degrees Angle of Attack

Cases 3 and 7, 20 degrees angle of attack at 40 km and 50 km are, respectively, detailed in Figures 58 and 59. As the angle of attack increased from 10 degrees, Cases 2 and 6, the amount of electrons found in the lower half the wake increased. The vibrational energy also exhibited a larger degree of population inversion, while the electron-electronic temperature still remained relatively low.

The low electron-electronic temperatures were the results to a combination of processes. Due to the slender vehicle geometry, there was only a small region, near the nose, where a strong normal shock existed and high translational-rotational temperatures produced by the shock diffused into the other energy modes. The remainder of the flow-field was processed by significantly weaker oblique shocks, the peak translational-rotational temperature was therefore less than that behind the normal shock, which resulted in less ionization and longer relaxation times for the electron energy. Therefore, the fluid was able to traverse the forebody and enter the wake before

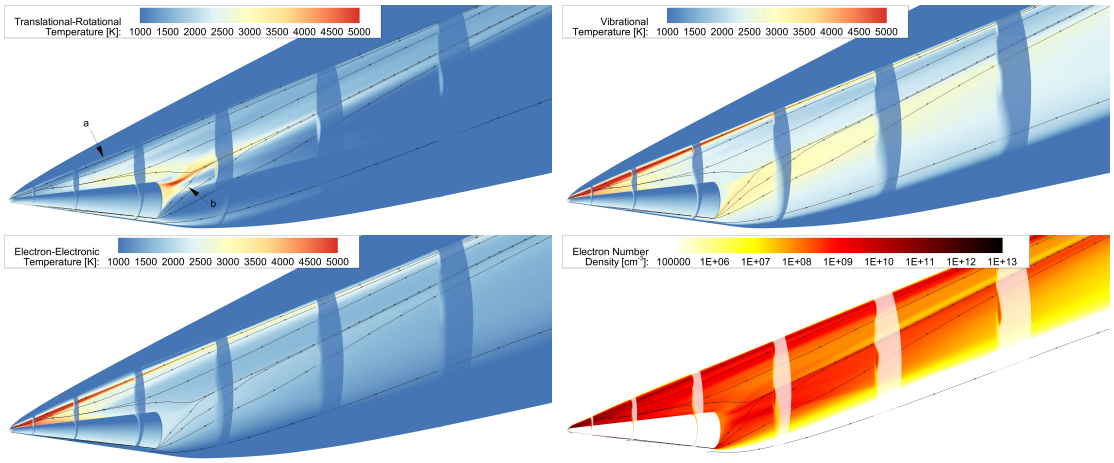

Figure 58. Wake investigation Case 3: $\alpha = 20$ degreese, 40 km

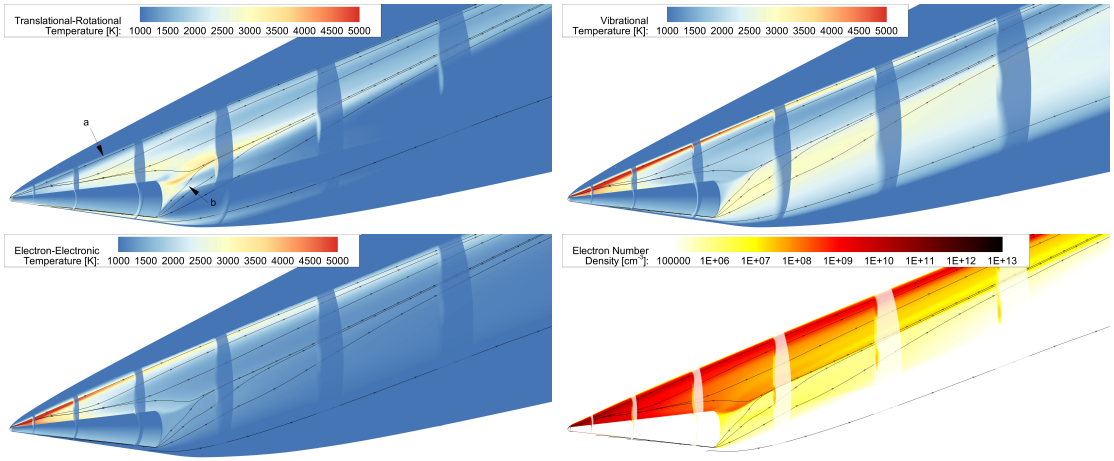

Figure 59. Wake investigation Case 7: $\alpha = 20$ degreese, 50 km

the electron-electronic energies were able to equilibrate with either the vibrational or translational modes. Then, once in the wake, the translational-rotational temperature dropped and the vibrational temperature froze, leaving the electron-electronic temperature in a state between the other two for the rest of the domain.

The streamlines highlighted for the 40 km case, Figure 58, are presented in Figures 60 and 61 and those highlighted for the 50 km case, Figure 59, are presented in Figures 62 and 63. The flow features detailed by these streamlines were largely the same as those presented for the 10 degrees angle of attack case. Within streamline *a*, following the fluid element over the nose into the wake, the vibrational and electron-electronic

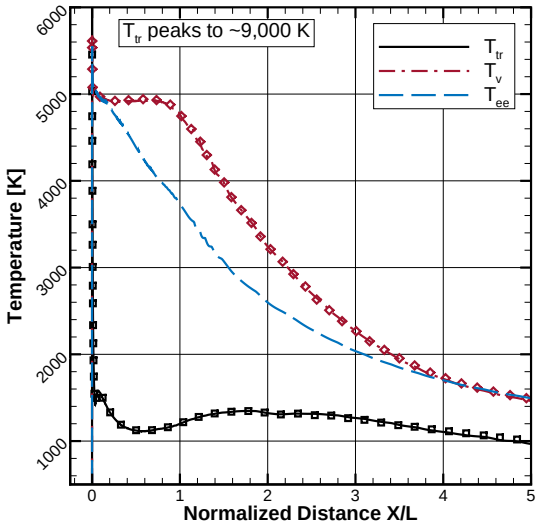

(a) Temperatures. ■ $= T_{tr}$ ♦ $= T_{vee}$

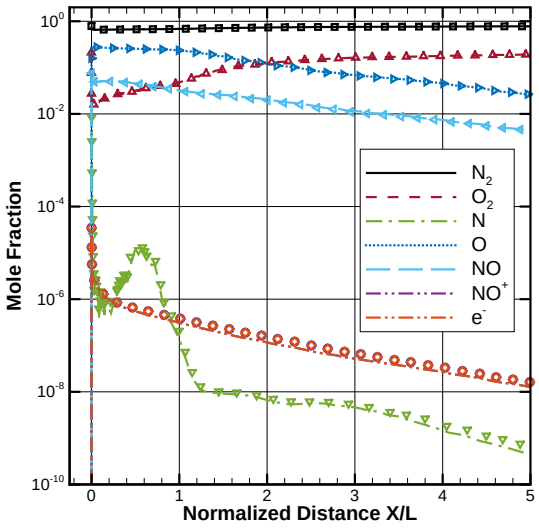

(b) Species concentrations. ■ $= N_2$ ▲ $= O_2$ ▼ $= N$ ►$= O$ ◄$= NO$ ●$= NO^+$ ♦ $= e^-$

Figure 60. Wake investigation Case 3 ($\alpha = 20$ degreese, 40 km) streamline *a*. $X/L = 0$ corresponds to the tip of the nose where L is the vehicle length. Symbols are results from the two-temperature model.

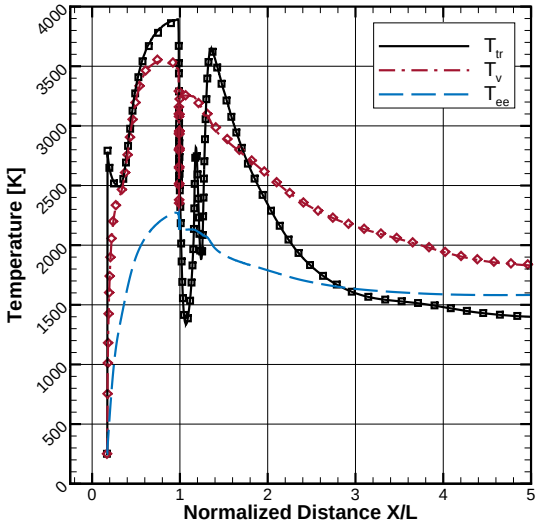

(a) Temperatures. ■ $= T_{tr}$ ♦ $= T_{vee}$

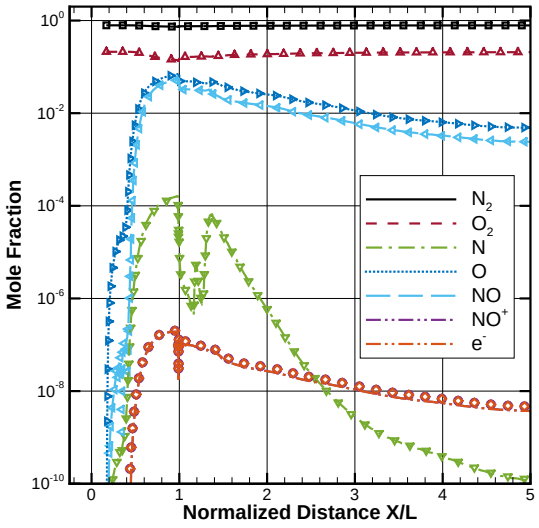

(b) Species concentrations. ■ $= N_2$ ▲ $= O_2$ ▼ $= N$ ►$= O$ ◄$= NO$ ●$= NO^+$ ♦ $= e^-$

Figure 61. Wake investigation Case 3 ($\alpha = 20$ degreese, 40 km) streamline *b*. $X/L = 0$ corresponds to the tip of the nose where L is the vehicle length. Symbols are results from the two-temperature model.

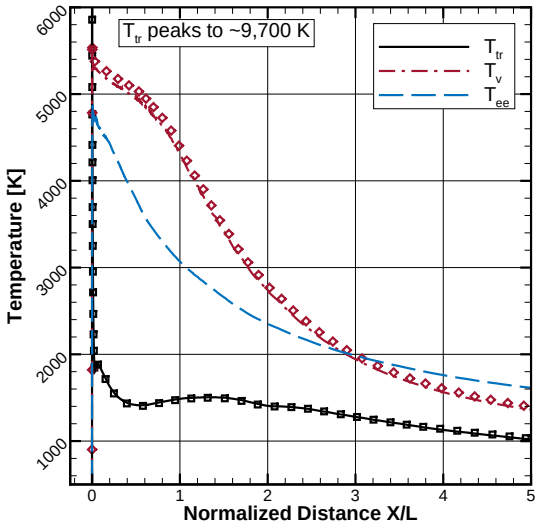

(a) Temperatures. ■ $= T_{tr}$ ♦ $= T_{vee}$

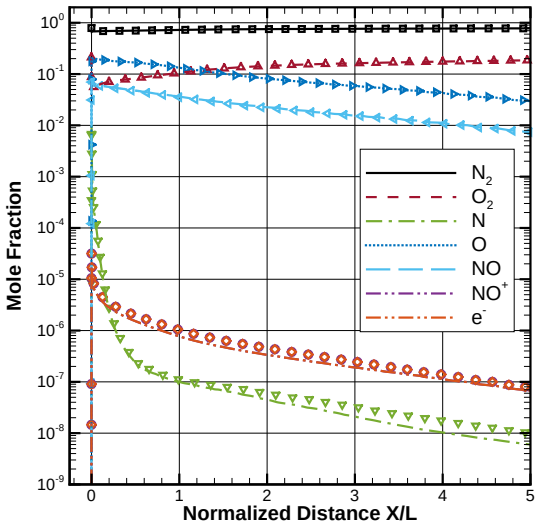

(b) Species concentrations. ■ $= N_2$ ▲ $= O_2$ ▼ $= N$ ►$= O$ ◄$= NO$ ●$= NO^+$ ♦ $= e^-$

Figure 62. Wake investigation Case 7 ($\alpha = 20$ degreese, 50 km) streamline *a*. $X/L = 0$ corresponds to the tip of the nose where L is the vehicle length. Symbols are results from the two-temperature model.

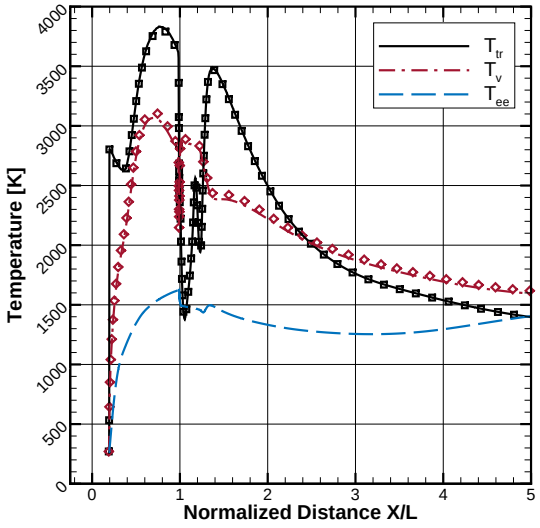

(a) Temperatures. ■ $= T_{tr}$ ♦ $= T_{vee}$

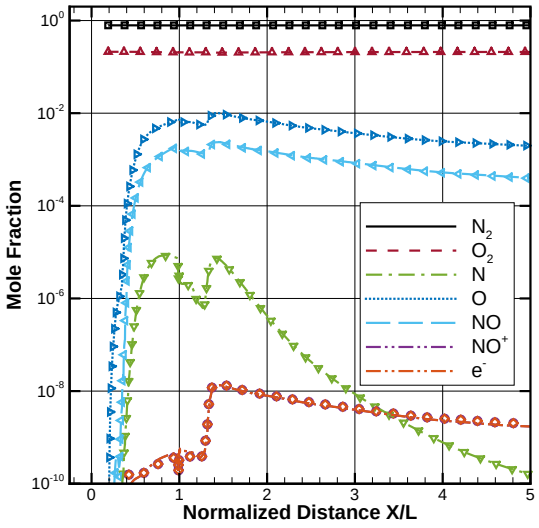

(b) Species concentrations. ■ $= N_2$ ▲ $= O_2$ ▼ $= N$ ►$= O$ ◄$= NO$ ●$= NO^+$ ♦ $= e^-$

Figure 63. Wake investigation Case 7 ($\alpha = 20$ degreese, 50 km) streamline *b*. $X/L = 0$ corresponds to the tip of the nose where L is the vehicle length. Symbols are results from the two-temperature model.

temperatures were approximately 5,000 K, and the free-electron concentrations slowly decayed into the wake. Along streamline *b*, the vibrational temperature followed the translational-rotational temperature through the major flow features: initial heating through the shock wave, viscous heating as the streamline entered the boundary layer, cooling through the expansion zone, and reheating through the wake compression zone and shock waves. The electron-electronic energy attempted to equilibrate with the other modes but was severely limited due the overall low amount of energy along the streamline: the translational temperature only obtained a maximum of approximately 4,000 K. Therefore, the electron-electronic temperature remained lower than the other temperatures for a majority of the streamline.

5.3.4 30 degrees Angle of Attack

Figures 64 and 65 detail the temperatures and electron number-densities within the wake for the 30 degrees angle of attack cases at 40 km (Case 4) and 50 km (Case 8), respectively. Immediately evident was the significantly increased level of ionization throughout the domain for both altitudes compared to the smaller angle of attack cases. Additionally, the extent of the vibrational energy population inversion was increased as well, while the electron-electronic energy remained at a relatively low value.

Streamlines *a* and *b* are presented, for the 30 degrees angle of attack case, in Figures 66 and 67 for the 40 km altitude case and Figures 68 and 69 for the 50 km case. Again, the major flow features along these streamlines were consistent with those observed for the lower angle of attack cases.

The results between the 40 km and 50 km cases for a given angle of attack were similar with respect to the overall wake structure. The nose vortex appeared in all cases above 0 degrees angle of attack which was highly vibrationally and electron-

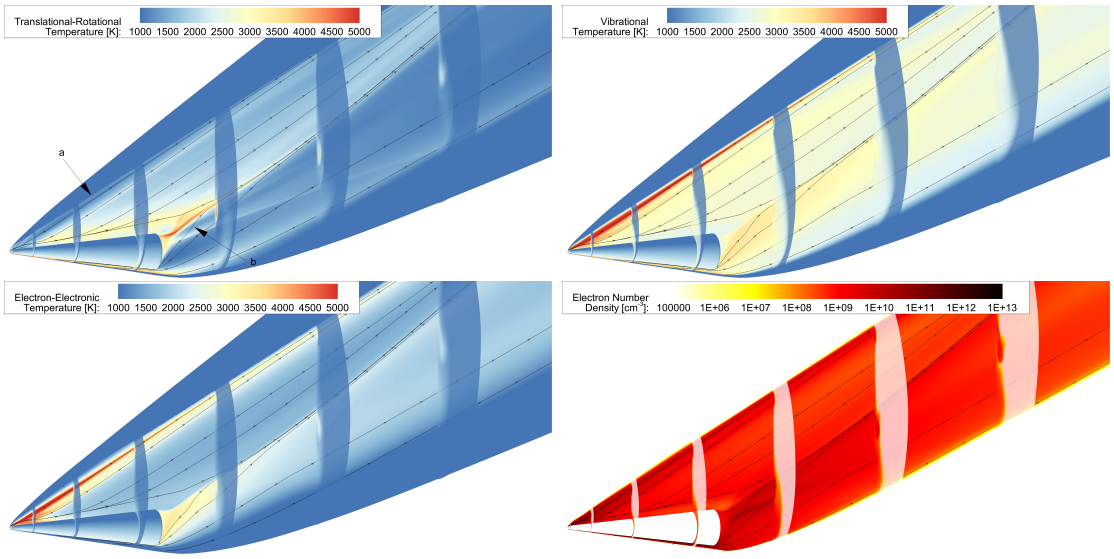

Figure 64. Wake investigation Case 4: $\alpha = 30$ degreese, 40 km

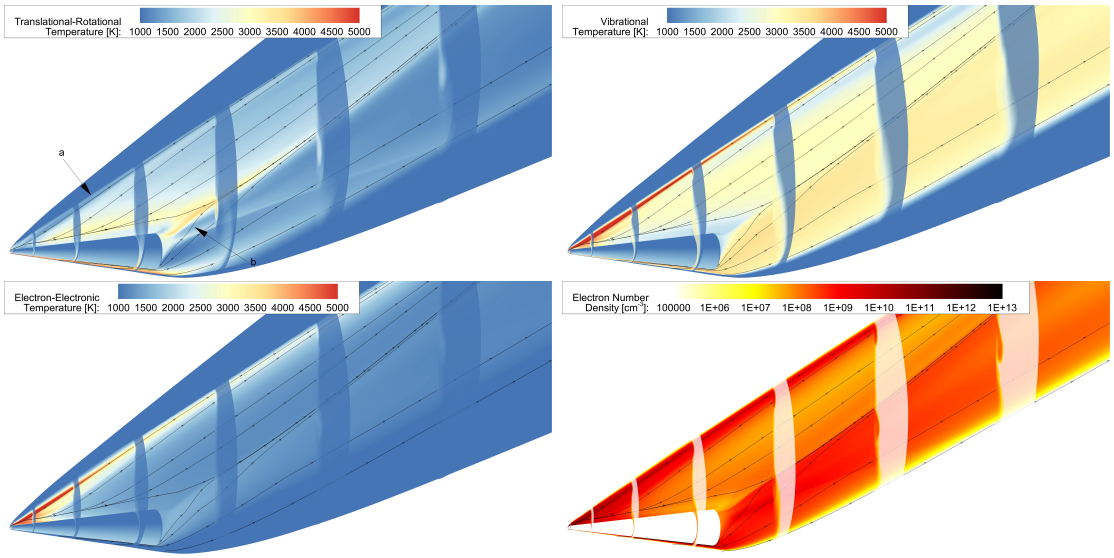

Figure 65. Wake investigation Case 8: $\alpha = 30$ degreese, 50 km

electronically excited and filled with free-electrons. The fluid within this vortex originated near the stagnation region; thus, the translational-rotational temperature reached high values through the shock wave and resulted in high temperatures within the other modes in the wake. Although the cross-sectional size of the wake increased with angle of attack, the near wake features including the nose vortex, expansion and compression zones, and wake shocks were similar in size, but did rotate, as the angle

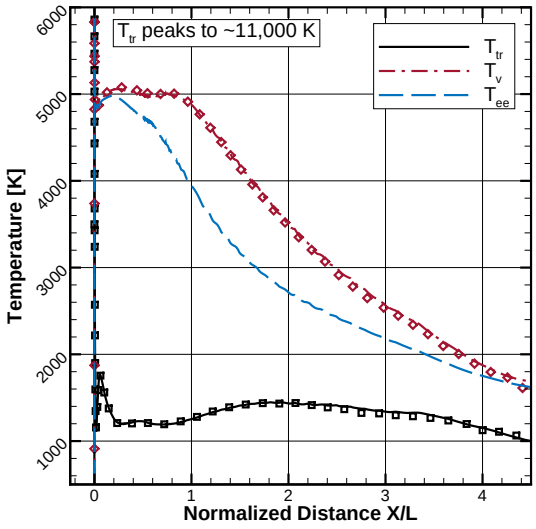

(a) Temperatures. ■ $= T_{tr}$ ♦ $= T_{vee}$

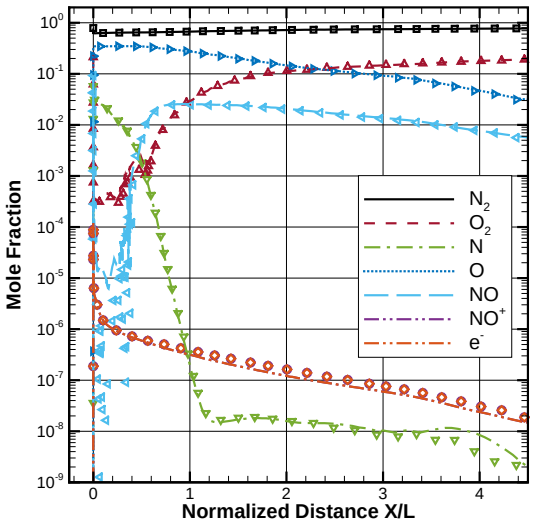

(b) Species concentrations. ■ $= N_2$ ▲ $= O_2$ ▼ $= N$ ►$= O$ ◄$= NO$ ● $= NO^+$ ♦ $= e^-$

Figure 66. Wake investigation Case 4 ($\alpha = 30$ degreese, 40 km) streamline *a*. $X/L = 0$ corresponds to the tip of the nose where L is the vehicle length. Symbols are results from the two-temperature model.

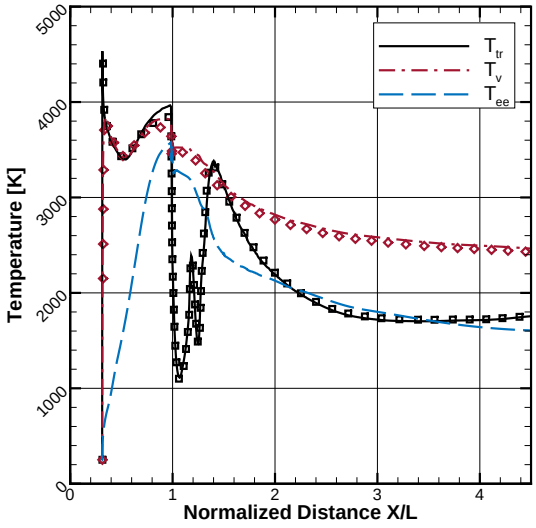

(a) Temperatures. ■ $= T_{tr}$ ♦ $= T_{vee}$

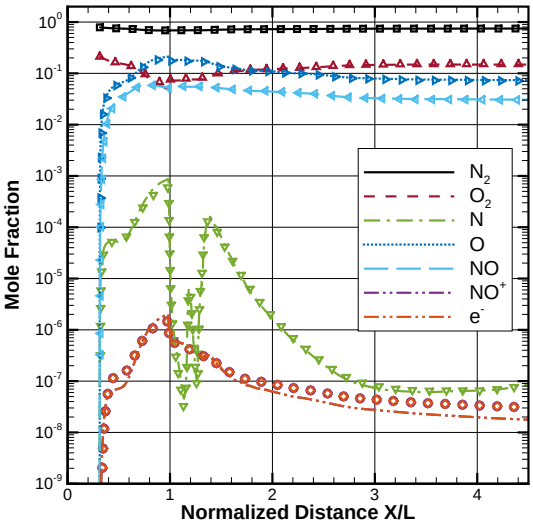

(b) Species concentrations. ■ $= N_2$ ▲ $= O_2$ ▼ $= N$ ►$= O$ ◄$= NO$ ● $= NO^+$ ♦ $= e^-$

Figure 67. Wake investigation Case 4 ($\alpha = 30$ degreese, 40 km) streamline *b*. $X/L = 0$ corresponds to the tip of the nose where L is the vehicle length. Symbols are results from the two-temperature model.

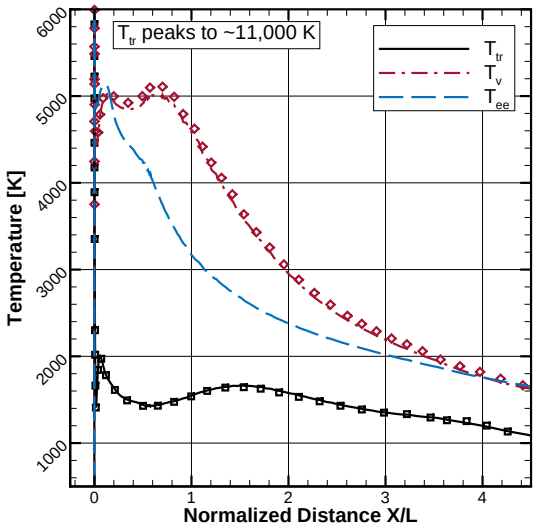

(a) Temperatures. ■ $= T_{tr}$ ♦ $= T_{vee}$

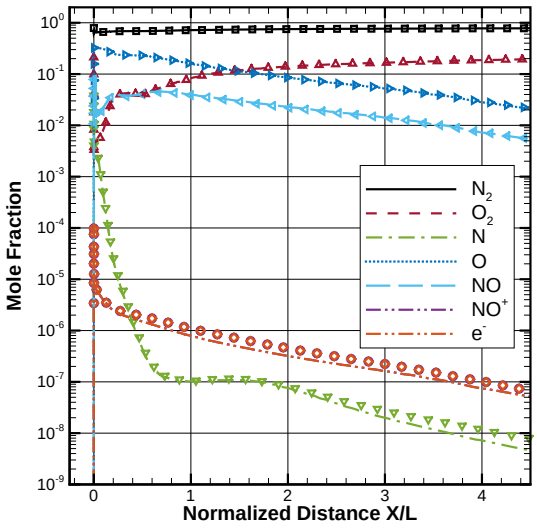

(b) Species concentrations. ■ $= N_2$ ▲ $= O_2$ ▼ $= N$ ►$= O$ ◄$= NO$ ●$= NO^+$ ♦ $= e^-$

Figure 68. Wake investigation Case 8 ($\alpha = 30$ degreese, 50 km) streamline *a*. $X/L = 0$ corresponds to the tip of the nose where L is the vehicle length. Symbols are results from the two-temperature model.

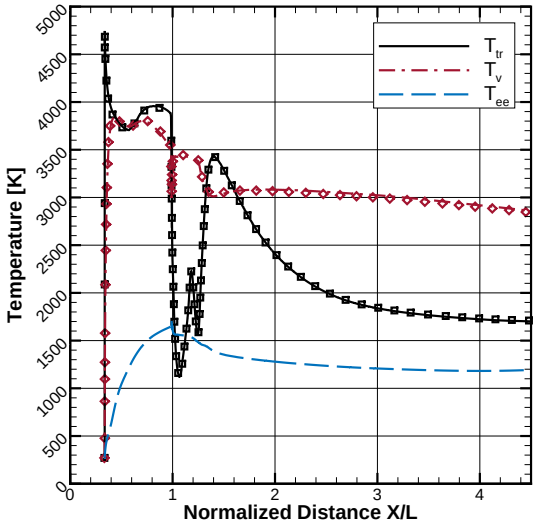

(a) Temperatures. ■ $= T_{tr}$ ♦ $= T_{vee}$

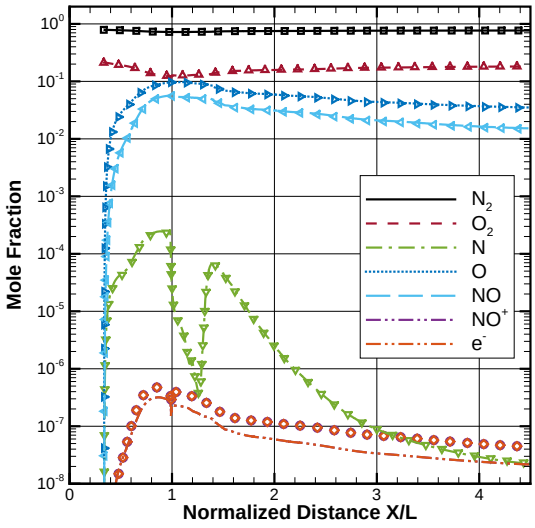

(b) Species concentrations. ■ $= N_2$ ▲ $= O_2$ ▼ $= N$ ►$= O$ ◄$= NO$ ●$= NO^+$ ♦ $= e^-$

Figure 69. Wake investigation Case 8 ($\alpha = 30$ degreese, 50 km) streamline *b*. $X/L = 0$ corresponds to the tip of the nose where L is the vehicle length. Symbols are results from the two-temperature model.

of attack increased.

In summary, the three-temperature thermochemical non-equilibrium model predicted the electron-electronic energy to be in a state of non-equilibrium with the other modes. Even though the gross wake structure predicted by the three-temperature model was largely the same as the two-temperature, the break-out of the electron-electronic energy, and therefore increase in the degrees of freedom of the simulation, led to a vastly different thermochemical state of the fluid and an increase in the accuracy of the solution.

5.4 Evaluation of the Continuum Assumption

The fluid continuum assumption, inherent in the current simulations, is known to fail in regions of steep gradients such as shock waves and expansions zones. Understanding the extent that this assumption is valid was important in interpreting the results of this study. Boyd, Chen, and Candler [20] developed a continuum breakdown parameter that calculates a localized Knudsen number. If the breakdown parameter, Kn_{GLL}, is less than 0.05 the continuum assumption is generally valid, and for values exceeding 0.05 the continuum assumption begins to fail. The gradient length-local Knudsen number, based on the fluid density, is [18]

$$Kn_{GLL} = \frac{\lambda}{\rho}\left|\frac{\partial \rho}{\partial x^i}\right|, \tag{130}$$

where the mean free path is [104]

$$\lambda = \frac{\mu}{\rho}\sqrt{\frac{\pi m}{2kT_t}} \tag{131}$$

and the average mass of a particle is

$$m = \sum X_s m_s. \tag{132}$$

Figure 70 presents Kn_{GLL} contours for the eight wake investigation cases. Only the near wake region showed areas where the continuum assumption began to break down. In particular, the largest Kn_{GLL} value was observed along the base of the

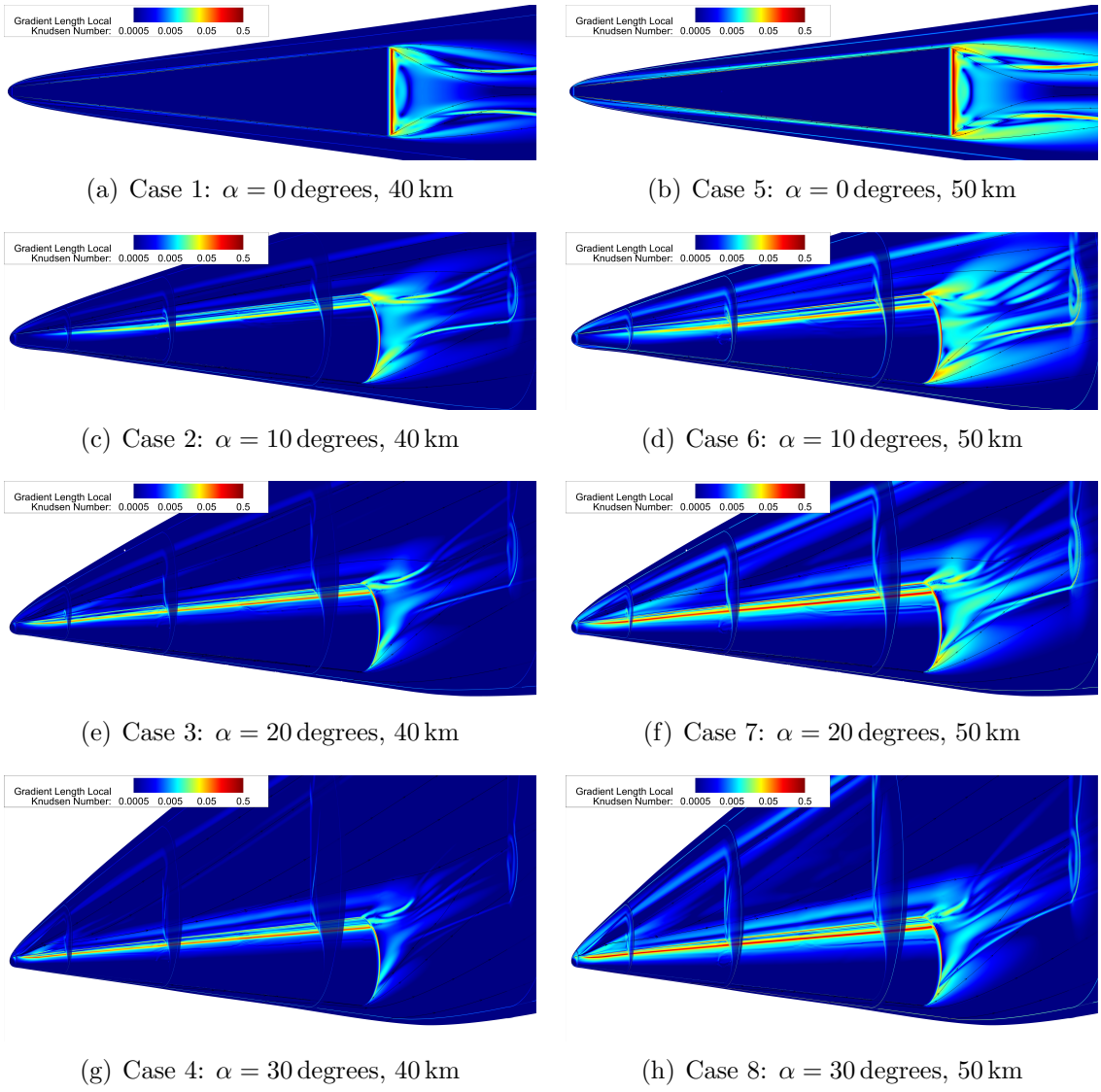

(a) Case 1: $\alpha = 0$ degrees, 40 km

(b) Case 5: $\alpha = 0$ degrees, 50 km

(c) Case 2: $\alpha = 10$ degrees, 40 km

(d) Case 6: $\alpha = 10$ degrees, 50 km

(e) Case 3: $\alpha = 20$ degrees, 40 km

(f) Case 7: $\alpha = 20$ degrees, 50 km

(g) Case 4: $\alpha = 30$ degrees, 40 km

(h) Case 8: $\alpha = 30$ degrees, 50 km

Figure 70. Wake investigation gradient length-local Knudsen number, Kn_{GLL}.

vehicle where, as expected, near vacuum conditions were predicted. The expansion and wake shocks also showed areas of breakdown. Although less severe, the leeward side of the vehicle showed signs of continuum breakdown for the cases where the angle of attack was greater than 0 degrees. This location coincided with the separation of the cross flow streamlines that coalesced into the vortex that ran along the leeward side.The 50 km cases exhibited larger regions of breakdown, which was as expected considering the freestream density was approximately an order of magnitude lower.

These figures serve to demonstrate the limitations of the CFD method within wake regions for conditions where the forebody flow-field is entirely within the continuum regime. A potential solution for these non-continuum regimes is a hybrid DSMC/CFD software where a DSMC solution is found in non-continuum regions while maintaining the CFD solution where appropriate. Even though these results show that the assumption inherent in the simulations of this study begin to breakdown in certain areas, these regions are limited in number and size, and the results presented are therefore still valid.

5.5 Global Trends

Since the electron number-density is closely tied to electron temperature, the overall ionization level of the solution domain is an important figure. The total number of free-electrons within the domain is presented in Figure 71(a) for all cases. As the angle of attack increased, so did the ionization level, and an exponential behavior for the ionization level from the 20 degrees to 30 degrees angle of attack cases was also observed. The 40 km cases predicted a higher degree of ionization than the 50 km cases because of the increased kinetic energy of the freestream conditions. Also shown are results obtained using the two-temperature model. Due to the electron-electronic temperature remaining lower than the vibrational temperature for a majority of the

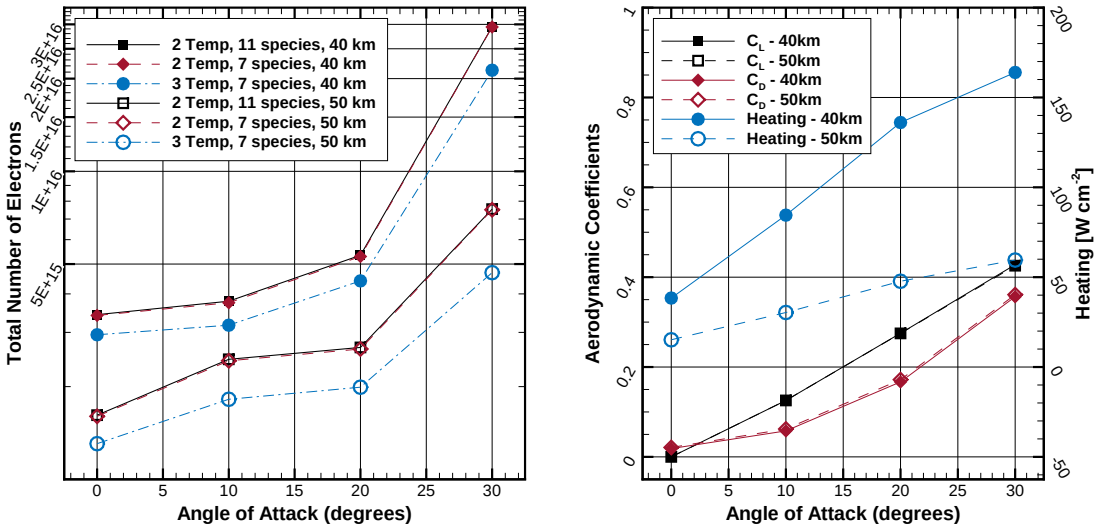

(a) Total number of electrons within the domain

(b) Surface quantities

Figure 71. Wake investigation trends.

domain, the three-temperature model predicted the number of free-electrons to be lower as compared to the two-temperature model.

Simulations were also conducted using an eleven-species two-temperature model. As shown in Figure 71(a) the seven-species and eleven-species models resulted in the same total electron count which validated the use of a seven-species air model for these conditions.

Figure 71(b) shows the aerodynamic coefficients and total heat flux to the vehicle for all cases using the electron-electronic three-temperature model. The coefficient of lift and drag increased with angle of attack, and the difference between the 40 km and 50 km cases was minimal. The total heat load for the 50 km case was lower than that of the 40 km case with both increasing with angle of attack. These trends were all consistent with expectations.

5.6 Wake Flow-Field Conclusions

A seven-species, three-temperature thermochemical non-equilibrium air model was used to conduct a parametric study of the wake structure behind a slender cone at hypersonic speeds. In total, eight cases were simulated at 40 km and 50 km altitude with angle of attacks ranging from 0 degrees to 30 degrees. Features of the wake structure were simulated using a massive, multi-block, structured domain with additional refinement concentrated in the wake to capture the recirculation and compression regions.

The complex wake structure had several features that were common for all cases with an angle of attack greater than 0 degrees. A significant portion exhibited a vibrational energy population inversion, the degree of which increased with angle of attack. The formation of a vibrationally and electron-electronically excited vortex was observed along the leeward side that extended several body lengths into the wake; this structure rotated but otherwise seemed to be invariant with angle of attack. Finally, the level of ionization increased with angle of attack, with a significant increase occurring from the 20 degrees to 30 degrees cases. The creation of the free-electrons occurred along the forebody and once the fluid traversed into the wake the population was essentially frozen for the remainder of the domain.

Within the wake, there was a significant degree of non-equilibrium between the electron and vibrational energies, which suggests that the three-temperature model captured additional non-equilibrium phenomena above the two-temperature model. This increase in accuracy, afforded by the three-temperature model, has the potential to drastically change the predictions for radiative heating, radio communication blackout and remote detection, and optical radiation for visual tracking.

VI. Conclusions

Hypersonic technologies have become the new frontier with numerous military applications being explored. Computational simulations are foundational to the development and assessment of such systems, and the legacy two-temperature thermochemical non-equilibrium model is typically utilized. This dissertation removed the limitations of the two-temperature model and developed two three-temperature models to more accurately simulate the thermochemical state of the flow-field around hypersonic vehicles.

The first research thrust was aimed at the development of two three-temperature thermochemical non-equilibrium models suitable for implementation into a computational architecture. Both three-temperature models account for thermal non-equilibrium phenomena by creating separate energy manifolds for the translational-rotational, vibrational, and free-electron energies. The difference between the two models was in how the electronic energy of the constituent species was allocated. The first, free-electron model, assumed that the vibrational and electronic energy exchange process was dominant and considered these two modes to be equilibrated, while a separate free-electron energy was considered. The second, electron-electronic model, assumed the electron-impact electronic-excitation process was dominant and grouped the electronic energy with the free-electron energy and assumed they were equilibrated at a common temperature. Additionally, the legacy two-temperature model, which assumed the vibrational, electronic, and free-electron energies were equilibrated at a common temperature, was presented. The equations governing the fluid dynamics were derived from first principles and presented in a finite volume formulation suitable for implementation within a CFD architecture.

In order to characterize the differences between the two three-temperature models and their potential ability to increase the fidelity of computational simulations, above

the two-temperature model, several zero-dimensional simulations were completed. Given a set of initial, non-equilibrium conditions, the governing equations were integrated in time until equilibrium was reached. The limitations of the free-electron three-temperature model were highlighted against results obtained with the two-temperature model where the differences between the thermochemical state through the relaxation processes were minimal, especially for the expansion case. Additionally, for the high Mach number flow conditions, the assumptions inherent in the free-electron model began to fail and the applicability of the model decreased. On the other hand, the electron-electronic three-temperature model exhibited behavior that was explainable by the physics of the simulation for all cases considered. The electron-electronic energy was the slowest to equilibrate, resulting to a different thermochemical state compared to the two-temperature model. Therefore, the electron-electronic three-temperature model was deemed to be the more viable three-temperature model for increasing the fidelity of hypersonic flow simulations.

Both three-temperature models were fully implemented within a CFD architecture and validation test cases were conducted against the experimentally determined electron number-densities of the RAM C-II flight test. The three-temperature models were in good agreement with the flight test data, and the simulations were extended far downstream to conduct an initial assessment of the three-temperature models performance within the wake. As expected given the results of the zero-dimensional simulations, the free-electron three-temperature model did not vary from the two-temperature model within the wake which suggests the ability of the free-electron model to increase the accuracy, above the two-temperature model, of the thermochemical state to be limited. However, the electron-electronic three-temperature model differed from the two-temperature model in that the electron-electronic energy was independent of the other two energy modes and was observed to be the

last to equilibrate. An additional investigation was conducted between three different diffusion models and results were compared to the experimental data; the higher fidelity Stefan-Maxwell equations, which solve for the true multicomponent diffusion velocities, resulted in better agreement with the RAM C-II flight test data than the commonly used approximate diffusion model. The simulations of the RAM C-II successfully validated the three-temperature thermochemical non-equilibrium models and determined the appropriateness of the Stefan-Maxwell equations in calculating the diffusion velocities for weakly ionized plasmas in the hypersonic flow regime.

The capstone research objective was to utilize the electron-electronic three-temperature model to simulate the flow-field around a slender hypersonic vehicle. The three-dimensional nature of the flow-field was investigated and results were compared to the two-temperature model to investigate if the newly developed and implemented three-temperature model increased the fidelity and accuracy of the solution. Eight different cases were simulated: two altitudes (40 km and 50 km) and four angles of attack (0, 10, 20, and 30 degrees). The complex structure of the wake was captured with a massive, multi-block, structured domain that was highly aligned to shock wave and had localized refinement in the wake recirculation, stagnation, and compression zones. These simulations demonstrated the ability of the three-temperature model to increase the fidelity of the thermochemical state of the fluid above that predicted by the two-temperature model.

The added fidelity that the newly developed three-temperature model affords has implications for future hypersonic simulations. Once coupled to radiative transport software, the three-temperature model would increase the accuracy of radiative predictions, and the increased accuracy of the electron number-density from the three-temperature model adds fidelity to radio blackout and remote detection predictions. Lastly, the higher fidelity thermochemical state of the three-temperature model in-

creases the accuracy of the prediction of optical radiation that can be utilized for visual tracking, especially when considering the large wakes behind hypersonic vehicles.

The work within this dissertation distinctly advances thermochemical non-equilibrium modeling used in the simulation of hypersonic flows. The ability of the three-temperature model to increase the solution fidelity, above the legacy two-temperature model, was demonstrated, and the application of the three-temperature model to a full, three-dimensional domain was shown to be computationally viable. However, there remain several avenues for future research concerning the use of the developed three-temperature models that should be explored:

- Couple the three-temperature model to a radiative transport software, such as High-Temperature Aerothermodynamic Radiation Algorithm (HARA) [53, 54], to investigate the radiative flux predicted with the use of the three-temperature model.

- Remove the ambipolar diffusion restriction, returning to the more complicated electron energy conservation equation, Equation 47. In doing so, precursor effects, where free-electrons are permitted to advance ahead of the bow shock wave, can be simulated and investigated.

- Consider faster speeds for the wake study behind a generic cone. It is expected that for faster speeds the energy modes along the forebody will relax more quickly and the electron-electronic energy will equilibrate to a greater extent before entering the wake. Then, the electron-electronic manifold is expected to freeze at a larger temperature than shown in this work and potentially be the largest of the three for large distances into the wake.

- Assess the unsteady nature of the wake. Within this dissertation, only steady

state solutions were obtained; however, it is expected that the wake would exhibit unsteady behavior which should be explored with time accurate simulations. Along the same lines, additional turbulence models should be considered !with deference given to large-eddy simulations (LES) due to the promising ability of such simulations to capture turbulent behavior.

- Conduct an investigation considering ablation in conjunction with the three-temperature model. The forebody flow-field with the addition of ablation would not be drastically different from that predicted by the two-temperature model because ablation products are essentially contained within the boundary layer, where thermal equilibrium is largely attained. However, ablation products entering the wake will emit radiation which could potentially be exploited; the increased thermochemical state predicted by the three-temperature model would increase the accuracy of the electronic state of these molecules thus increasing the radiative predictions.

Appendix A. Electronic Energy Levels and Degeneracies

Table A.1. Molecular Nitrogen, N_2 [84]

i	g_i	Θ_i $[K]$	i	g_i	Θ_i $[K]$	i	g_i	Θ_i $[K]$
1	1	0	5	3	95,351	9	5	109,974
2	3	72,232	6	1	98,057	10	6	126,468
3	6	85,778	7	2	99,683	11	6	128,248
4	6	86,050	8	2	103,731			

Table A.2. Molecular Oxygen, O_2 [84]

i	g_i	Θ_i $[K]$	i	g_i	Θ_i $[K]$	i	g_i	Θ_i $[K]$
1	3	0	8	3	71,641	15	2	10,7715
2	2	11,392	9	3	77,739	16	3	10,8282
3	1	18,985	10	6	79,887	17	1	10,9478
4	1	47,562	11	6	82,069	18	3	11,4934
5	6	49,911	12	8	97,608	19	1	11,8218
6	3	50,930	13	8	99,453			
7	10	56,514	14	2	104,803			

Table A.3. Nitrogen Atom, N [84]

i	g_i	Θ_i $[K]$	i	g_i	Θ_i $[K]$	i	g_i	Θ_i $[K]$
1	4	0	9	60	150,866	17	288	162,480
2	10	27,665	10	30	150,930	18	648	164,449
3	6	41,494	11	54	154,067	19	882	165,613
4	12	119,903	12	18	158,296	20	1152	166,367
5	6	124,012	13	90	158,719	21	1458	166,885
6	36	137,081	14	126	158,965	22	1800	167,255
7	18	139,263	15	54	160,226			
8	18	149,434	16	90	162,367			

Table A.4. Oxygen Atom, O [84]

i	g_i	Θ_i $[K]$	i	g_i	Θ_i $[K]$	i	g_i	Θ_i $[K]$
1	9	112	8	8	137,772	15	288	153,429
2	5	22,830	9	40	140,201	16	392	154,787
3	1	48,619	10	24	142,889	17	512	155,556
4	5	106,135	11	8	147,081	18	648	156,075
5	3	110,490	12	96	148,022	19	800	156,443
6	15	124,639	13	24	149,444			
7	9	127,520	14	168	151,638			

Table A.5. Nitric-Oxide, NO [84]

i	g_i	Θ_i $[K]$	i	g_i	Θ_i $[K]$	i	g_i	Θ_i $[K]$
1	4	0	6	4	75,084	11	4	88,916
2	8	55,835	7	2	76,377	12	2	89,885
3	2	63,257	8	4	77,172	13	2	90,518
4	4	66,086	9	4	86,850	14	4	90,700
5	4	68,989	10	2	87,232	15	4	92,194

Table A.6. Molecular Nitrogen Ion, N_2^+ [84]

i	g_i	Θ_i $[K]$	i	g_i	Θ_i $[K]$	i	g_i	Θ_i $[K]$
1	2	0	3	4	36,633	5	4	92,956
2	4	13,189	4	4	75,274			

Table A.7. Molecular Oxygen Ion, O_2^+ [84]

i	g_i	Θ_i $[K]$	i	g_i	Θ_i $[K]$
1	4	0	3	4	58,514
2	8	47,428	4	4	71,296

Table A.8. Nitrogen Atom Ion, N^+ [84]

i	g_i	Θ_i $[K]$	i	g_i	Θ_i $[K]$	i	g_i	Θ_i $[K]$
1	9	128	4	15	132721	7	12	214461
2	5	22036	5	9	157141			
3	1	47027	6	5	207455			

Table A.9. Oxygen Atom Ion, O^+ [84]

i	g_i	Θ_i $[K]$	i	g_i	Θ_i $[K]$	i	g_i	Θ_i $[K]$
1	4	0	3	6	58223	5	10	237097
2	10	38582	4	12	172557	6	18	268481

Table A.10. Nitric-Oxide Ion, NO^+ [84]

i	g_i	Θ_i $[K]$	i	g_i	Θ_i $[K]$	i	g_i	Θ_i $[K]$
1	1	0	4	6	89,031	7	2	102,801
2	3	75,090	5	3	97,434	8	2	105,710
3	6	85,233	6	1	100,052			

Bibliography

1. "Technology Horizons: A Vision for Air Force Science and Technology 2010-30," Vol. 1, September 2011. 1

2. "America's Air Force: A Call to the Future," July 2014. 1

3. Anderson, John D., *Modern Compressible Flow: With Historical Perspective*, McGraw-Hill, 3rd ed., 2003. 7

4. Anderson, John D., *Hypersonic and High-Temperature Gas Dynamics*, American Institute of Aeronautics and Astronautics, Inc., 2nd ed., 2006. 4, 115

5. Anderson, W. Kyle and Daryl L. Bonhaus, "An Implicit Upwind Algorithm for Computing Turbulent Flows on Unstructured Grids," *Computers and Fluids*, Vol. 23, No. 1, January 1994, pp. 1–21. 61, 62

6. Appleton, J. P. and K. N. Bray, "The Conservation Equations for a Non-Equilibrium Plasma," *Journal of Fluid Mechanics*, Vol. 20, No. 4, December 1964, pp. 659–672. 4, 5, 16, 32, 40

7. Atkinson, Kendall E., *An Introduction to Numerical Analysis*, John Wiley and Sons, Inc., 2nd ed., 1989. 63

8. Barnhardt, Michael and Graham V. Candler, "Detached-Eddy Simulation of the Reentry-F Flight Experiment," *Journal of Spacecraft and Rockets*, Vol. 49, No. 4, July-August 2012, pp. 691–699. 11

9. Behrens, Wilhelm, "The Far Wake behind Cylinders at Hypersonic Speeds. Part I: Flowfield," *AIAA Journal*, Vol. 5, No. 12, December 1967, pp. 2135–2141. 9

10. Behrens, Wilhelm, "Far Wake behind Cylinders at Hypersonic Speeds. Part II: Stability," *AIAA Journal*, Vol. 6, No. 2, February 1968, pp. 225–232. 9

11. Biedron, Robert T., Jan-Reneé Carlson, Joseph M. Derlaga, Peter A. Gnoffo, Dana P. Hammond, William T. Jones, Bil Kleb, Elizabeth M. Lee-Rausch, Eric J. Nielsen, Michael A. Park, Christopher L. Rumsey, James L. Thomas, and William A. Wood, "FUN3D Manual: 12.9," Tech. Rep. TM-2016-219012, NASA, February 2016. 61

12. Biedron, Robert T., Jan-Reneé Carlson, Joseph M. Derlaga, Peter A. Gnoffo, Dana P. Hammond, William T. Jones, Bil Kleb, Elizabeth M. Lee-Rausch, Eric J. Nielson, Michael A. Park, Christopher L. Rumsey, James L. Thomas, and William A. Wood, "FUN3D Manual: 13.1," Tech. Rep. TM-2017-219580, NASA, February 2017. 3, 6

13. Blazek, Jiri, *Computational Fluid Dynamics: Principles and Applications*, Elsevier Ltd., 3rd ed., 2015. 61, 62

14. Bose, Deepak and Graham V. Candler, "Thermal Rate Constants of the $O_2 + N \rightarrow NO + O$ Reaction Based on the $2A'$ and $4A'$ Potential-Energy Surfaces," *Journal of Chemical Physics*, Vol. 107, No. 16, October 1997, pp. 6136–6145. 45

15. Bourdon, A. and P. Vervisch, "Electron-Vibration Energy Exchange Models in Nitrogen Plasma Flows," *Physical Review E*, Vol. 55, No. 4, April 1997, pp. 4634–4641. 41, 42

16. Bourdon, A. and P. Vervisch, "Study of a Low-Pressure Nitrogen Plasma Boundary Layer over a Metallic Plate," *Physics of Plasmsa*, Vol. 4, No. 11, August 1997, pp. 4144–4157. 45

17. Bourdon, A. and P. Vervisch, "Analytical Models for Electron-Vibration Coupling in Nitrogen Plasma Flows," *Journal of Thermophysics and Heat Transfer*, Vol. 14, No. 4, October-December 2000, pp. 489–495. 41

18. Boyd, Iaian D. and Thomas E. Schwartzentruber, *Nonequilibrium Gas Dynamics and Moleculare Simulation*, Cambridge University Press, 2017. 2, 139

19. Boyd, Iain D., "Computation of Hypersonic Nonequilibrium Flows using the Direct Simulation Monte Carlo Method," *Hypersonic Nonequilibrium Flows: Fundamentals and Recent Advances*, edited by E. Josyula, Vol. 247 of *Progress in Astronautics and Aeronautics*, chap. 2. American Institute of Aeronautics and Astronautics, Inc., 2015. 2

20. Boyd, Iain D., Gang Chen, and Graham V. Candler, "Predicting Failure of the Continuum Fluid Equations in Transitional Hypersonic Flows," *The Physics of Fluids*, Vol. 7, No. 1, January 1995, pp. 210–219. 139

21. Brock, Joseph M., Pramod K. Subbareddy, and Graham V. Candler, "Detached-Eddy Simulations of Hypersonic Capsule Wake Flow," *AIAA Journal*, Vol. 53, No. 1, January 2015, pp. 70–80. 10

22. Candler, Graham V., "Next Generation CFD for Hypersonic and Aerothermal Flows," *22nd AIAA Computational Fluid Dynamcis Conference*, No. 2015-3048, June 2015. 116

23. Candler, Graham V., Heath B. Johnson, Ioannis Nompelis, Pramod K. Subbareddy, Travis W. Drayna, and Vladimyr Gidzak, "Development of the US3D Code for Advanced Compressible and Reacting Flow Simulations," *53rd AIAA Aerospace Sciences Meeting*, No. 2015-1893, January 2015. 3, 6

24. Candler, Graham V. and Robert W. MacCormack, "Computation of Weakly Ionized Hypersonic Flows in Thermochemical Nonequilibrium," *Journal of Thermophysics and Heat Transfer*, Vol. 5, No. 3, July-September 1991, pp. 266–273. 6, 12, 15, 91

25. Candler, Graham V. and Chul Park, "The Computation of Radiation from Nonequilibrium Hypersonic Flows," *23rd AIAA Thermophysics, Plasmadynamics, and Lasers Conference*, No. 1988-2678, June 1988. 42

26. Catris, Stéphane and Bertrand Aupoix, "Density Corrections for Turbulence Models," *Aerospace Science and Technology*, Vol. 4, No. 1, January 2000, pp. 1–11. 115

27. Chapman, Sydney and T. G. Cowling, *The Mathematical Theory of Non-Uniform Gases*, Cambridge University Press, 3rd ed., 1970. 14, 17, 19, 20, 22, 23, 25, 26, 28, 32, 48

28. Curtiss, C. F. and R. Byron Bird, "Multicomponent Diffusion," *Industrial and Engineering Chemistry Research*, Vol. 38, No. 7, July 1999, pp. 2515–2522. 48

29. Curtiss, Charles F. and Joseph O. Hirschfelder, "Transport Properties of Multicomponent Gas Mixtures," *The Journal of Chemical Physics*, Vol. 17, No. 6, June 1949, pp. 550–555. 48, 52, 105

30. Davidson, Norman, *Statistical Mechanics*, McGraw-Hill Book Company, Inc., 1962. 4, 35, 36, 37, 38

31. Dogra, Virendra K., James N. Moss, and Joseph M. Price, "Near-Wake Structure for a Generic Configuration or Aeroassisted Space Transfer Vehicles," *Journal of Spacecraft and Rockets*, Vol. 31, No. 6, November-December 1994, pp. 953–959. 10

32. Dogra, Virendra K., James N. Moss, Richard G. Wilmoth, Jeff C. Taylor, and H. A. Hassan, "Effects of Chemistry on Blunt-Body Wake Structure," *AIAA Journal*, Vol. 33, No. 3, March 1995, pp. 463–469. 10

33. Farbar, Erin, Iain D. Boyd, and Alexandre Martin, "Numerical Prediction of Hypersonic Flowfields Including Effects of Electron Translational Nonequilibrium," *Journal of Thermophysics and Heat Transfer*, Vol. 27, No. 4, October-December 2013, pp. 593–606. 12, 91

34. Ferdinando, Lisa, "Missile Defense Agency Director Outlines Priorities, Threats," *DoD News, Defense Media Activity*, March 2018. 1

35. Fujita, Kazuhisa, Tetsuya Yamada, and Nobuyuki Ishii, "Impact of Ablation Gas Kinetics on Hyperbolic Entry Radiative Heating," *44th AIAA Aerospace Sciences Meeting*, No. 2006-1185, January 2006. 45

36. Garamore, Jim, "DARPA Chief Describes Promising Furture Technologies," *DoD News, Defense Media Activity*, March 2018. 1

37. Gnoffo, Peater A., "Planetary-Entry Gas Dynamics," *Annual Review of Fluid Mechanics*, Vol. 31, January 1999, pp. 459–494. 7

38. Gnoffo, Peter A., "Code Calibration Program in Support of the Aeroassist Flight Experiment," *Journal of Spacecraft and Rockets*, Vol. 27, No. 2, March-April 1990, pp. 131–142. 12, 91

39. Gnoffo, Peter A., Roop N. Gupta, and Judy L. Shinn, "Conservation Equations and Physical Models for Hypersonic Air Flows in Thermal Chemical Nonequilibrium," Tech. Rep. TP-2867, NASA, February 1989. 29, 40, 46, 52, 54, 85, 90

40. Gnoffo, Peter A., Joseph M. Price, and Robert D. Braun, "Computation of Near-Wake, Aerobrake Flowfields," *Journal of Spacecraft and Rockets*, Vol. 29, No. 2, Marh-April 1992, pp. 182–189. 9

41. Gnoffo, Peter A., William A. Wood, William L. Kleb, Stephen J. Alter, and Christopher E. Glass, "A Tutorial for the Generic Gas Path in FUN3D," Tech. Rep. TM-2014-218658, NASA, November 2014. 3, 6

42. Golant, V. E., A. P. Zhilinksy, and I. E. Sakharov, *Fundamentals of Plasma Physics*, John Wiley and Sons, Inc., 1980. 51

43. Grasso, F. and G. Capano, "Modeling of Ionizing Hypersonic Flows in Nonequilibrium," *Journal of Spacecraft and Rockets*, Vol. 32, No. 2, March-April 1995, pp. 217–224. 12, 91

44. Grasso, F. and S. Pirozzoli, "Nonequilibrium Effects in Near-Wake Ionizing Flows," *AIAA Journal*, Vol. 35, No. 7, July 1997, pp. 1151–1163. 10, 12, 91

45. Gupta, Roop N., Kam-Pui Lee, Richard A. Thompson, and Jerrold M. Yos, "Calculations and Curve Fits for Thermodynamic and Transport Properties for Equilirbium Air to 30,000 K," Tech. Rep. RP-1260, NASA, October 1991. 52

46. Gupta, Roop N., Jerrold M. Yos, Richard A. Thompson, and Kam-Pui Lee, "A Review of Reaction Rates and Thermodynamic and Transport Properties for an 11-Species Air Model for Chemical and Thermal Nonequilibrium Calculations to 30,000 K," Tech. Rep. RP-1232, NASA, August 1990. 54

47. Heritier, K. L., R. L. Jaffe, V. Laporta, and M. Panesi, "Energy Transfer Models in Nitrogen Plasma: Analysis of $N_2(X^1\Sigma_g^+) - N(^4S_u) - e^-$ Interaction," *The Journal of Chemical Physics*, Vol. 141, No. 18, November 2014, pp. 184302. 41

48. Hirschfelder, Joseph O., Charles F. Curtiss, and R. Byron Bird, *Molecular Theory of Gases and Liquids*, John Wiley and Sons, Inc., 1954. 17, 22, 48, 53

49. Holt, E. H. and R. E. Haskell, *Foundations of Plasma Dynamics*, The Macmillan Company, 1965. 51

50. Huo, W. M, "Electron-Nitrogen Molecule Collisions in High-Temperature Nonequilibrium Air," *Thermophysical Aspects of Re-Entry Flows*, edited by J. N. Moss and C. D. Scott, Vol. 103 of *Progress in Astronautics and Aeronautics*. American Institute of Aeronautics and Astronautics, Inc., January 1986. 41

51. Johnston, C. O. and A. M. Brandis, "Modeling of Nonequilibrium CO Fourth-Positive and CN Violet Emission in CO_2-N_2 Gases," *Journal of Quantitative Spectroscopy and Radiative Transfer*, Vol. 149, December 2014, pp. 303–317. 45

52. Johnston, Christopher O. and Aaron M. Brandis, "Featues of Afterbody Radiative Heating for Earth Entry," *Journal of Spacecraft and Rockets*, Vol. 52, No. 1, January-February 2015, pp. 105–119. 11

53. Johnston, Christopher O., Brian R. Hollis, and Kenneth Sutton, "Non-Boltzmann Modeling for Air Shock-Layer Radiation at Lunar-Return Conditions," *Journal of Spacecraft and Rockets*, Vol. 45, No. 5, September-October 2008, pp. 879–890. 147

54. Johnston, Christopher O., Brian R. Hollis, and Kenneth Sutton, "Spectrum Modeling for Air Shock-Layer Radiation at Lunar-Return Conditions," *Journal of Spacecraft and Rockets*, Vol. 45, No. 5, September-October 2008, pp. 865–878. 147

55. Jones, Jr., W. Linwood and Aubrey E. Cross, "Electrostatic-Probe Measurements of Plasma Parameters for Two Reentry Flight Experiments at 25,000 Feet per Second," Tech. Rep. TN D-6617, NASA, February 1972. 11, 91, 94, 95, 106

56. Josyula, Eswar and William F. Bailey, "Governing Equations for Weakly Ionized Plasma Flowfields of Aerospace Vehicles," *Journal of Spacecraft and Rockets*, Vol. 40, No. 6, November-December 2003, pp. 845–857. 6, 12, 15, 91

57. Josyula, Eswar and Prakash Vedula, "Fundamental Fluid Transport Equations for Hypersonic Nonequilibrium Flows," *Hypersonic Nonequilibrium Flows: Fundamentals and Recent Advances*, edited by E. Josyula, Vol. 247 of *Progress in Astronautics and Aeronautics*, chap. 1. American Institute of Aeronautics and Astronautics, Inc., 2015. 6, 51

58. Jr., C. Forbes Dewey, "Near Wake of a Blunt Body at Hypersonic Speeds," *AIAA Journal*, Vol. 3, No. 6, June 1965, pp. 1001–1010. 9

59. Kim, Minkwan, Ali Gülhan, and Iain D. Boyd, "Modeling of Electron Energy Phenomena in Hypersonic Flows," *Journal of Thermophysics and Heat Transfer*, Vol. 26, No. 2, April-June 2012, pp. 244–257. 12, 41, 91

60. Kundu, Pijush K. and Ira M. Cohen, *Fluid Mechanics*, Elsevier Inc., 4th ed., 2008. 52

61. Laporta, V. and D. Bruno, "Electron-Vibration Energy Exchange Models in Nitrogen-Containing Plasma Flows," *The Journal of Chemical Physics*, Vol. 138, No. 104319, March 2013. 41

62. Lee, Jong-Hun, "Basic Governing Equations for the Flight Regimes of Aeroassisted Orbital Transfer Vehicles," *Thermal Design of Aeroassisted Orbital Transfer Vehicles*, edited by H. F. Nelson, Vol. 96 of *Progress in Astronautics and Aeronautics*. American Institute of Aeronautics and Astronautics, Inc., January 1985. 5, 7, 14, 15, 16, 29, 40, 41, 46, 47, 52, 53, 54, 56

63. Lee, Jong-Hun, "Electron-Impact Vibrational Excitation Rates in the Flowfield of Aeroassisted Orbital Transfer Vehicles," *Thermophysical Aspects of Re-Entry Flows*, edited by J. N. Moss and C. D. Scott, Vol. 103 of *Progress in Astronautics and Aeronautics*. American Institute of Aeronautics and Astronautics, Inc., January 1986. 6, 41, 42, 43

64. Lee, Jong-Hun, "Electron-Impact Vibrational Relaxation in High-Temperature Nitrogen," *Journal of Thermophysics and Heat Transfer*, Vol. 7, No. 3, July-September 1993, pp. 399–405. 42, 43, 63, 65, 66, 67, 68, 69, 70, 71, 72, 73, 74, 75, 76, 77, 78, 79, 80, 81, 83, 84, 89, 115

65. Lees, Lester, "Hypersonic Wakes and Trails," *AIAA Journal*, Vol. 2, No. 3, March 1964, pp. 417–428. 7, 9

66. Lin, T. C., L. K. Sproul, M. Kim, M. Olmos, and H. Feiz, "Hypersonic Reentry Vehicle Wake Flow Fields at Angle of Attack," *44th AIAA Aerospace Sciences Meeting*, No. 2006-0582, January 2006. 11

67. Lykoudis, Paul S., "A Review of Hypersonic Wake Studies," *AIAA Journal*, Vol. 4, No. 4, April 1966, pp. 577–590. 7, 8

68. MacCormack, Robert W., *Numerical Computation of Compressible and Viscous Flow*, American Institute of Aeronautics and Astronautics, Inc., 2014. 61

69. Martin, Jr., Christopher L., *Coupled Radiation-Gasdynamic Solution Method for Hypersonic Shock Layers in Thermochemical Nonequilibrium*, Ph.D. dissertation, Air Force Institute of Technology, 2950 Hobson Way, WPAFB OH, 45433-8865, December 2011. 6

70. Mazaheri, Alireza, Peter A. Gnoffo, Christopher O. Johnston, and Bil Kleb, "LAURA Users Manual: 5.5-65135," Tech. Rep. TM-2013-217800, NASA, February 2013. 6

71. McBride, Bonnie J. and Sanford Gordon, "Computer Program for Calculating and Fitting Thermodynamic Functions," Tech. Rep. RP-1992-1271, NASA, November 1992. 38, 39

72. McBride, Bonnie J. and Sanford Gordon, "Computer Program for Calculation of Complex Chemical Equilibrium Compositions and Applications II. Users Manual and Program Description," Tech. Rep. RP-1996-1311, NASA, June 1996. 38, 39

73. McBride, Bonnie J., Sanford Gordon, and Martin A. Reno, "Coefficients for Calculating Thermodynamic and Transport Properties of Individual Species," Tech. Rep. TM-1993-4513, NASA, October 1993. 38, 39

74. Mertens, John D., "Computational Model of Nitrogen Vibrational Relaxation by Electron Collisions," *Journal of Thermophysics and Heat Transfer*, Vol. 13, No. 2, April-June 1999, pp. 204–209. 42, 43, 63, 67, 68, 69, 70, 73, 74, 75, 76, 78, 79, 80, 81, 83, 84, 89

75. Millikan, Roger C. and Donald R. White, "Systematics of Vibrational Relaxation," *The Journal of Chemical Physics*, Vol. 39, No. 12, December 1963, pp. 3209–3213. 40

76. Morse, T. F., "Energy and Momentum Exchange between Non-Equipartition Gases," *The Physics of Fluids*, Vol. 6, No. 10, October 1963, pp. 1420–1427. 32, 46

77. Morse, T. F., "Energy and Momentum Exchange between Nonequipartition Gases," Tech. Rep. ARAP-5-P, Project SQUID, March 1963. 32, 46

78. Moss, James N., Robert A. Mitcheltree, Virendra K. Dogra, and Richard G. Wilmoth, "Direct Simulation Monte Carlo and Navier-Stokes Simulations of Blunt Body Wake Flows," *AIAA Journal*, Vol. 32, No. 7, July 1994, pp. 1399–1406. 10

79. Park, Chul, "Problems of Rate Chemistry in the Flight Regimes of Aeroassisted Orbital Transfer Vehicles," *Thermal Design of Aeroassisted Orbital Transfer Vehicles*, edited by H. F. Nelson, Vol. 96 of *Progress in Astronautics and Aeronautics*. American Institute of Aeronautics and Astronautics, Inc., January 1985. 41

80. Park, Chul, "Converence of Computation of Chemical Reacting FLows," *Thermophysical Aspects of Re-Entry Flows*, edited by J. N. Moss and C. D. Scott, Vol. 103 of *Progress in Astronautics and Aeronautics*. American Institute of Aeronautics and Astronautics, Inc., January 1986. 5, 42

81. Park, Chul, "Assessment of a Two-Temperature Kinetic Model for Dissociating and Weakly Ionizing Nitrogen," *Journal of Thermophysics and Heat Transfer*, Vol. 2, No. 1, January 1988, pp. 8–16. 5

82. Park, Chul, "Assessment of Two-Temperature Kinetic Model for Ionizing Air," *Journal of Thermophysics and Heat Transfer*, Vol. 3, No. 3, July 1989, pp. 233–244. 5, 41

83. Park, Chul, "A Review of Reaction Rates in High Temperature Air," *24th AIAA Thermophysics Conference*, No. 1989-1740, June 1989. 46

84. Park, Chul, *Nonequilibrium Hypersonic Aerothermodynamics*, John Wiley and Sons, Inc., 1990. 2, 3, 4, 6, 7, 14, 15, 28, 29, 31, 34, 39, 40, 41, 45, 46, 47, 52, 53, 55, 56, 92, 149, 150, 151

85. Park, Chul, "Review of Chemical-Kinetic Problems for Future NASA Missions, I: Earth Entries," *Journal of Thermophysics and Heat Transfer*, Vol. 7, No. 3, July-September 1993, pp. 385–398. 41, 42, 45

86. Park, Chul, Richard L. Jaffe, and Harry Partridge, "Chemical-Kinetic Parameters of Hyperbolic Earth Entry," *Journal of Thermophysics and Heat Transfer*, Vol. 15, No. 1, January-March 2001, pp. 76–90. 45

87. Pellerin, Cheryl, "DoD Officials Discuss Science, Technology Budget," *DoD News, Defense Media Activity*, April 2015. 1

88. Pellerin, Cheryl, "Budget Request Seeks Greater Missile Defense Capabilities," *DoD News, Defense Media Activity*, May 2017. 1

89. Petschek, Harry and Stanley Byron, "Approach to Equilibrium Ionization behind Strong Shock Waves in Argon," *Annals of Physics*, Vol. 1, No. 3, June 1957, pp. 270–315. 32

90. Pletcher, Richard H., John C. Tannehill, and Dale A. Anderson, *Computational Fluid Mechanics and Heat Transfer*, CRC Press, 3rd ed., 2013. 61

91. Raghunandan, Pratibha and Stephen M. Ruffin, "Influences of Multi-Temperature Models on Shock Structures of Weakly Ionized Hypersonic Flows," *46th AIAA Thermophysics Conference*, No. 2016-4314, June 2016. 12, 91

92. Ramshaw, J. D. and C. H. Chang, "Ambipolar Diffusion in Two-Temperature Multicomponent Plasmas," *Plasma Chemistry and Plasma Processing*, Vol. 13, No. 3, September 1993, pp. 489–498. 48, 50, 51, 105, 115

93. Ramshaw, J. D. and C. H. Chang, "Multicomponent Diffusion in Two-Temperature Magnetohydrodynamics," *Physical Review E*, Vol. 53, No. 6, June 1996, pp. 6382–6388. 48, 105, 115

94. Ramshaw, John D., "Hydrodynamic Theory of Multicomponent Diffusion and Thermal Diffusion in Multitemperature Gas Mixtures," *Journal of Non-Equilibrium Thermodynamics*, Vol. 18, No. 2, October 1993, pp. 121–134. 48

95. Reis, Victor H., "Chemiluminescent Radiation from the Far Wake of Hypersonic Spheres," *AIAA Journal*, Vol. 5, No. 11, November 1967, pp. 1928–1933. 9

96. Roe, Philip L., "Approximate Riemann Solvers, Parameter Vectors, and Difference Schemes," *Journal of Computational Physics*, Vol. 43, No. 2, October 1981, pp. 357–372. 62

97. Schulz, G. J., "Vibrational Excitation of Nitrogen by Electron Impact," *Physical Review*, Vol. 125, No. 1, January 1962, pp. 229–232. 42

98. Spalart, P. R. and S. R. Allmaras, "A One-Equation Turbulence Model for Aerodynamic Flows," *30th AIAA Aerospace Sciences Meeting*, No. 1992-0439, January 1992. 115

99. Spalart, P. R. and S. R. Allmaras, "A One-Equation Turbulence Model for Aerodynamic Flows," *Recherche Aérospatiale*, No. 1, May 1994, pp. 5–21. 115

100. Sutton, George W. and Arthur Sherman, *Engineering Magnetohydrodynamics*, McGraw-Hill, 1965. 4, 5, 15, 19, 20, 21, 27, 31, 32, 33, 40, 46, 47, 52, 56

101. Sutton, Kenneth and Peter A. Gnoffo, "Multi-Component Diffusion with Application to Computational Aerothermodynamics," *7th AIAA/ASME Joint Thermophysics and Heat Transfer Conference*, No. 1998-2575, June 1998. 48, 49, 52, 105

102. Taylor, R. L., B. W. Melcher II, and W. K. Washburn, "Studies of the Luminous Hypersonic Wake," *AIAA Journal*, Vol. 2, No. 10, October 1964, pp. 1731–1738. 9

103. Toro, Eleuterio F., *Riemann Solvers and Numerical Methods for Fluid Dynamics: A Practical Introduction*, Springer, 3rd ed., 2009. 61, 62

104. Vincenti, Walter G. and Charles H. Kruger, Jr., *Introduction to Physical Gas Dynamics*, Krieger Publishing Company, 1965. 2, 4, 14, 19, 29, 35, 36, 42, 44, 48, 52, 139

105. Wilke, C. R., "A Viscosity Equation for Gas Mixtures," *The Journal of Chemical Physics*, Vol. 18, No. 4, April 1950, pp. 517–519. 54

106. Wilmoth, Richard G., Robert A. Mitcheltree, James N. Moss, and Virendra K. Dogra, "Zonally Decoupled Direct Simulation Monte Carlo Solutions of Hypersonic Blunt-Body Wake Flows," *Journal of Spacecraft and Rockets*, Vol. 31, No. 6, November-December 1994, pp. 971–979. 10

107. Wright, Michael, Mark Loomis, and Periklis Papadopoulos, "Aerothermal Analysis of the Project Fire II Afterbody Flow," *Journal of Thermophysics and Heat Transfer*, Vol. 17, No. 2, April-June 2003, pp. 240–249. 10

108. Wright, Michael J., Graham V. Candler, and Deepak Bose, "Data-Parallel Line Relaxation Method for the Navier-Stokes Equations," *AIAA Journal*, Vol. 36, No. 9, September 1998, pp. 1603–1609. 6

109. Wright, Michael J., Helen H. Hwang, and David W. Schwenke, "Recommended Collision Integrals for Transport Property Computations Part II: Mars and Venus Entries," *AIAA Journal*, Vol. 45, No. 1, January 2007, pp. 281–288. 54

110. Wright, Michael J., Frank S. Milos, and Philippe Tran, "Afterbody Aeroheating Flight Data for Planetary Probe Thermal Protection System Design," *Journal of Spacecraft and Rockets*, Vol. 43, No. 5, September-October 2006, pp. 929–943. 3

111. Wright, Michael J., Deepak Bose Grant E. Palmer, and Eugene Levin, "Recommended Collision Integrals for Transport Property Computations Part 1: Air Species," *AIAA Journal*, Vol. 43, No. 12, December 2005, pp. 2558–2564. 54

112. Wright, Michael J., Dinesh K. Prabhu, and Edward R. Martinez, "Analysis of Apollo Command Module Afterbody Heating Part I: AS-202," *Journal of Spacecraft and Rockets*, Vol. 20, No. 1, January-March 2006, pp. 16–30. 10

113. Yee, H. C., "On Symmetric and Upwind TVD Schemes," Tech. Rep. TM-1985-86842, NASA, September 1985. 62

114. Yos, Jerrold M., "Transport Properties of Nitrogen, Hydrogen, Oxygen, and Air to 30,000K," Tech. Rep. RAD-TM-63-7, AVCO Corp., March 1963. 54

REPORT DOCUMENTATION PAGE

Form Approved
OMB No. 0704–0188

1. REPORT DATE *(DD–MM–YYYY)*	2. REPORT TYPE	3. DATES COVERED *(From — To)*
14–09–2018	Dissertation	Sep 2015 — Sep 2018

4. TITLE AND SUBTITLE

Thermochemical Non-Equilibrium Models for Weakly Ionized Hypersonic Flows with Application to Slender-Body Wakes

5a. CONTRACT NUMBER

5b. GRANT NUMBER

5c. PROGRAM ELEMENT NUMBER

6. AUTHOR(S)

Clarey, Matthew P., Capt, USAF

5d. PROJECT NUMBER

5e. TASK NUMBER

5f. WORK UNIT NUMBER

7. PERFORMING ORGANIZATION NAME(S) AND ADDRESS(ES)

Air Force Institute of Technology
Graduate School of Engineering and Management (AFIT/EN)
2950 Hobson Way
WPAFB OH 45433-7765

8. PERFORMING ORGANIZATION REPORT NUMBER

AFIT-ENY-DS-18-S-059

9. SPONSORING / MONITORING AGENCY NAME(S) AND ADDRESS(ES)

Intentionally Left Blank

10. SPONSOR/MONITOR'S ACRONYM(S)

11. SPONSOR/MONITOR'S REPORT NUMBER(S)

12. DISTRIBUTION / AVAILABILITY STATEMENT

DISTRIBUTION STATEMENT A:
APPROVED FOR PUBLIC RELEASE; DISTRIBUTION UNLIMITED.

13. SUPPLEMENTARY NOTES

14. ABSTRACT

The current resurgence of interest in hypersonic technologies has warranted an inquiry into the commonly employed thermochemical non-equilibrium models. Additionally, research has historically focused on forebody flow-fields, while studies of the complex wake structure have remained elusive. This dissertation aimed to address these two deficits. First, two three-temperature non-equilibrium models were developed, increasing the fidelity of hypersonic solutions above that of the legacy two-temperature model. The models were then investigated via zero-dimensional simulations, to detail the non-equilibrium processes, and ultimately implemented within a CFD architecture and validated against the RAM C-II flight test data. Second, a parametric study, characterizing the wake behind a generic slender cone configuration, was completed where the non-equilibrium processes were shown to extend a significant distance into the wake. The complex wake structure, coupled with the high-fidelity three-temperature model, has implications on radiative heating, communications blackout, and remote detection predictions.

15. SUBJECT TERMS

hypersonic, non-equilibrium, wake flows, computational fluid dynamics

16. SECURITY CLASSIFICATION OF:			17. LIMITATION OF ABSTRACT	18. NUMBER OF PAGES	19a. NAME OF RESPONSIBLE PERSON
a. REPORT	b. ABSTRACT	c. THIS PAGE			Dr. Robert Greendyke, AFIT/ENY
U	U	U	U	185	19b. TELEPHONE NUMBER *(include area code)* (937) 255-3069